

Doctoral Thesis Reviewed
by Ritsumeikan University

Study on Deformation Behavior of
Heterogeneous Structure Materials via Multi-Scale FEM Analysis

(マルチスケールFEM解析による
ヘテロ構造材料の変形挙動に関する研究)

March 2017

2017年03月

Doctoral Program in Advanced Mechanical
Engineering and Robotics
Graduate School of Science and Engineering
Ritsumeikan University

立命館大学大学院理工学研究科
機械システム専攻博士課程後期課程

YU Han

ユハン

Supervisor: Professor AMEYAMA Kei

研究指導教員：飴山 恵 教授

Abstract

Study on Deformation Behavior of Heterogeneous Structure Materials via Multi-Scale FEM Analysis

By

YU Han

Doctoral Program in Advanced Mechanical Engineering and Robotics

Graduate School of Science and Engineering

Ritsumeikan University

Academic Advisor: Prof. AMEYAMA Kei

Recently, a unique bi-modal micro-structure design, called “harmonic structure”, to achieve an improved set of strength and ductility which is consisted of coarse-grained (CG) areas (or “cores”) enclosed in a three-dimensional continuously connected network of ultra-fine grained (UFG) structure (or “shell”). The experimental results of an austenitic stainless steel SUS304L has been employed to compare with multi-scale finite element analysis (FEA) results. In this research, the harmonic structure result is compared with the same UFG volume fraction heterogeneous bi-model structure.

In this research, the multi-scale FEA has been raised to find the reason why the harmonic structure has strength and elongation, simultaneously. The finite element method (FEM) is a numerical technique for finding approximate solutions to boundary value problems for partial differential equations. FEM subdivides a large problem into smaller, simpler, parts, called finite elements. The simple equations which model these finite elements are then assembled into a larger system of equations as a large matrix that models the entire problem. However, the normal scale FEM can not meet the requirement of this research. Nowadays, micro-scale

mechanical analyses have been on an increasing trend in order to understand the behavior of modern materials with sophisticated micro-structures. The multi-scale FEA is applying the micro-scale model to describe the characteristics of macro-scale object. Periodic boundary condition is the bridge between the micro composition and the macro object. By using the micro structure model with periodic boundary condition, the stress and strain distribution of micro structure and the macro characteristic as stress-strain curve of object can be obtained. In this research, not only harmonic structure model and random structure model which have the experimental results but also inverse harmonic structure model and 3D fabric structure model have been raised to comparison.

Although there are some researches about periodic boundary condition for FEM, the discussions are almost focused on the mathematics. However, in order to build the program process successfully, there are some significant and error-prone points in the programming which are correct in mathematics. In this research, the specific thread to achieve the periodic boundary condition in ABAQUS has been discussed at great length. Moreover, a special shape called truncated octahedron (TO) has been applied as the basement shape in this research. In geometry, the TO is an Archimedean solid. TO has an especial characteristic as space-filling. For the harmonic structure, the cell-transitive bitruncated cubic honeycomb can also be seen as the Voronoi tessellation of the body-centered cubic lattice. The vertexes of the body-centered cubic lattice have been seen as CG region, while the remaining space has been treated as UFG region. By this way, arbitrary volume fraction of the UFG region can be achieved. Moreover, because of efficient space filling, this model can maintain almost the same thickness as the actual object throughout the shell. The TO can also be used for random structure, inverse harmonic structure model and 3D fabric structure model. In this research, the hexahedral mesh has been employed because of the computational efficiency and precision. However, the hexahedral mesh can not be briefly built automatically as the tetrahedral mesh. The meshing method has been discussed specifically in this research.

The FEA results show that there is still some stress and strain localization

happening in the general random bi-modal micro-structure, while the network structure of the harmonic structure materials avoids the stress and strain localization owing to the well-distributed deformation caused by network structure of UFG. From the comparison between harmonic structure and 3D fabric structure based on truncated octahedron, it demonstrates that not only the UFG network but also the uniform of the UFG network is a significant point for achieving the high mechanical capabilities of harmonic structure.

As a result, thanks to the uniform thickness connected UFG shell region, it can be obtained that harmonic structure design ensures the co-existence of high strength and high elongation in the material. The numerical simulation results indicate the consistency with the experimental results.

In this research, the effect of UFG volume fraction and CG/UFG material characteristics in harmonic and random structure material has also been discussed. It can be observed that while the UFG volume is near 50%, the harmonic structure shows obviously better performance than random structure. While the UFG volume is near the two terminal endpoints, harmonic structure still expresses well performance.

Application of deformation behavior of harmonic structure based on digital image correlation (DIC) has been raised to compare with results of multi-scale FEM in this research. It demonstrates that in DIC results, for harmonic structure, the relatively strain concentrations happened in the CG regions, while the UFG regions show lower strain, which keeps in agreement with multi-scale FEM results.

The possibility of harmonic structure multi-scale model with multi layer shell regions has been discussed in this thesis. By applying body fitted anisotropic layers in ICEM, FE model for harmonic structure with multi layer shell regions can be achieved. However, as the model is complicated itself, there are some errors happening in body fitted anisotropic layers creating process. We found there are some meshes disappeared in the GUI of ABAQUS. Owing to the complexity of the model, some meshes become minus volume meshes. After changing the direction of the meshes, the harmonic structure multi-scale model with multi layer shell regions can be obtained.

Thesis Contents

Chapter 1: Introduction	1
1.1 Background	1
1.2 Objective of dissertation	6
1.3 Outlet of dissertation	7
Chapter 2: Experimental procedure and FEM software introduction	16
2.1 Experimental procedure	16
2.1.1 Harmonic structure material fabrication	16
2.1.2 General random structure material fabrication	18
2.1.3 Kernel average misorientation results	20
2.1.4 Phase transition of harmonic structure material	22
2.2 FEM software introduction	23
2.2.1 ABAQUS CAE	23
2.2.2 Other software	25
Chapter 3: Modeling of harmonic structure	27
3.1 Periodic boundary condition	27
3.1.1 Periodic boundary condition in mathematics	27
3.1.2 Programming of periodic boundary condition for ABAQUS	30
3.2 Finite element model for harmonic structure	40
3.2.1 Geometry basement: truncated octahedron	40
3.2.2 Block dividing of harmonic structure model for meshing	42
3.3 Material characteristics of CG and UFG based on Hall-Petch rule	46

Chapter 4: Modeling of random structure and simulation results	
comparison with harmonic structure-----	52
4.1 Random structure's FEM model for comparative simulation-----	52
4.1.1 Block dividing of random structure model for meshing-----	52
4.1.2 Random materials setting-----	55
4.2 Simulation results comparison between harmonic structure and random structure-----	60
4.2.1 True stress-strain curves-----	60
4.2.2 Stress & strain contour distribution-----	61
4.2.3 Histograms of the stress and strain distribution frequency--	63
4.3 Conclusions-----	66
Chapter 5: Comparative simulations of 4 kinds 50% UFG volume fraction bi-modal heterogeneous models-----	71
5.1 4 kinds 50% UFG volume fraction models based on same geometry of truncated octahedron-----	71
5.2 Results-----	74
5.2.1 True stress-strain curves-----	74
5.2.2 Stress & strain contour distribution-----	75
5.2.3 Histogram for strain distribution frequency of 4 kinds models -----	81
5.3 Discussions-----	88
5.3.1 Irregular and non-uniform network structure happened in	

random structure-----	88
5.3.2 The perfect 3D fabric model based on geometry of cube---	91
5.4 Conclusions-----	93
Chapter 6: Effects of UFG volume fraction and CG/UFG material	
characteristics in harmonic structure material-----	96
6.1 Effect of shell volume fraction in harmonic structure material----	96
6.1.1 FEA models with 5 kinds of UFG volume fraction for	
harmonic structure and random structure-----	96
6.1.2 Stress and strain contour distribution-----	98
6.1.3 Histograms for strain distribution-----	100
6.2 Effect of CG/UFG material characteristics in harmonic structure	
material-----	103
6.2.1 FEA models with different CG/UFG material characteristics	
-----	103
6.2.2 Stress and strain distribution-----	105
6.2.3 Comparison of max stress/strain values of these bi-modal	
harmonic and random structures-----	107
6.3 Conclusions-----	109
Chapter 7: Application of deformation behavior of harmonic	
structure based on digital image correlation-----	111
7.1 Introduction of digital image correlation-----	111
7.2 Circumspect parts precautions for use of tensile test specimen	

photos for DIC-----	112
7.3 Programming for post treatment-----	117
7.4 Results-----	120
Chapter 8: The possibility of harmonic structure multi-scale model	
with multi layer shell region-----	128
8.1 The solid foundation of harmonic structure material with multi layer shell region-----	128
8.2 Body fitted anisotropic layers in ICEM-----	128
8.3 Dealing with the wrong sequence node serial number meshes--	132
8.4 Simulation results-----	135
8.5 Conclusions-----	136
Acknowledgement-----	138

Chapter 1: Introduction

1.1 Background

In the pursuit of developing tougher structural metallic materials, the general trend has been to focus on grain refinement, especially, the creation of homogeneous ultrafine-grained (UFG) micro-structures [1-7]. However, it is extremely difficult to simultaneously achieve high strength and high ductility, which are conflicting but desirable properties, in materials with homogeneous and UFG structures. However, the high strength homogeneous UFG materials always show the shortcoming of poor ductility due to plastic instability at the early stage of deformation, which becomes a regrettable barrier to the wider spread commercial applications [8-10]. In order to deal with the antinomy characteristic of the strength and ductility, researches for enhancing the ductility of high-strength UFG materials have been raised. An effectual micro-structural possibility solving this problem is to develop a bi-modal grain-size distribution, in which the fine grains support strength, while the coarser grains enable strain hardening [11-32]. However, in most researches above, there is little attention focused on the arrangement of the bi-modal micro-structures, where mere random bi-modal micro-structures were applied in. While in some researches, regular arrangement bi-modal micro-structure designs have been applied [23,29,30,32-38]. Multilayer structure is a widely used design. Daly et al. (2015) raised a distinct multilayer NiCo with a modulated grain size distribution [23]. Beyerlein and Mayeur (2015) employed a two-phase multilayer Cu-Nb by accumulative roll bonding (ARB) [34]. Benafan et al. (2015) brought up a research of thermomechanical behavior and micro-structural evolution for a multilayer high temperature shape memory alloy [37]. Other multilayer bi-modal micro-structures have been obtained through hot extrusion [29,30] and pulsed electrodeposition [32]. To study the assistance of growth twin in nano-layered polycrystalline metallic multilayers to their strength, Zhu et al. (2015) raised a series of uniaxial tensile modeling of nano-twinned Cu/Ag and Cu/Ni multilayers by molecular dynamics method [35]. Whereas the multilayer structure

shows directivity, which will bring the limitation of force direction. Non-directional design should be developed. Kumar et al. (2015) raised a research of strength and ductility optimization of Mg–Y–Nd–Zr alloy by micro-structural design, while an obvious partial honeycomb network arrangement was found in high angle annular dark field scanning transmission electron microscopy (HAADF-STEM) mode [36]. Zhu and Lu (2012) developed a plastic deformation model research for nano-structured metals in which coarse grains are embedded in a ultrafine grains matrix as a network structure [33]. Chen et al. (2016) applied a fastened dumbbell-shaped cross metallic thin-walled round tubes to make a novel self-locked energy absorbing system, which showed the benefit of network structure under impact loadings [38]. While the network structure exhibits more and more advantage, recently, a unique regular arrangement bi-modal micro-structure design—called a harmonic structure—has been proposed to successfully improve the relationship between strength and ductility [39-40]. The harmonic structure is a unique heterogeneous bi-modal structure consisting of coarse-grained (CG) areas (cores) enclosed in a three-dimensional continuously connected network of UFG structures (shell). The concept of harmonic-structure design has been successfully applied to a variety of pure metals and metallic alloys (e.g., Ti, Al, Ni, SUS304L, CCM) [39-54]. Ameyama et al. (2009); Fujiwara et al. (2009); Sekiguchi et al. (2010); Ota et al. (2015) raised pure Ti harmonic structure [40,43,47]; Ameyama et al. (2009); Fujiwara et al. (2009) applied SUS316L stainless steel to produce harmonic structure [40,42]; Fujiwara et al. (2009); Vajpai et al. (2015) developed Ti-Al-4V alloy harmonic structure [42,52]; Sawangrat et al. (2014); Vajpai et al. (2016) employed Co-Cr-Mo alloy to manufacture harmonic structure [48,53]; Ota et al. (2014) investigated the mechanical properties of pure Ni harmonic structure [45]; Orlov et al. (2013) raised pure Cu harmonic structure [44]; Zhang et al. (2014, 2015) made a research of SUS304L stainless steel harmonic structure [49,50]. Mechanically milled (MM) is used in most of researches above, while a highly active milling process called jet milling process is applied in pure Ti and Ti-Al-4V alloy harmonic structure research [47]. Compared to traditional MM process, jet milling use highly compressed air or

gases to facilitate the collision of fine particles against each other at a very high velocity [54]. All these harmonic structure materials demonstrate a desirable combination of improved strength and ductility compared to their CG as well as UFG counterparts. Dirras et al. (2015) carried out a research about micro-structure evolution during direct impact loading of commercial harmonic structure purity α -titanium. In the research, tortuous localization bands 25 - 30 μm wide were observed whose micro-structural characteristics suggest dynamic recrystallization as a consequence of adiabatic heating [55]. Kikuchi et al. (2015) raised an evaluation of near-threshold fatigue crack propagation in Ti-6Al-4V Alloy with harmonic structure [56]. It showed that the harmonic structure also demonstrated better mechanical behavior than the compact prepared from as-received powder in fatigue experiment.

Table 1.1 demonstrates harmonic-structure materials mechanical capabilities. The numerical values represent the comparison of divers metals and alloys with harmonic structure and their coarse-grained counterparts prepared from initial powders. From Table 1.1, it can be indicated that with the harmonic structure, materials capabilities of normalized yield strength and ultimate tensile strength increase compared to original coarse-grained materials significantly. From the data of total elongation, it can also be shown that many metals and alloys demonstrate improved ductility as compared to original coarse-grained materials. A few materials show lower elongation than original materials, but harmonic-structure values are very close to values of the original materials. Nevertheless, since the area under the stress-strain curve is considered as a representation of the toughness of materials, the harmonic-structure materials also demonstrate enhanced toughness relative to their coarse-grained counterparts. Hence, in consideration of the distinguished strength improvement, the harmonic-structure mechanical capabilities developed relative to original coarse-grained materials overall.

Therefore, these results clearly exhibit that the harmonic-structure design leads to enhanced mechanical properties in most of the metals and alloys which indicate that the harmonic-structure metallic material would also result in improved performance in service.

Table 1.1: Harmonic-structure mechanical capabilities relative to original materials.

Harmonic-Structure material	yield stress	ultimate tensile strength	total elongation	toughness
pure Ti (Fujiwara et al. (2009))	× 1.47	× 1.26	× 0.97	× 1.27
pure Ti (JM) (Ota et al. (2015))	× 1.64	× 1.52	× 1.10	× 2.19
pure Al	× 1.22	× 1.25	× 0.81	× 1.45
pure Cu (Orlov et al. (2013))	× 1.14	× 1.19	× 1.31	× 1.57
pure Ni (Ota et al. (2014))	× 1.21	× 1.20	× 1.05	× 1.25
pure Fe	× 2.00	× 1.31	× 0.83	× 1.17
Co-Cr-Mo alloy (Vajpai et al. (2016))	× 1.01	× 1.17	× 1.48	× 1.87
Ti-6Al-4V alloy (Vajpai et al. (2015))	× 1.14	× 1.12	× 1.21	× 1.33
Ti-6Al-4V alloy (JM) (Ota et al. (2015))	× 1.28	× 1.27	× 0.87	× 1.22
SUS316L stainless steel (Fujiwara et al. (2008))	× 2.00	× 1.51	× 1.05	× 1.50
SUS304L stainless steel	× 1.71	× 1.30	× 0.85	× 1.19
SUS329J1 stainless steel (Ota et al. (2014))	× 1.35	× 1.20	× 0.97	× 1.25
SUS430 stainless steel	× 1.00	× 1.20	× 0.98	× 1.40
average	× 1.40	× 1.27	× 1.04	× 1.43

Figure 1.1 shows the example of effect of milling time on the mechanical properties of harmonic Titanium by representative engineering stress-strain curves. From the results of the engineering stress-strain curves, it can be revealed that the harmonic structure pure Ti has both higher strength and elongation than initial powder [57].

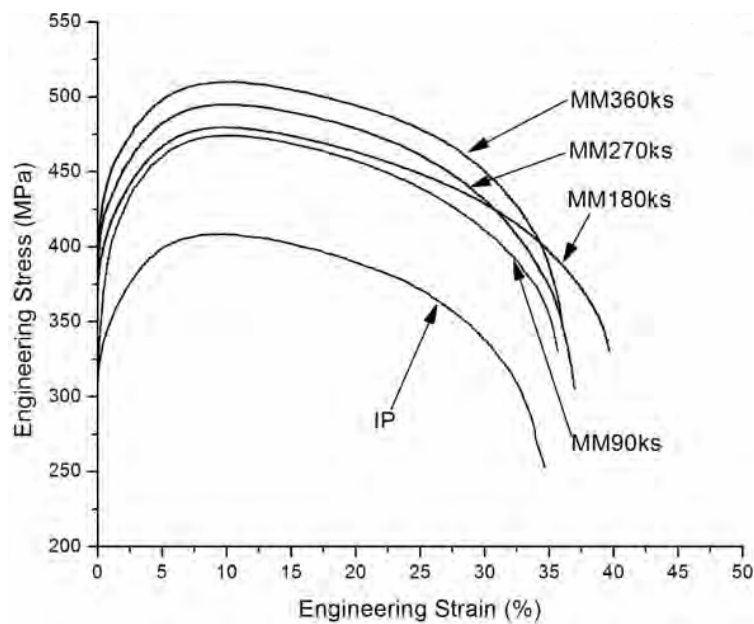


Figure 1.1: Effect of milling time on the mechanical properties of harmonic Titanium: Representative Engineering Stress-Strain Curves [57].
Copyright © 2016 The Japan Institute of Metals and Materials.

To understand the underlying mechanism behind the response of harmonic-structure materials, numerical simulation has been performed based on the finite element (FE) analysis of periodic micro-structures.

The finite element method (FEM) is a numerical technique for finding approximate solutions to boundary value problems for partial differential equations. It is also referred to as FE analysis. FEM subdivides a large problem into smaller, simpler, parts, called finite elements. The simple equations that model these finite elements are then assembled into a larger system of equations that models the entire problem. FEM then uses variational methods from the calculus of variations to approximate a solution by minimizing an associated error function [58].

By employing the FE analysis of a periodic micro-structure, the deformation of the micro-structure and the corresponding macroscopic material response can be characterized, which is a viable method to investigate the relationship between the deformation mechanism and macroscopic material properties [59-62].

Recently, FE analysis has been applied to analyze the mechanical mechanism of heterogeneous micro-structures. FE analyses have been applied to composites

containing soft-phase particles distributed in a hard-phase matrix [62-67]. Wang et al. (2011) carried out the FE analyses of tensile deformation and fracture analysis for CuW alloys at the mesoscopic level and found that the hard phase of W showed high stress distribution in the tensile test simulation [64]. Yu et al. (2008) investigated the thermal properties of the Al/SiC_p matrix composite based on FE analysis and found that the hard phase still showed high stress distribution in the thermal expansion [63]. Some studies have been conducted on complex substances containing hard material particles distributed in a soft material network [63,68-70], whereas other studies have investigated hard-phase material fibers arrayed in a soft-phase material [59,71-74]. In studies that considered stress distribution [63,66,68,69,71-75], the hard phase always showed high stress whereas the soft phase showed low stress. While in some researches, FE analysis has also been developed to investigate the random bi-modal structure [76] and multilayer structure [77,78].

1.2 Objective of dissertation

In this study, the FE analysis of a periodic micro-structure is carried out to demonstrate the multi-scale deformation behavior of harmonic-structure materials. The study presents multi-scale comparative structural analyses of two types of heterogeneous structural materials: a harmonic-structure material with a network structure, and a random-structure material without a network structure. Microscopic models of the harmonic- and random-structure materials have been developed in this research. Both these models are based on the shape of a truncated octahedron and have the same material characteristics as those of CG and UFG structures. The two models differ in terms of whether they contain a network structure. The tensile test simulation of these two structural models has been performed by applying a periodic boundary condition. The mechanical effect of the network structure has also been investigated by discussing and comparing the stress and strain distribution results obtained using these two models.

1.3 Outlet of dissertation

The present dissertation consists of seven chapters as follows:

Chapter 2 presents the experimental procedure and software introduction. The fabrication of harmonic-structured SUS304L steels by mechanical milling and consolidating process.

Chapter 3 presents the processing of multi-scale finite element model for harmonic structure. In order to describe the repeated units, the period boundary condition has been used in this research. The achievement of period boundary condition in ABAQUS is described in this chapter.

Chapter 4 presents the processing of multi-scale finite element model for random structure and simulation results comparison between Harmonic Structure and Random Structure. In this chapter, the importance of network structure of harmonic structure can be observed.

Chapter 5 demonstrates the Comparative simulations of 4 kinds 50% UFG volume fraction bi-model heterogeneous models based on same geometry of truncated octahedron. In this chapter, we knew that not only network structure, but also the uniform thickness of the network is a significant function to decide the coexistence of strength and elongation of harmonic structure.

Chapter 6 presents the effects of UFG volume fraction and CG/UFG material characteristics in harmonic structure material.

Chapter 7 demonstrates the application of deformation behavior of harmonic structure based on Digital Image Correlation. In this chapter, the measuring result of DIC for the strain distribution of harmonic structure has been observed and compared to the calculated result of FEM.

Chapter 8 investigates the possibility of harmonic structure multi-scale model with multi layer shell region.

References

- [1] Gleiter, H., 2000. Nanostructured materials: basic concepts and microstructure. *Acta Mater.* 48 (1), 1 - 29.
- [2] Hansen, N., 2004. Hall-petch relation and boundary strengthening. *Scr. Mater.* 51 (8), 801 - 806.
- [3] Meyers, M. A., Mishra, A., Benson, D. J., 2006. Mechanical properties of nanocrystalline materials. *Prog. Mater. Sci.* 51 (4), 427 - 556.
- [4] Sauvage, X., Wilde, G., Divinski, S., Horita, Z., Valiev, R., 2012. Grain boundaries in ultrafine grained materials processed by severe plastic deformation and related phenomena. *Mater. Sci. Eng.: A* 540, 1 - 12.
- [5] Estrin, Y., Vinogradov, A., 2013. Extreme grain refinement by severe plastic deformation: a wealth of challenging science. *Acta Mater.* 61 (3), 782 - 817.
- [6] Liu, L. H., Yang, C., Wang, F., Qu, S. G., Li, X. Q., Zhang, W. W., Li, Y. Y., Zhang, L. C., 2015. Ultrafine grained Ti-based composites with ultrahigh strength and ductility achieved by equiaxed microstructure. *Mater. Design.* 79 (15), 1 - 5.
- [7] Zhang, Z. J., Pang, J. C., Zhang, Z. F., 2016. Optimizing the fatigue strength of ultrafine-grained Cu-Zn alloys. *Materials Sci. Eng.: A* 666, 305 - 313.
- [8] Huang, X. X., Hansen, N., Tsuji, N., 2006. Hardening by annealing and softening by deformation in nanostructured metals. *Science* 312 (5771), 249 - 251.
- [9] Zhao, Y. H., Liao, X. Z., Cheng, S., Ma, E., Zhu, Y. T., 2006. Simultaneously increasing the ductility and strength of nanostructured alloys. *Adv. Mater.* 18 (17), 2280 - 2283.
- [10] Wu, X. L., Jiang, P., Chen, L., Yuan, F. P., Zhu, Y. T., 2014. Extraordinary strain hardening by gradient structure. *Proc. Natl. Acad. Sci.* 111(20), 7197 - 7201.
- [11] Zhao, M. C., Yin, F. X., Hanamura, T., Nagai, K., Atrens, A., 2007. Relationship between yield strength and grain size for a bimodal structural ultrafine-grained ferrite/cementite steel. *Scripta Mater.* 57 (9), 857 - 860.
- [12] Sano, T., Rohrer, G. S., 2007. Experimental evidence for the development of bimodal grain size distributions by the nucleation-limited coarsening mechanism.

- J. Am. Cera. Soc. 90 (1), 211 - 216.
- [13] Chakrabarti, D., Davis, C., Strangwood, M., 2007. Characterisation of bimodal grain structures in HSLA steels. *Mater. Charact.* 58(5), 423 - 438.
- [14] Tejedor, R., Rodriguez-Baracaldo, R., Benito, J., Cabrera, J., Prado, J., 2008. Plastic deformation of a nanostructured and ultrafine grained Fe-1%Cr with a bimodal grain size distribution. *Int. J. Mater. Forming* 1 (1), 487 - 490.
- [15] Wang, T. S., Zhang, F. C., Zhang, M., Lv, B., 2008. A novel process to obtain ultrafine-grained low carbon steel with bimodal grain size distribution for potentially improving ductility. *Mater. Sci. Eng.: A* 485 (1), 456 - 460.
- [16] Afshar, A., Simchi, A., 2009. Flow stress dependence on the grain size in alumina dispersion-strengthened copper with a bimodal grain size distribution. *Mater. Sci. Eng.: A* 518 (1), 41 - 46.
- [17] Prasad, M., Suwas, S., Chokshi, A., 2009. Microstructural evolution and mechanical characteristics in nanocrystalline nickel with a bimodal grain-size distribution. *Mater. Sci. Eng.: A* 503 (1), 86 - 91.
- [18] Zhao, D. P., Liu, Y., Liu, F., Wen, Y. R., Zhang, L. J., Dou, Y. H., 2011. ODS ferritic steel engineered with bimodal grain size for high strength and ductility. *Mater. Lett.* 65(11), 1672 - 1674.
- [19] Gollapudi, S., 2012. Grain size distribution effects on the corrosion behavior of materials. *Corros. Sci.* 62, 90 - 94.
- [20] Patra, S., Hasan, S. M., Narasaiah, N., Chakrabarti, D., 2012. Effect of bimodal distribution in ferrite grain sizes on the tensile properties of low-carbon steels. *Mater. Sci. Eng.: A* 538, 145 - 155.
- [21] Raju, K. S., Sarma, V. S., Kauffmann, A., Hegedus, Z., Gubicza, J., Peter-lechner, M., Freudenberger, J., Wilde, G., 2013. High strength and ductile ultrafine-grained Cu-Ag alloy through bimodal grain size, dislocation density and solute distribution. *Acta Mater.* 61 (1), 228 - 238.
- [22] Casas, C., Tejedor, R., Rodriguez-Baracaldo, R., Benito, J., Cabrera, J., 2015. The effect of oxide particles on the strength and ductility of bulk iron with a bimodal grain size distribution. *Mater. Sci. Eng.: A* 627, 205 - 216.

- [23] Daly, M., McCrea, J. L., Bouwhuis, B. A., Singh, C. V., Hibbard, G. D., 2015. Deformation behavior of a NiCo multilayer with a modulated grain size distribution. *Mater. Sci. Eng.: A* 641, 305 - 314.
- [24] Hilger, I., Bergner, F., Weißgarber, T., 2015. Bimodal grain size distribution of nanostructured ferritic ODS Fe - Cr alloys. *J. Am. Ceram. Soc.* 98 (11), 3576 - 3581.
- [25] Kidder, S., Hirth, G., Avouac, J.-P., Behr, W., 2015. The influence of stress history on the grain size and microstructure of experimentally deformed quartzite. *J. Struc. Geo.* 83, 194 - 206.
- [26] Oskooie, M. S., Asgharzadeh, H., Kim, H., 2015. Microstructure, plastic deformation and strengthening mechanisms of an Al-Mg-Si alloy with a bimodal grain structure. *J. Alloy. Compd.* 632, 540 - 548.
- [27] Szabó, P. J., Field, D. P., Jóni, B., Horoky, J., Ungár, T., 2015. Bimodal Grain Size Distribution Enhances Strength and Ductility Simultaneously in a Low-Carbon Low-Alloy Steel. *Metall. Mater. Trans. A* 46 (5), 1948 - 1957.
- [28] Sabooni, S., Karimzadeh, F., Enayati, M. H., Ngan, A. H. W., 2015. The role of martensitic transformation on bimodal grain structure in ultrafine grained AISI 304L stainless steel. *Mater. Sci. Eng.: A* 636, 221 - 230.
- [29] Shan, Y., Xu, J., Wang, G., Sun, X., Liu, G., Xu, J., & Li, J. 2015. A fast pressureless sintering method for transparent ALON ceramics by using a bimodal particle size distribution powder. *Ceram. Int.* 41 (3), 3992 - 3998.
- [30] Shen, M. J., Wang, X. J., Zhang, M. F., Zheng, M. Y., Wu, K., 2015. Significantly improved strength and ductility in bimodal-size grained microstructural magnesium matrix composites reinforced by bimodal sized SiC_p over traditional magnesium matrix composites. *Compos. Sci. Tech.* 118, 85 - 93.
- [31] Shen, M. J., Zhang, M. F., Ying, W. F., 2015. Processing, microstructure and mechanical properties of bimodal size SiC_p reinforced AZ31B magnesium matrix composites. *J. Magn. Alloy.* 3 (2), 162 - 167.
- [32] Fiebig, J., Jian, J., Kurmanaeva, L., McCrea, J., Wang, H., Lavernia, E., Mukherjee, A., 2016. Deformation behavior of multilayered NiFe with bimodal

- grain size distribution at room and elevated temperature. *Mater. Sci. Eng.:A* 656, 174 - 183.
- [33] Zhu, L. L., Lu, J., 2012. Modelling the plastic deformation of nanostructured metals with bimodal grain size distribution. *Int. J. Plasticity* 30, 166 - 184.
- [34] Beyerlein, I. J., Mayeur, J. R., 2015. Mesoscale investigations for the evolution of interfaces in plasticity. *Curr. Opin. Solid St. Mater. Sci.* 19 (4), 203 - 211.
- [35] Zhu, Y. X., Li, Z. H., Huang, M. S., Liu, Y., 2015. Strengthening mechanisms of the nanolayered polycrystalline metallic multilayers assisted by twins. *Int. J. Plasticity* 72, 168 - 184.
- [36] Kumar, N., Choudhuri, D., Banerjee, R., Mishra, R., 2015. Strength and ductility optimization of Mg-Y-Nd-Zr alloy by microstructural design. *Int. J. Plasticity* 68, 77 - 97.
- [37] Benafan, O., Garg, A., Noebe, R., Bigelow, G., Padula, S., Gaydos, D., Vaidyanathan, R., Clausen, B., Vogel, S., 2015. Thermomechanical behavior and microstructural evolution of a Ni(Pd)-rich $\text{Ni}_{24.3}\text{Ti}_{49.7}\text{Pd}_{26}$ high temperature shape memory alloy. *J. Alloy. Compd.* 643, 275 - 289.
- [38] Chen, Y. L., Qiao, C., Qiu, X. M., Zhao, S. G., Zhen, C. R., Liu, B., 2016. A novel self - locked energy absorbing system. *J. Mech. Phys. Solid.* 87, 130 - 149.
- [39] Fujiwara, H., Akada, R., Noro, A., Yoshita, Y., Ameyama, K., 2008. Enhanced mechanical properties of nano/meso hybrid structure materials produced by hot roll sintering process. *Mater. Trans.* 49 (1), 90 - 96.
- [40] Ameyama, K., Fujiwara, H., Zoz, H., 2009. A new tailored nano-scaled network-structure for metals at outstanding mechanical properties by severe plastic deformation pm process. *Trans. PMAI* 34, 1 - 4.
- [41] Fujiwara, H., Nakatani, M., Yoshida, T., Zhang, Z., Ameyama, K., 2008. Outstanding mechanical properties in the materials with a nano/meso hybrid microstructure. In: *Materials Science Forum*. Vol. 584. *Trans. Tech. Publ.* 55 - 60.
- [42] Fujiwara, H., Sekiguchi, T., Ameyama, K., 2009. Mechanical properties of pure titanium and Ti-6Al-4V alloys with a new tailored nano/meso hybrid microstructure. *Int. J. Mater. Res.* 100 (6), 796 - 799.

- [43] Sekiguchi, T., Ono, K., Fujiwara, H., Ameyama, K., 2010. New microstructure design for commercially pure titanium with outstanding mechanical properties by mechanical milling and hot roll sintering. *Mater. Trans.* 51 (1), 39 - 45.
- [44] Orlov, D., Fujiwara, H., Ameyama, K., 2013. Obtaining copper with harmonic structure for the optimal balance of structure-performance relationship. *Mater. Trans.* 54 (9), 1549 - 1553.
- [45] Ota, M., Sawai, K., Kawakubo, M., Vajpai, S. K., Ameyama, K., 2014. Harmonic structure formation and deformation behavior in a ($\alpha + \gamma$) two phase stainless steel. *Mater. Sci. Eng.* 63, 012027.
- [46] Ota, M., Shimojo, K., Okada, S., Vajpai, S., Ameyama, K., 2014. Harmonic structure design and mechanical properties of pure Ni compact. *J. Powder. Metall. Min* 3, 1000122.
- [47] Ota, M., Vajpai, S. K., Imao, R., Kurokawa, K., Ameyama, K., 2015. Application of high pressure gas jet mill process to fabricate high performance harmonic structure designed pure titanium. *Mater. Trans.* 56 (1), 154 - 159.
- [48] Sawangrat, C., Yamaguchi, O., Vajpai, S. K., Ameyama, K., 2014. Harmonic structure design of Co-Cr-Mo alloy with outstanding mechanical properties. In: *Advanced Materials Research*. Vol. 939. Trans Tech Publ, pp. 60 - 67.
- [49] Zhang, Z., Vajpai, S. K., Orlov, D., Ameyama, K., 2014. Improvement of mechanical properties in SUS304L steel through the control of bimodal microstructure characteristics. *Mater. Sci. Eng. A* 598, 106 - 113.
- [50] Zhang, Z., Orlov, D., Vajpai, S. K., Tong, B., Ameyama, K., 2015. Importance of Bimodal Structure Topology in the Control of Mechanical Properties of a Stainless Steel. *Adv. Eng. Mater.* 17(6), 791-795.
- [51] Vajpai, S. K., Ameyama, K., Ota, M., Watanabe, T., Maeda, R., Sekiguchi, T., Dirras, G., Tingaud, D., 2014. High performance Ti-6Al-4V alloy by creation of harmonic structure design. In: *IOP Conference Series: Materials Science and Engineering*. Vol. 63. IOP Publishing, p. 012030.
- [52] Vajpai, S. K., Ota, M., Watanabe, T., Maeda, R., Sekiguchi, T., Kusaka, T., Ameyama, K., 2015. The development of high performance Ti-6Al-4V alloy via a

- unique microstructural design with bimodal grain size distribution. *Metall. Mater. Trans. A* 46 (2), 903 - 914.
- [53] Vajpai, S. K., Sawangrat, C., Yamaguchi, O., Ciuca, O. P., Ameyama, K., 2016. Effect of bimodal harmonic structure design on the deformation behaviour and mechanical properties of Co-Cr-Mo alloy. *Mater. Sci. Eng.: C* 58, 1008 - 1015.
- [54] Midoux, N., Hořšek, P., Pailleres, L., Authelin, J., 1999. Micronization of pharmaceutical substances in a spiral jet mill. *Powder Technology* 104 (2), 113 - 120.
- [55] Dirras, G., Ota, M., Tingaud, D., Ameyama, K., Sekiguchi, T., 2015. Microstructure evolution during direct impact loading of commercial purity -titanium with harmonic structure design-direct impact loading of pure harmonic -Ti. *Materiaux Tech.* 103 (3), No.311, 1 - 9.
- [56] Kikuchi, S., Imai, T., Kubozono, H., Nakai, Y., Ueno, A., Ameyama, K., 2015. Evaluation of near-threshold fatigue crack propagation in Ti-6Al-4V alloy with harmonic structure created by mechanical milling and spark plasma sintering. *Fract. Struct. Integ.* 34, 261 - 270.
- [57] Vajpai, S. K., Yu, H., Ota, M., Watanabe, I., Dirras, G., & Ameyama, K. 2016. Three-Dimensionally Gradient and Periodic Harmonic Structure for High Performance Advanced Structural Materials. *Mater. Trans.* 57, 1424 - 1432.
- [58] Finite element method, Wikipedia,
https://en.wikipedia.org/wiki/Finite_element_method.
- [59] Chen, Y. L., Ghosh, S., 2012. Micromechanical analysis of strain rate-dependent deformation and failure in composite microstructures under dynamic loading conditions. *Int. J. Plast.* 32, 218 - 247.
- [60] Watanabe, I., Terada, K., Akiyama, M., 2005. Two-scale analysis for deformation-induced anisotropy of polycrystalline metals. *Comput. Mater. Sci.* 32 (2), 240 - 250.
- [61] Watanabe, I., Terada, K., de Souza Neto, E. A., Peric, D., 2008. Characterization of macroscopic tensile strength of polycrystalline metals with two-scale finite element analysis. *J. Mech. Phys. Solids* 56 (3), 1105 - 1125.
- [62] Watanabe, I., Nakamura, G., Yuge, K., Setoyama, D., Iwata, N., 2015.

- Maximization of strengthening effect of microscopic morphology in duplex steels. In: *From Creep Damage Mechanics to Homogenization Methods*. Vol. 64. Springer, pp. 541 - 555.
- [63] Yu, E., Sun, J. Y., Chung, H. S., Oh, K. H., 2008. Investigation on thermal properties of Al/SiC_p metal matrix composite based on FEM analysis. *Int. J. Mod. Phys. B* 22 (31n32), 6167 - 6172.
- [64] Wang, Y. L., Liang, S. H., Xiao, P., Zou, J. T., 2011. FEM simulations of tensile deformation and fracture analysis for CuW alloys at mesoscopic level. *Comput. Mater. Sci.* 50 (12), 3450 - 3454.
- [65] Jeon, C., Kim, C., Joo, S.-H., Kim, H., Lee, S., 2013. High tensile ductility of Ti-based amorphous matrix composites modified from conventional Ti - 6Al - 4V titanium alloy. *Acta. Mater.* 61 (8), 3012 - 3026.
- [66] Cao, C. Y., Qin, Q. H., Yu, A. B., 2013. Micromechanical analysis of heterogeneous composites using hybrid trefftz FEM and hybrid fundamental solution based FEM. *J. Mech.* 29 (04), 661 - 674.
- [67] Debski, H., Sadowski, T., 2014. Modelling of microcracks initiation and evolution along interfaces of the WC/Co composite by the finite element method. *Comput. Mater. Sci.* 83, 403 - 411.
- [68] Wang, Z. Q., Liu, F., Liang, W. Y., Zhou, L. M., 2013. Study on tensile properties of nanoreinforced epoxy polymer: Macroscopic experiments and nanoscale FEM simulation prediction. *Adv. Mater. Sci. Eng.* 2013, 8 pages.
- [69] Kim, Y. R., Souza, F., Teixeira, J., 2013. A two-way coupled multiscale model for predicting damage-associated performance of asphaltic roadways. *Comput. Mech.* 51 (2), 187 - 201.
- [70] Yang, W. L., Peng, K., Zhou, L. P., Zhu, J. J., Li, D. Y., 2014. Finite element simulation and experimental investigation on thermal conductivity of diamond/aluminium composites with imperfect interface. *Comput. Mater. Sci.* 83, 375 - 380.
- [71] Jia, X. W., Xia, Z. H., Gu, B. H., 2013. Numerical analyses of 3D orthogonal woven composite under three-point bending from multi-scale microstructure

- approach. *Comput. Mater. Sci.* 79, 468 - 477.
- [72] Bouhala, L., Makradi, A., Belouettar, S., Kamal, H. K., Freres, P., 2013. Modelling of failure in long fibres reinforced composites by X-FEM and cohesive zone model. *Compos. Part. B-eng.* 55, 352 - 361.
- [73] Wu, L. W., Zhang, F., Sun, B. Z., Gu, B. H., 2014. Finite element analyses on three-point low-cyclic bending fatigue of 3-D braided composite materials at microstructure level. *Int. J. Mech. Sci.* 84, 41 - 53.
- [74] Joshi, P., Upadhyay, S., 2014. Evaluation of elastic properties of multi walled carbon nanotube reinforced composite. *Comput. Mater. Sci.* 81, 332 - 338.
- [75] Wang, Y. L., Liang, S. H., Xiao, P., Zou, J. T., 2011. FEM simulations of tensile deformation and fracture analysis for CuW alloys at mesoscopic level. *Comput. Mater. Sci.* 50 (12), 3450 - 3454.
- [76] Hachemi, A., Chen, M., Chen, G., Weichert, D., 2014. Limit state of structures made of heterogeneous materials. *Int. J. Plasticity* 63, 124 - 137.
- [77] Hansen, B., Carpenter, J., Sintay, S., Bronkhorst, C., McCabe, R., Mayeur, J., Mourad, H., Beyerlein, I., Mara, N., Chen, S., et al., 2013. Modeling the texture evolution of Cu/Nb layered composites during rolling. *Int. J. Plasticity* 49, 71 - 84.
- [78] Huang, M. S., Li, Z. H., 2015. Coupled DDD-FEM modeling on the mechanical behavior of microlayered metallic multilayer film at elevated temperature. *J. Mech. Phys. Solid.* 85, 74 - 97.

Chapter 2: Experimental procedure and FEM software introduction

2.1 Experimental procedure

2.1.1 Harmonic structure material fabrication

In this research, the characteristics of harmonic structure SUS304L grade stainless steel have been discussed. SUS304L grade stainless steel powder was used for the fabrication. Stainless steels are an important group of alloys which are widely used in many fields, from low-end applications, like cooking utensils and furniture. To very sophisticated ones, such as astronautics vehicles, the employment of stainless steels is imperative. Figure 2.1 shows the schematic of the fabrication process of harmonic-structured materials, while Table 2.1 reveals the mechanical milling and SPS conditions for Harmonic Structure SUS304L. After mechanically milled (MM), the ultra-fine grains will be achieved in initial coarse grain powders' boundary. The SUS304L powder was MM for 180 ks. Mechanical milling was carried out in a planetary ball mill (P-5, Fritsch [1]) manufactured by Fritsch GmbH in Germany using SUS304L steel vial and balls (diameter: 10 mm). The milling was carried out under argon gas atmosphere at room temperature, and the ball-to-powder weight ratio was maintained at 2:1. The rotation speed is 200 rpm. The mechanically milled powder was sintered by the spark plasma sintering (SPS) process at 1123 K for 3.6 ks in vacuum under an applied pressure of 50 MPa. Spark plasma sintering (SPS) is a newly developed sintering process that combines the use of mechanical pressure and microscopic electric discharge between the particles. The enhance densification in this process has been attributed to localized self-heat generation by the discharge, activation of the particle surfaces, and the high speed of mass and heat transfer during the sintering process. As a result, samples can rapidly reach full density at relatively low temperature [2].

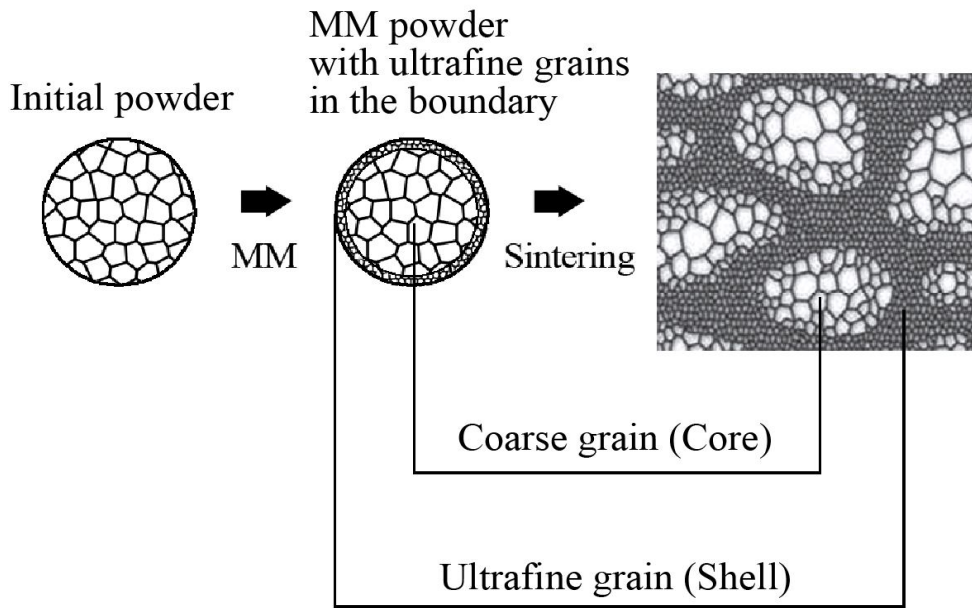


Figure 2.1: Schematic of harmonic-structured materials fabrication process.

Table 2.1: Mechanical milling and SPS conditions for harmonic structure SUS304L.

Mechanical Milling conditions		SPS conditions	
Temperature	Room Temperature	Temperature	1173K
Time	180ks, 360ks	Hold time	60min
Ball : Powder	2 : 1	Pressure	50MPa
Rotation speed	200rpm	Atmosphere	Vacuum<0.1MPa
Atmosphere	Ar		

The microstructure of the SUS304L harmonic-structure material (Figure 2.2(b)) was analyzed by electron backscatter diffraction (EBSD) [4,5]. Electron backscatter diffraction (EBSD) based on scanning electron microscopy (SEM) is a powerful technique to automatically and quantitatively measure the grain/subgrain size, local texture, point-to-point orientations, strain and phase identification. It has been established that EBSD has a lot of advantages over transmission electron microscopy (TEM), such as simple sample preparation, automatic scanning and indexing, ultra-fast speed, large area investigation and a lot of post-processing results derived from one EBSD scan [3]. The analysis results showed that the average grain sizes of

the coarse and ultrafine grains were 16.9 and 2.0 μm , respectively. The area fraction of the ultrafine grain was found to be approximately 20.7%.

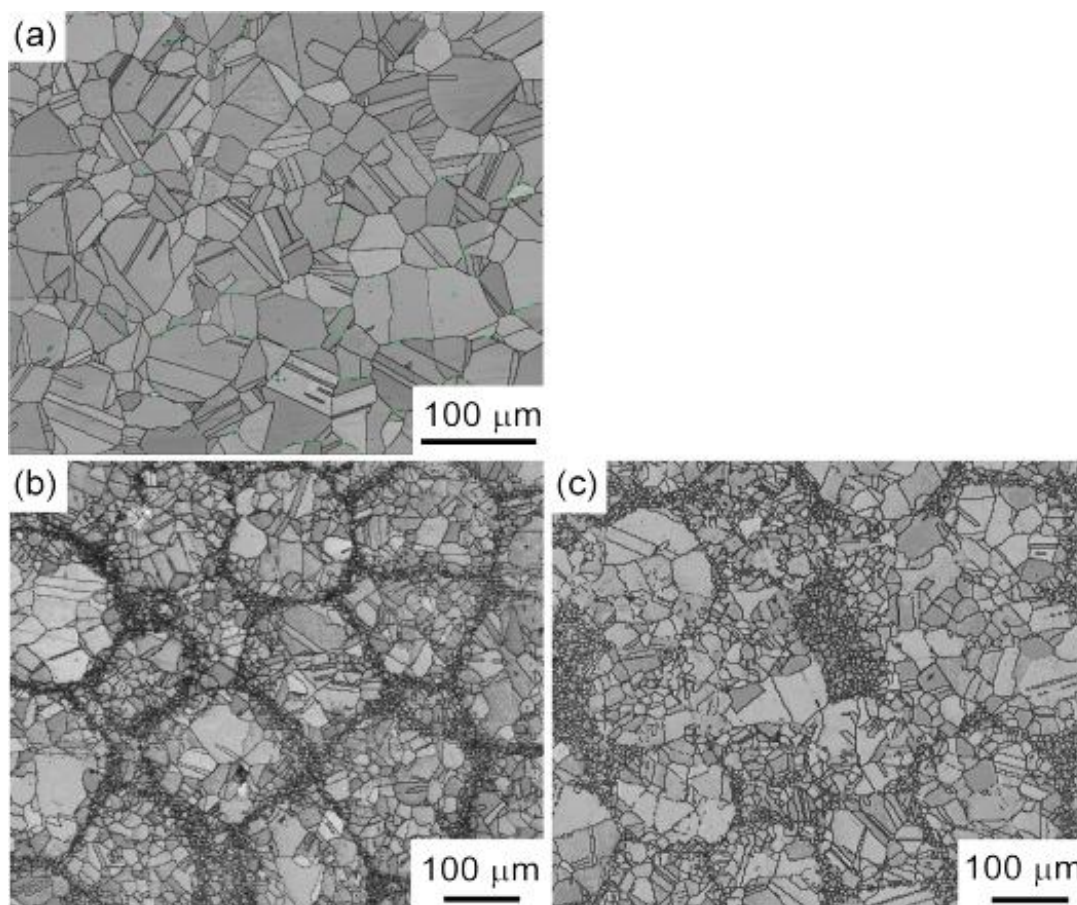


Figure 2.2: The microstructure of (a) SUS304L Initial Powder (IP); (b) harmonic structure SUS304L material, MM 180ks Compact; (c) random structure material, IP+MM360ks (weight ration=1:1) Compact by EBSD [5].

Copyright © 2014 WILEY-VCH Verlag GmbH & Co. KGaA, Weinheim.

2.1.2 General random structure material fabrication

The same SUS304L grade stainless steel powder used for the fabrication of the harmonic-structure material was used here. First, the SUS304L powder was mechanically milled (MM) for 360 ks. Then, random-structure powder was manufactured by mixing the MM 360 ks powder and initial powder (IP) in the weight ratio of 1:1. The mixed powder was also sintered by the SPS process at 1123 K for 3.6

ks in vacuum under an applied pressure of 50 MPa. The average grain sizes of the coarse and ultrafine grains were 19.7 and 1.5 μm , respectively. Figure 2.2(c) shows the micro-structure of the SUS304L random-structure material obtained by EBSD. The ultrafine grain fraction was found to be approximately 20.4%, which is close to the corresponding value for the SUS304L harmonic-structure material.

Tensile experiments were conducted in a universal testing machine (Autograph AGS-10kND, Shimadzu), under displacement control. The specimens for tensile tests were manufactured by wire-spark cutting as a gauge length of 3mm and a cross-section area of $1 \times 1 \text{mm}^2$ of a mini I-beam.

Figure 2.3 shows a comparison of the nominal stress–strain curves of the harmonic and random structures [4,5]. It can be observed that the SUS304L harmonic- and random-structure materials have almost same strength and that the harmonic-structure material shows larger elongation than the random-structure material. FE analyses have been carried out to understand the effect of the network structure on the mechanical properties.

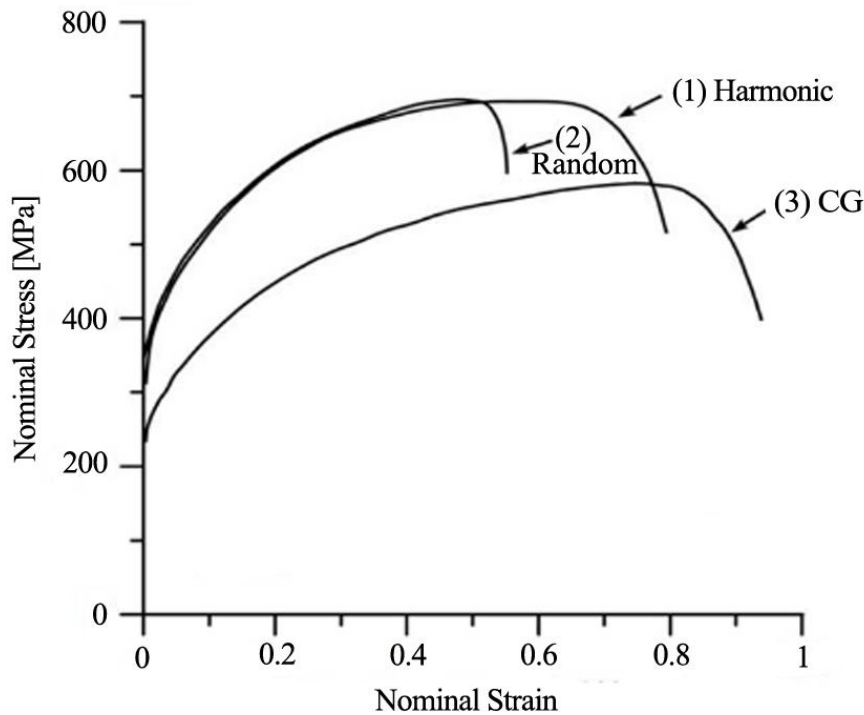


Figure 2.3: Comparison nominal stress-strain curves of the (1) harmonic structure, (2) random structure and (3) initial powder for SUS304L.

2.1.3 Kernel average misorientation results

Kernel average misorientation (KAM) during EBSD analysis can be applied as a measure of local grain misorientation. KAM quantifies the average misorientation around a measurement point with respect to a defined set of nearest neighbor points. In this research, the KAM images are employed as a way of measuring the dislocation density.

Figure 2.4 shows nominal stress-strain curve of harmonic structure and initial powder nickel. It clearly demonstrates the same tendency with harmonic structure SUS304L. Hence, the KAM image of Ni can represent the common performance of harmonic structure.

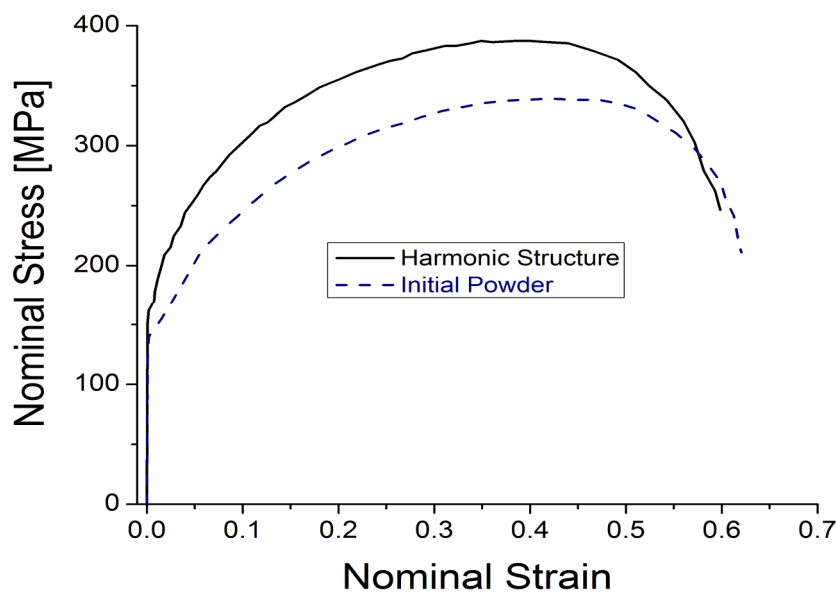
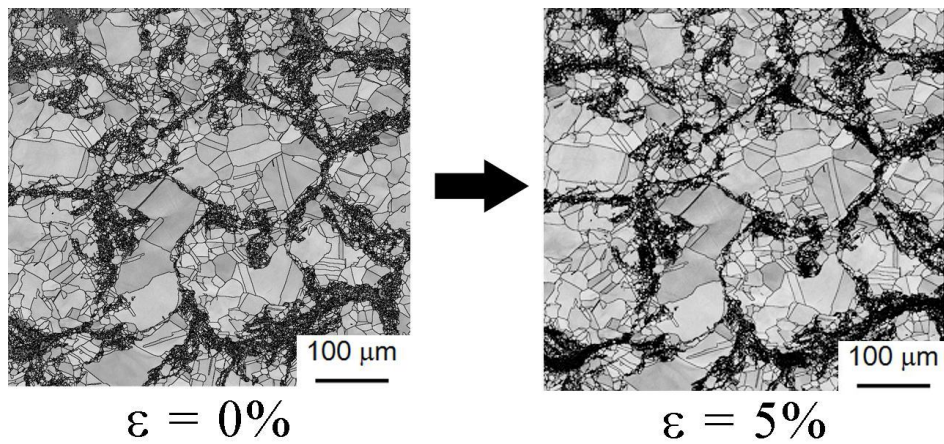


Figure 2.4: Comparison nominal stress-strain curves of the Ni (1) harmonic structure and (2) initial powder.

Figure 2.5 shows the micro-structure EBSD grain boundary images of Ni Harmonic Structure Compact before tensile test and in 5% strain. It can clearly demonstrate the connecting network structure of ultrafine grain region. Figure 2.6 shows the KAM images of Ni Harmonic Structure Compact before and after tensile test deformation corresponding to the EBSD grain boundary images shown in Figure

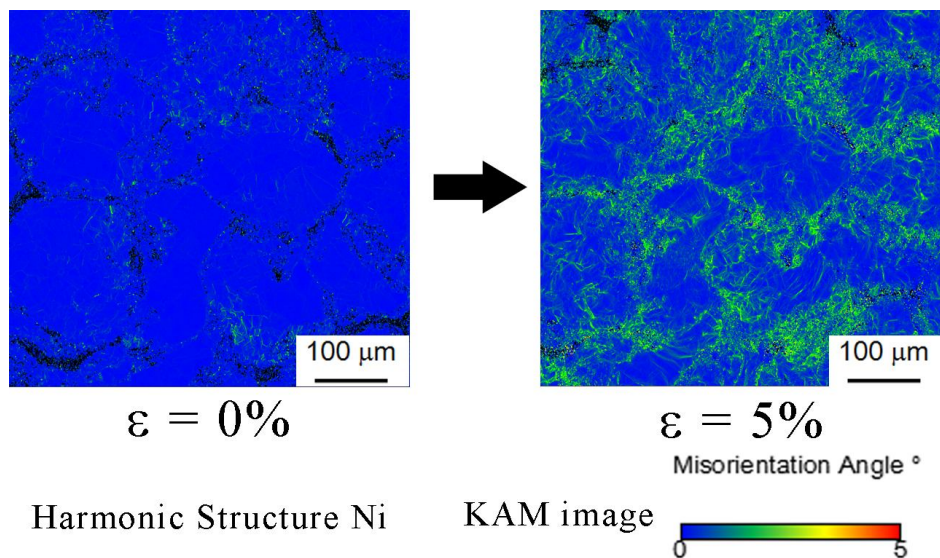
2.5. After deformation, the dark region in Figure 2.6 demonstrates the occurrence of high dislocation density. Besides, the dark region is match along with the shell region shown in Figure 2.5. The result demonstrates the high dislocation density happens in ultrafine shell region.



Harmonic Structure Ni

EBSD grain boundary image

Figure 2.5: The microstructure EBSD grain boundary images of Ni harmonic structure compact before and after tensile test deformation.



Harmonic Structure Ni

KAM image

Figure 2.6: The KAM image of Ni harmonic structure compact before and after tensile test deformation.

Figure 2.7 reveals the KAM images comparison of Ni (1) initial powder; (2) random structure and (3) harmonic structure compact in tensile test of $\varepsilon = 5\%$. From the results, it can be demonstrated that for Ni Initial Powder, dislocation density distribution shows uniform, while in Ni random structure and harmonic structure, the high dislocation density shows in ultrafine grain region. It reveals that, in the beginning of the tensile test, the stress location happens in the ultrafine grain region no matter in random structure or harmonic structure.

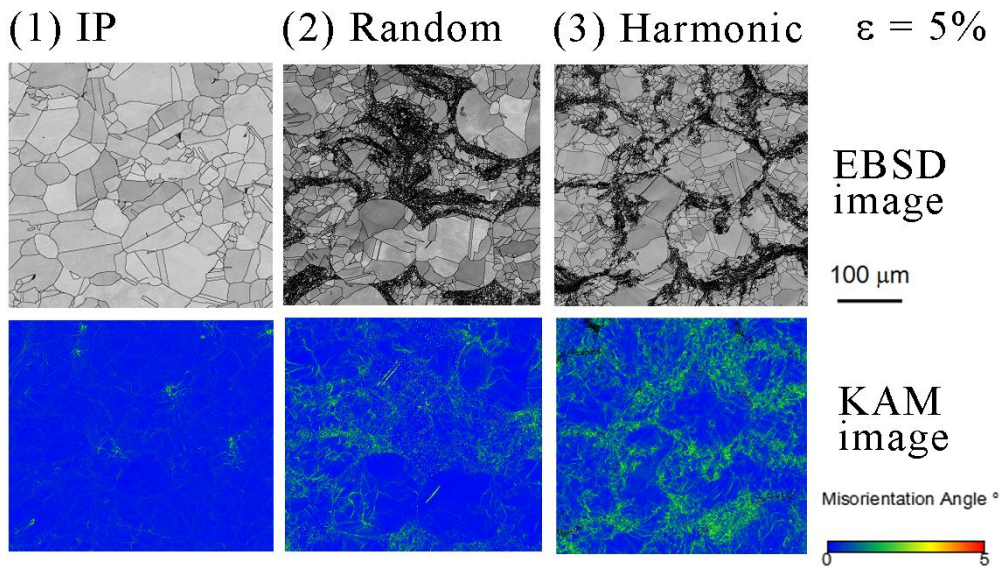


Figure 2.7: The EBSD grain boundary images and KAM images of Ni (1) initial powder; (2) random structure and (3) harmonic structure compact in tensile test of $\varepsilon = 5\%$.

2.1.4 Phase transition of harmonic structure material

However, the phase transition can also be a measurement tool of mechanical behavior. Figure 2.8 shows EBSD images and phase distribution of harmonic Co-Cr-Mo alloy specimen after 0%, 10%, and 20% tensile deformation, respectively [6]. The images above show the grain boundary of harmonic Co-Cr-Mo alloy as EBSD images, while the below images reveal the phase distribution. From the results, it can be revealed that the ε -hcp phase increased along with increasing degree of deformation. Furthermore, ε -hcp phase is almost happened in the ultrafine region,

which reveals the evidence that in the beginning of tensile test, higher stress happens in ultrafine region for harmonic structure.

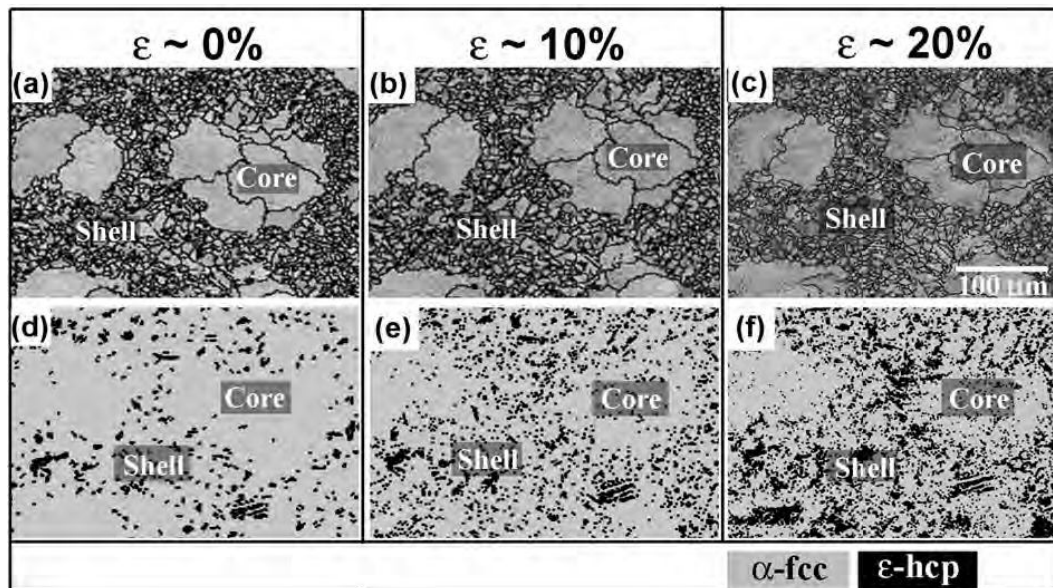


Figure 2.8: Distribution of ϵ -hcp phase with increasing plastic strain in the harmonic structured Co-Cr-Mo alloys:(a), (b) and (c) EBSD grain boundary images for the 0%, 5% and 20% strain deformation. (d), (e) and (f) corresponding phase distribution [6].

Copyright © 2015 Elsevier B.V.

2.2 FEM software introduction

2.2.1 ABAQUS CAE

In this research, Solidworks is used to built the model [7], ICEM-CFD is applied for meshing [8], while ABAQUS CAE is mainly employed to deal with the FEM problems [9]. In this research, we choose ABAQUS CAE because of the predominant nonlinear structure analysis from the dominant FEM softwares of ADINA, ANSYS, ABAQUS and MARC.

ABAQUS FEA (formerly ABAQUS) is a software suite for finite element analysis and computer-aided engineering, originally released in 1978. The name and logo of this software are based on the abacus calculation tool. The ABAQUS product suite consists of five core software products: ABAQUS/CAE; ABAQUS/Standard; ABAQUS/Explicit; ABAQUS/CFD; ABAQUS /Electromagnetic.

ABAQUS is used in the automotive, aerospace, and industrial products industries. The product is popular with academic and research institutions due to the wide material modeling capability, and the program's ability to be customized. ABAQUS also provides a good collection of multiphysics capabilities, such as coupled acoustic-structural, piezoelectric, and structural-pore capabilities, making it attractive for production-level simulations where multiple fields need to be coupled.

ABAQUS was initially designed to address non-linear physical behavior; as a result, the package has an extensive range of material models such as elastomeric (rubberlike) material capabilities.

Figure 2.9 shows GUI of ABAQUS. The content is the von Mises Stress distribution of the collapsed stick by XFEM simulation. The XFEM is a numerical technique based on the generalized finite element method (GFEM) and the partition of unity method (PUM). It extends the classical finite element method (FEM) approach by enriching the solution space for solutions to differential equations with discontinuous functions. The extended finite element method was developed to ease difficulties in solving problems with localized features that are not efficiently resolved by mesh refinement. One of the initial applications was the modeling of fractures in a material [10]. An ideal uniaxial tensile test was simulated in Figure 2.9.

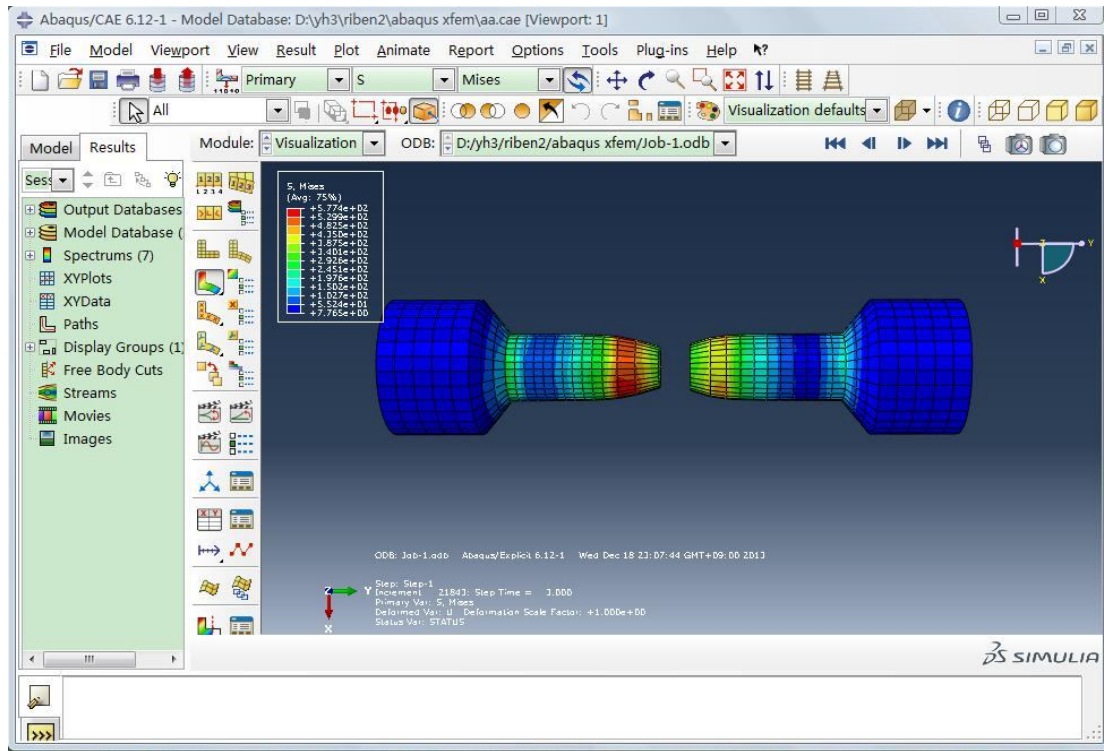


Figure 2.9: The graphical user interface (GUI) of ABAQUS.

2.2.2 Other software

Programming languages can be used to create programs to control the behavior of a machine or to express algorithms.

In this research, programming languages like C Language and Visual Basic have been used to deal with some mathematical problem to help to build the mesh, to set the boundary conditions or to do post treatment, while the FEM software themselves can no deal with the problem or do not have the functions required. A programming language is a formal constructed language designed to communicate instructions to a machine, particularly a computer.

In Chapter 4, I used a 3D computer graphics and computer-aided design (CAD) application software called Rhinoceros [11] to draw the Voronoi models.

References

- [1] Suryanarayana, C., 2001. Mechanical alloying and milling. *Prog. in Mat. Sci.* 46, 1-184.
- [2] Gogoti, Y., editor, *Nanomaterials Handbook*, Published by CRC Press, 2006, 364-365.
- [3] Chen, Y., Hjelen, J., Roven, H., 2012. Application of EBSD technique to ultrafine grained and nanostructured materials processed by severe plastic deformation: Sample preparation, parameters optimization and analysis, *Trans. Nonferrous. Met. Soc. China.* 22, 1801-1809.
- [4] Zhang, Z., Vajpai, S. K., Orlov, D., Ameyama, K., 2014. Improvement of mechanical properties in SUS304L steel through the control of bimodal microstructure characteristics. *Mater. Sci. Eng. A* 598, 106 - 113.
- [5] Zhang, Z., Orlov, D., Vajpai, S. K., Tong, B., Ameyama, K., 2015. Importance of Bimodal Structure Topology in the Control of Mechanical Properties of a Stainless Steel. *Adv. Eng. Mater.* 17(6), 791-795.
- [6] Vajpai, S. K., Sawangrat, C., Yamaguchi, O., Ciuca, O. P., Ameyama, K., 2016. Effect of bimodal harmonic structure design on the deformation behaviour and mechanical properties of Co-Cr-Mo alloy. *Mater. Sci. Eng.: C*, 58, 1008-1015.
- [7] LOMBARD, M. *SolidWorks 2010 bible* / Matt Lombard. Indianapolis, IN : Wiley Pub., 2010.
- [8] Wikibooks: ICEM CFD. https://en.wikibooks.org/wiki/ICEM_CFD.
- [9] ABAQUS/CAE. Hibbitt, Karlsson & Sorensen, 2002.
- [10] Wikipedia: Extended finite element method.
https://en.wikipedia.org/wiki/Extended_finite_element_method.
- [11] Rhinoceros 3D, wikipedia. https://en.wikipedia.org/wiki/Rhinoceros_3D.

Chapter3: Modeling of harmonic structure

It is well known that the FEA is usually applied in the research related with the evaluation of the reliability and integrity of various structural units under loads. However, in order to meet the requirement of the research of heterogeneous materials mechanical properties, the multi-scale FEA has been used. Nowadays, micro-mechanical analyses have been on an increasing trend in order to understand the behavior of modern materials with sophisticated micro-structures. The multi-scale FEA is applying the micro-scale model to describe the characteristics of macro-scale object. Periodic boundary condition is the bridge between the micro composition and the macro object. By using the micro structure model with periodic boundary condition, we can get the stress and strain distribution of micro structure and the macro characteristic as stress-strain curve of object. In this chapter, the micro scale model with periodic boundary condition for harmonic structure is built.

3.1 Periodic boundary condition

3.1.1 Periodic boundary condition in mathematics

The basic idea of using periodic boundary conditions is to assume that a structural part at the macro level consists of a number of repeated microscopic units. The periodic boundary condition is the bridge that connects the microscopic units with the macro object. Allaire (1992) developed a foundation for periodic micro-structures based on mathematical homogenization theory to specify the micro/macro-scale coupling boundary value problem (BVP) [1]. Using a two-scale FE analysis method, Guedes and Kikuchi (1990) and Terada et al. (2003) developed an FE method to solve the derived two-scale BVP [2,3]. The mathematical framework of the two-scale BVP has a unique feature in that the microscopic BVPs act as constitutive models for the macroscopic BVP. By reducing the macroscopic BVP to a macroscopic stress–strain

relationship and controlling the macroscopic stress or strain, researchers carried out the FE analysis of periodic micro-structures [4-12].

To determine the global constitutive law of a material at the macro level, the transformation of the corresponding surfaces should be restricted to coupling. This restriction leads to parallelism between the corresponding surfaces in the microscopic unit. In terms of a mathematical expression, any displacement on one side of a representative unit cell (RUC) must be the same as that on the opposite side of the RUC plus or minus a constant for structure analysis [6].

The periodic boundary condition for the heat analysis is not discussed in this research. For periodic boundary condition of heat analysis, the displacement for the opposite edges of the RUC can not be set, while the heat flux for the opposite edges should be same.

The equation below shows the diagrammatic sketch for 2D periodic boundary condition applied in a RUC rectangle for structure analysis [6]. The square's side - length is L. A0 locates at the origin of the coordinate plane. A1 and A2 locate at the x-axis and y-axis, separately (Figure 3.1). The points on the opposite sides should fulfill the equations below.

$$\begin{aligned}\bar{u}(L, y) &= \bar{u}(0, y) + (\bar{u}_{A1} - \bar{u}_{A0}) && \text{(x-direction displacement)} \\ \bar{u}(x, L) &= \bar{u}(x, 0) + (\bar{u}_{A2} - \bar{u}_{A0}) && \text{(y-direction displacement)}\end{aligned}\tag{Eq.1}$$

In the equations, the \bar{u}_{Ai} means the displacement of the Ai point. (i=0,1,2)

After applying the equations above for structure analysis, the origin cube can be deformed as the figure 3.2 shows. After deforming, the edges of the cube can not be straight, but they should be parallel with matching edges. Hence, by extending the same unit one by one, they can constitute a large graph without holes and overlapping regions. Parallelism is a significant characteristic in the periodic boundary condition of structure analysis.

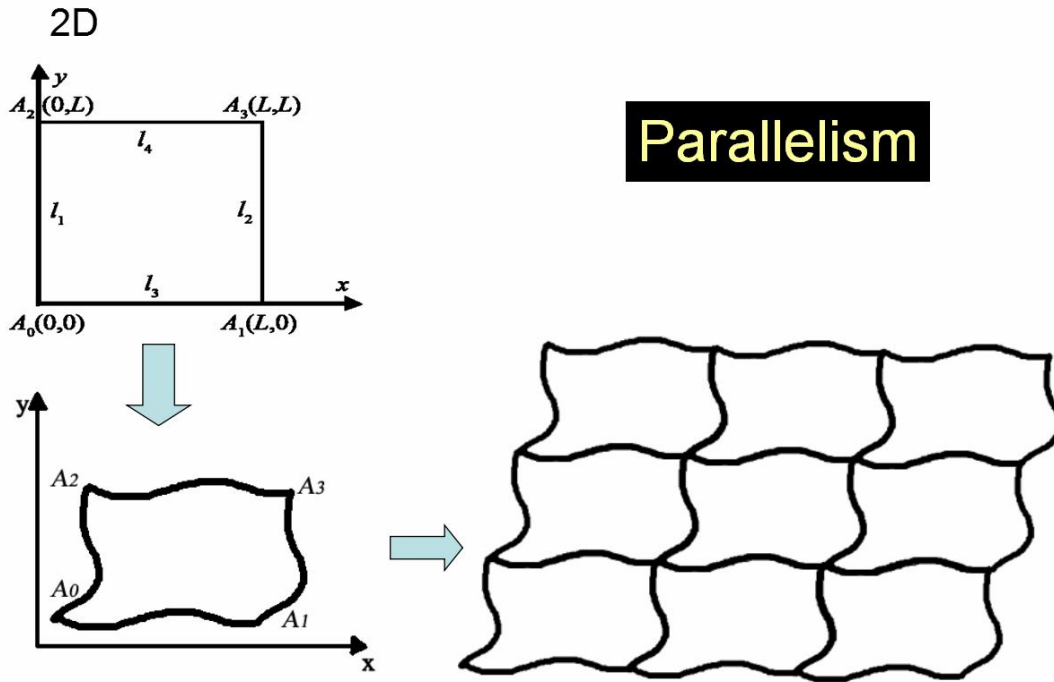


Figure 3.1: The parallelism characteristic in the periodic boundary condition of structure analysis.

Extending the 2D equations to the 3D model of orthogonality cube with the side-length L , the equation can be [5,7]:

$$\bar{u}(L, y, z) = \bar{u}(0, y, z) + \varepsilon \bar{x} \quad (\text{x-direction displacement})$$

$$\bar{u}(x, L, z) = \bar{u}(x, 0, z) + \varepsilon \bar{y} \quad (\text{y-direction displacement})$$

$$\bar{u}(x, y, L) = \bar{u}(x, y, 0) + \varepsilon \bar{z} \quad (\text{z-direction displacement}) \quad (\text{Eq.2})$$

Here, $\bar{u}(x, y, z)$ represents the displacement vector of the point with the coordinate x, y, z . ε represents the macroscopic strain tensor. $\varepsilon \bar{i}$ ($i = x, y, z$) is a constant representing the i -direction displacement difference for a pair of surfaces. This indicates that the displacement of a point in the surface represented by $i = 0$ maintains the difference in $\varepsilon \bar{i}$ compared to the displacement of the matching point in the surface represented by $i = L$ (the other two coordinates except i are the same). The constant $\varepsilon \bar{i}$ guarantees parallelism for a pair of surfaces. Even in the process of

displacement in which the origin plane surfaces may change to curved surfaces, a pair of curved surfaces should also be able to maintain parallelism.

3.1.2 Programming of periodic boundary condition for ABAQUS

In FE solver ABAQUS, in order to fulfill the equation above, three dummy nodes should be considered. These nodes should be matched to three pairs of surfaces. Thus, the displacements of the dummy nodes will replace the constants in the equation.

Figure 3.2 shows the command applied to fulfill the periodic boundary condition in ABAQUS, *EQUATION, which belongs to the constraint command [13]. The command "EQUATION" contains two lines to describe an add operation which the result equals zero. First line is for number of nodes, while the second line describes the node number, degree of freedom, value of coefficient, the other node number, its degree of freedom, value of coefficient, the next node number and so on. The command "EQUATION" can be used for many types for constraint. For example, the coupling of degree of freedom (DOF) is choosing one node in the surface as the drive node and the remaining nodes in the surface should keep the same displacement in normal direction of the surface. In a free FEM soft Front-ISTR, the coupling of DOF should be achieved by writing the program. In ABAQUS, there is a command to build the coupling of DOF directly. However, there is not a direct command for periodic boundary condition for structure analysis. We should employing the "EQUATION" to write the periodic boundary condition.

$$\bar{u}(L, y, z) = \bar{u}(0, y, z) + \varepsilon \bar{x}$$

↓

$$(-1) * \bar{u}(L, y, z) + \bar{u}(0, y, z) + \varepsilon \bar{x} = 0$$

The diagram illustrates the ABAQUS EQUATION command used to implement a periodic boundary condition. The command is: `*EQUATION, 3, 4348, 1, -1, 7550, 1, 1, 10814, 1, 1`. The components are annotated as follows:

- `3`: 3 items in this equation
- `4348`: Node number in paired surface
- `1`: Node number in basement surface
- `-1`: constant
- `7550`: Dummy node number
- `1, 1, 1`: 1 x, 2 y, 3 z

Figure 3.2: Constraint command used the “EQUATION” to deal with the periodic boundary condition for structure analysis in ABAQUS.

In the mathematic theory of the periodic boundary condition, it seems that just displacement definition of the matching point of the pair surfaces is required. Therefore, in mesh process, the nodes' coordination of the pair surfaces should be put into a one-to-one relationship, respectively. However, in order to build the program process successfully, there are three significant and error-prone points in the programming.

First point is the sequence of the equation. In the mathematic theory, $x+y=0$ and $y+x=0$ have the same meaning. While in the FEM simulation, they are the different equations. In FEM constraint command, the parameters are distinguished between passive node and initiative node. The nodes in the left three surfaces are the passive nodes which are determined by the initiative nodes in the three coordinate surfaces. Therefore, the passive node should be the first item in the equation, while the initiative node is the second item and the difference value is the third item. For example, in coupling of DOF, if the first node in the equation is drive node, the analysis will report error because of redefinition. For periodic boundary condition, the

order of the equation items is also important.

Second point is the coordinate deviation of the matching nodes. Although in modeling, the rectangular parallelepiped cube is employed for the physical form which the outside edges are paralleled to the xyz-axis and while in meshing, the nodes' coordination are supposed to be one-to-one relationship, owing to the decimal digits as eight, sometimes there will be the deviation in the coordinate. It means that 1.00000001 is not equal 1 in mathematics but it should be regarded as the corresponding nodes in soft. So the setting of deviation is significant in programming. While the coordinate deviation is changed with the model size and the mesh refinement, the deviation should be a revisable option as Figure 3.3 shows. The value of deviation should be very small, because there is possibility that the neighbor nodes are regarded as one node when the value of deviation is large. Hence, a supervisor status should be added in this soft. The deviation has been used twice. First time is about the statistics of the nodes in the max/ min surfaces. Because the nodes in the corresponding surfaces matched one by one, if the numbers of corresponding surfaces nodes are different, the calculation is wrong, which should be written in the supervisor status. Second time is that each node in surface finds the corresponding node in the matching surface. It is necessary to confirm every node in surface is matched with the node in the matching surface. The matched nodes in the matching surface should be all applied and they can be used only time. I set arrays to describe the nodes. Hence, there is a variable (Figure 3.3) in the array to represent the status if the node has been used. After these two times check, the inp file for ABAQUS can be built.

With the deviation setting, the inp file can be built and ABAQUS can read the inp file successfully. However, error message happened in simulation in ABAQUS.

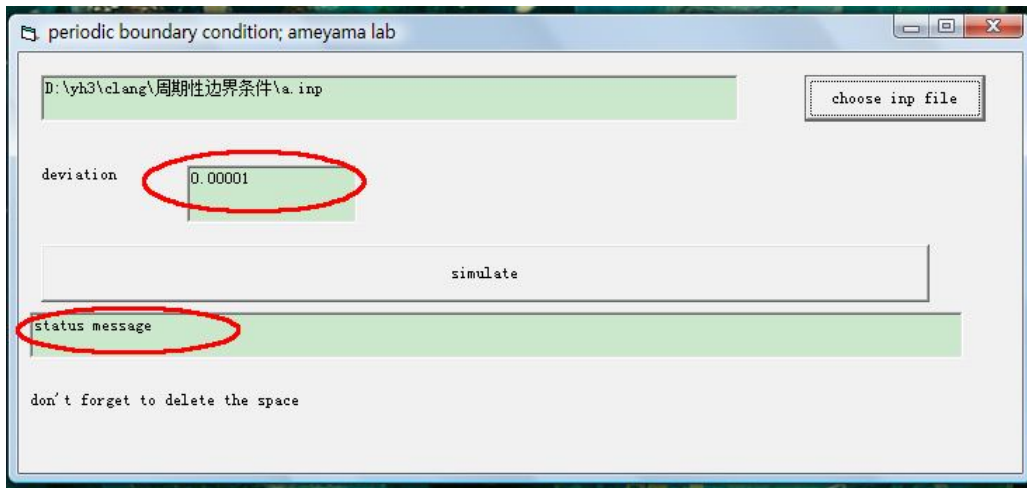


Figure 3.3: The alterable deviation setting by user in the soft; The status message to make sure the periodic boundary condition setting successfully.

Third point is about the nodes with over constraint freedom. While in the mathematic theory, the passive nodes are determined by initiative nodes no matter how many times the passive nodes have been multiplicity defined because there is the connection relationship in the nodes so the results are same. But in the ABAQUS, it will report the error because of the over constraint freedom and the over constraint freedom passive nodes would be treated as slave nodes. As a matter of fact that slave passive nodes are not just in one passive surface but in the juncture of the passive surfaces, so the nodes are used as passive nodes two times or three times. For example, if $x = 1$ and $y = 1$, then we define that $z = x$ and $z = y$. In mathematics, there is no problem because $z = x = y = 1$. However, in programming, this is duplicate definition. In order to solve this problem, the juncture passive nodes should be treated specially.

Suppose that, the surfaces on the $xy/yz/zx$ surfaces are the initiative surfaces, the left three surfaces are passive surfaces. Figure 3.4 shows the slave juncture passive nodes as the blue nodes which should be treated specially, because in the Figure 3.4, the displacements of the slave blue nodes have been defined twice or thrice. At the same time, the red initiative nodes (closed to origin of the coordinate) have also been used twice or thrice. As they are initiative nodes, multiplicity using would not show the error, but it is still a repeat definition.

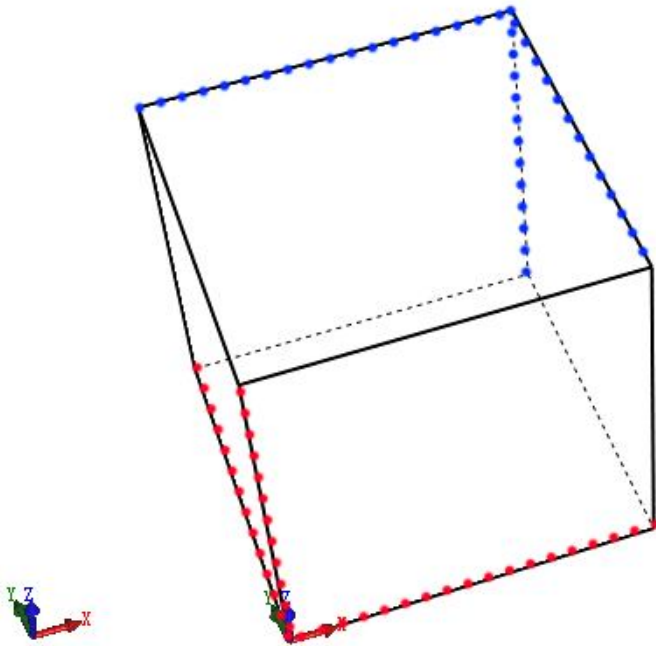


Figure 3.4: The nodes used twice and thrice in the periodic boundary condition without distinguishing special nodes.

The equation chain has been raised to solve this problem. The nodes of vertexes and nodes in the edges should be solved, respectively.

First, the nodes amount of vertexes in a cube is eight. There is equation chain as the Figure 3.5 shown which explains the relationship of the vertexes so there is no repeat definition. Thanks to this equation chain, every vertex's displacement has been guaranteed to be defined. In Figure 3.5, A0 locates at the origin of the coordinate system. A0 is the originally initiative vertex. Other vertexes are connected to A0 by the chain as the Figure 3.5 shown. It demonstrates that A0 decides A1, A1 decides A2 and so on. The words near the blue arrows mean the difference value between the initiative node and passive node. As the three dummy nodes defined previously demonstrate difference value of three pair surfaces, they also have the direction. For example, $-y$ means opposite direction of $\bar{\varepsilon}y$, so in the equation, modulus of $\bar{\varepsilon}y$ is -1.

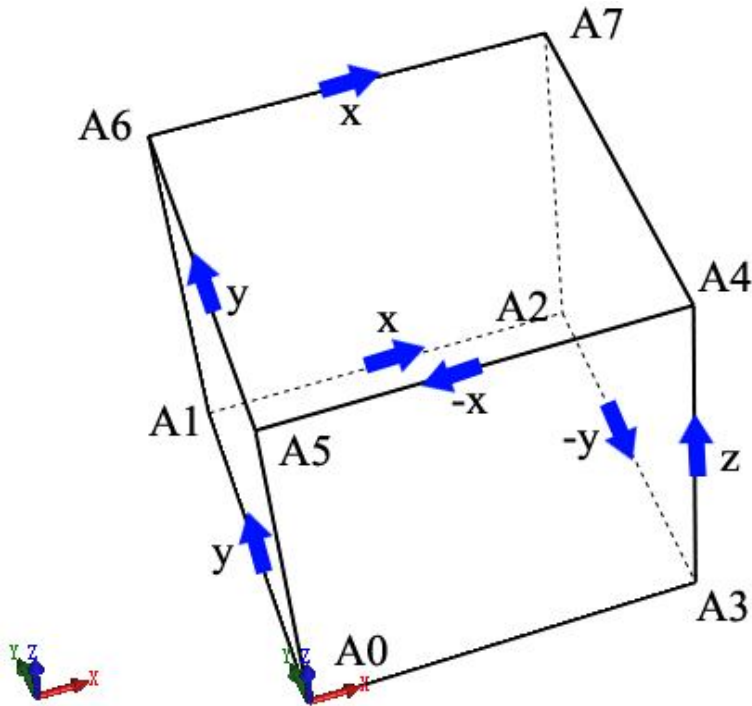


Figure 3.5: Special treatment for the vertexes of periodic boundary condition.

Second step is for the nodes in the juncture edges except the vertexes. It can be separated into three groups, x/y/z axis. The blue dots are imaged as the nodes in the edges except the vertexes. As the Figure 3.6 shown, the nodes on L0 decide the displacement of L1 corresponding nodes. Then L1 nodes decide the L2 nodes and so on. Through this way, all the nodes in the edges can be defined.

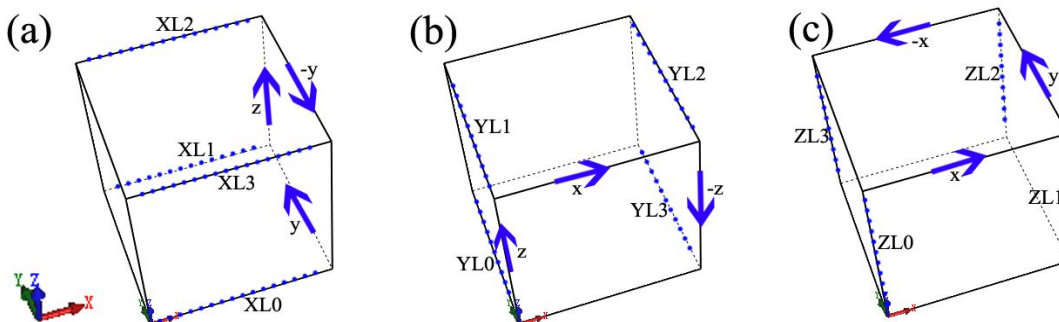


Figure 3.6: Special treatment for the nodes on the edges of periodic boundary condition.

As the Figure 3.7 shown, because the juncture slave nodes are all handled, then the remaining nodes on the matching surfaces can be treated normally. Finally, the periodic boundary condition was created, and the displacement of the model can be controlled by the three dummy nodes.

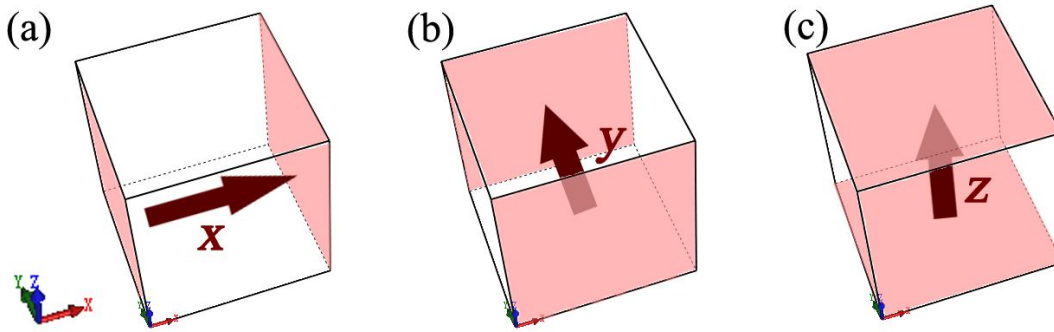


Figure 3.7: Dealing with the remaining nodes in the surfaces.

Figure 3.8 shows the flow chart of periodic boundary condition program for ABAQUS. In this programming, we should notice the different positions of the nodes we used, and the validation checking is significant.

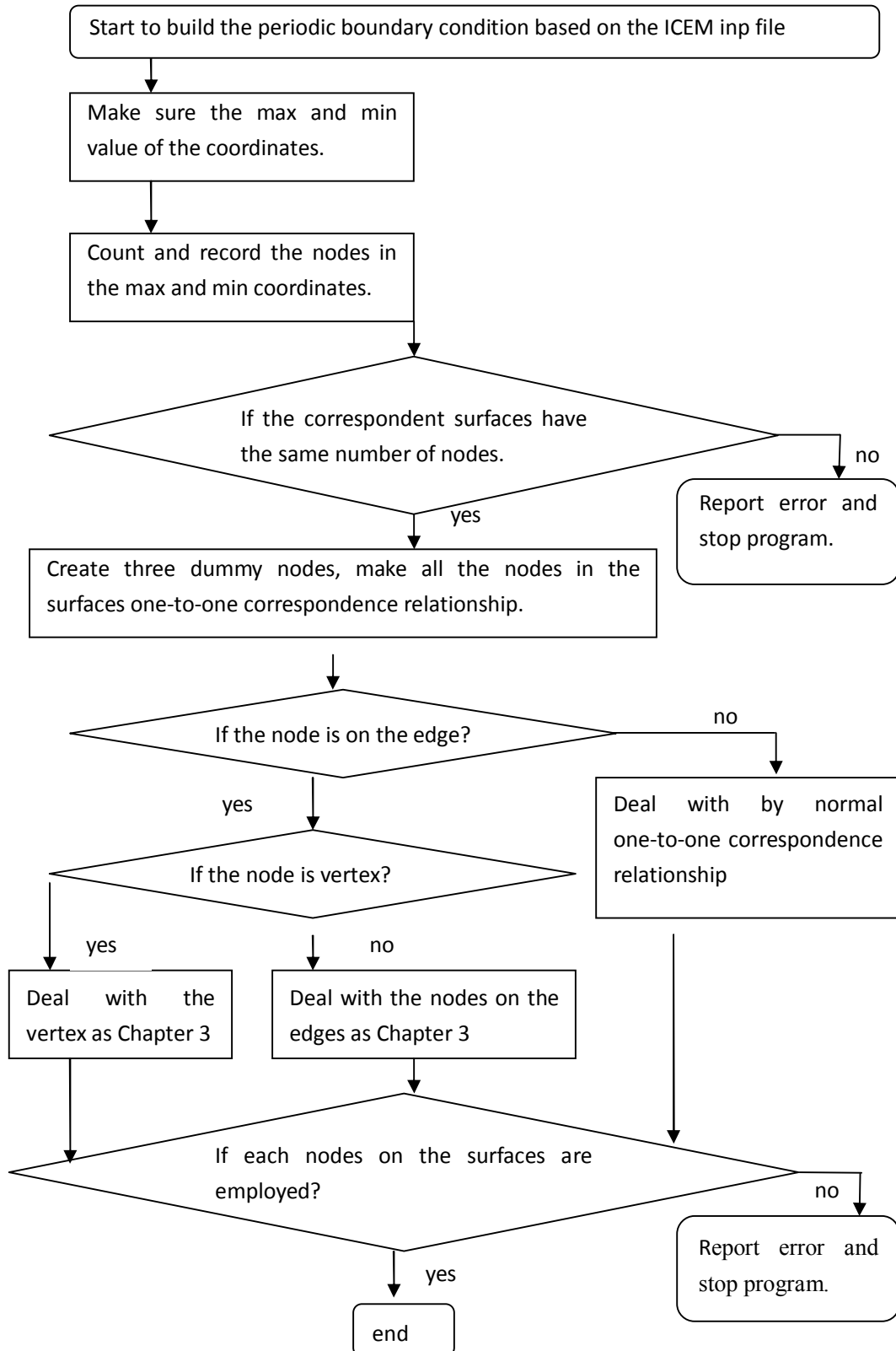


Figure 3.8: Flow chart of periodic boundary condition program for ABAQUS.

After compiling the program for periodic boundary condition and applying it for ABAQUS, therefore, the displacement boundary condition can be added in the dummy nodes (Figure 3.9).

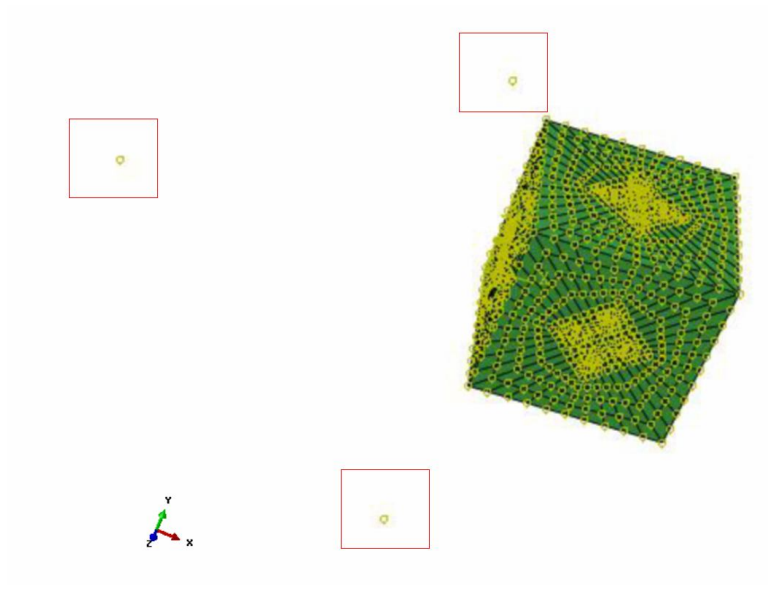


Figure 3.9: The effect of periodic boundary condition in ABAQUS.

Another method to set the periodic boundary condition in ABAQUS is using the original nodes as the difference value of displacement [14]. As Figure 3.10 shown, displacements of node X, Y, Z in the vertex angle are employed as the difference values of pair curved surfaces' displacement relative to base node, directly. The origin node is fixed as the reference substance node. The remaining steps are as same as the periodic boundary condition setting with dummy nodes. However, in the mathematic theory, these two methods share the same theory. Nevertheless, in simulation process, using the original nodes will make the three original nodes as the driving nodes. It will bring a little difference between these three original nodes and other nodes in the surfaces. Even though the difference is too little to be mentioned in the plastic region, it will bring a visible aberration for the driving nodes in Von Mises Stress distribution within elastic region because of young's modulus. Although the strain difference is

extremely small, it will still influence Von Mises Stress distribution in elastic region. The unique driving nodes will show displacement faster than other nodes in the very beginning of the plastic region. Figure 3.11 shows the Von Mises Stress distribution within elastic region for the periodic boundary condition with and without dummy nodes. For the model using the original nodes as the drive point, it can be clearly observed that mainly regions show value as 42 MPa, while the values of vertexes are nearly 97 MPa. The value of vertexes show about 131% inaccuracy compared to other nodes, while it should be a uniform value due to uniform mechanical properties in elastic region. Although in the plastic region, the inaccuracy will be ignored due to the large gap between CG and UFG characteristics, the vertexes show incorrect values in the elastic region. However, for the model using dummy nodes, the nodes on the tensile surfaces show relatively higher value as 44.8 MPa, while the nodes in the center show relatively lower value as 44.4MPa. The inaccuracy is about 0.9%.

Hence, importing the dummy nodes makes the nodes displacements in the pair curved surfaces unifying and reduces aberration.

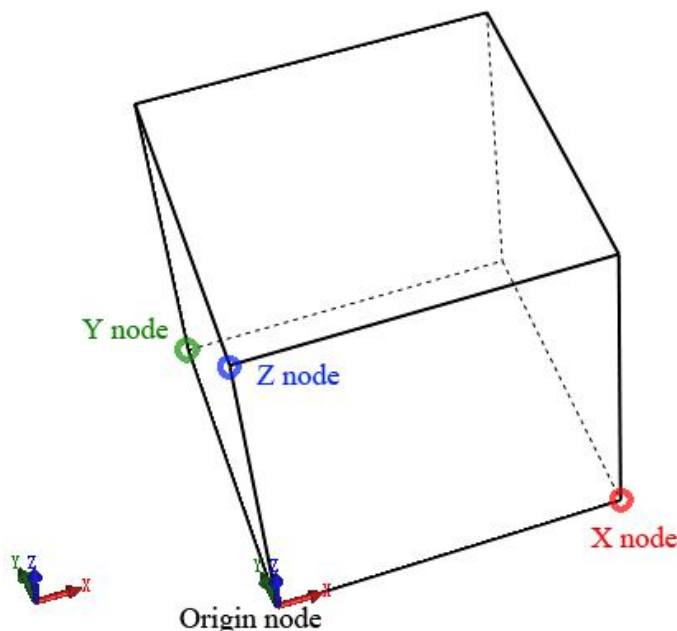


Figure 3.10: Setting the periodic boundary condition in ABAQUS by using the original nodes as the difference value of displacement.

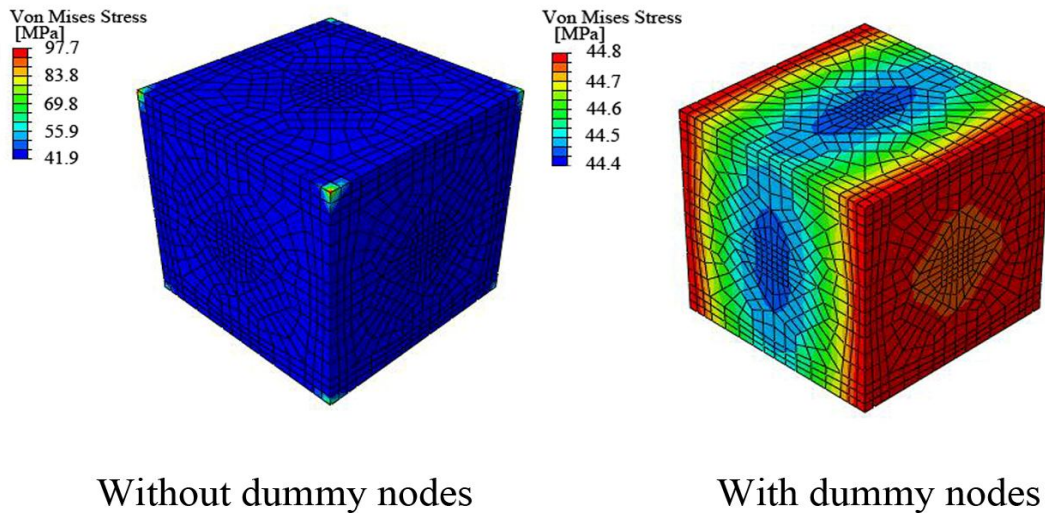


Figure 3.11: Von Mises Stress distribution in early elastic region with and without dummy nodes for periodic boundary condition.

3.2 Finite element model for harmonic structure

3.2.1 Geometry basement: truncated octahedron

To obtain macroscopic averaged properties from a heterogeneous microstructure, the concept of a representative volume element (RVE) has been employed. An RVE has been defined as a part extracted from a complete microstructure to homogenize the heterogeneity of the microstructure. Especially, a periodic microstructure has been defined as an RVE in computational approaches using discretization methods such as the FE method in general.

In geometry, the truncated octahedron (Figure 3.12) is an Archimedean solid. It has 14 faces (8 regular hexagonal and 6 square), 36 edges, and 24 vertices. Since each of its faces has point symmetry the truncated octahedron is a zonohedron. A truncated octahedron is constructed from a regular octahedron with side length $3a$ by the removal of six right square pyramids, one from each point.

In this research, a truncated octahedron is used to constitute the RVE of the harmonic-structure model for the FE analyses owing to its efficient space-filling characteristic. The arrangement of the truncated octahedron can form a bitruncated cubic honeycomb, which can be realized as a body-centered cubic lattice [15-19]. Chantarapanich et al. (2012) geometrically evaluated a scaffold library for tissue engineering [16]. The evaluation results revealed that the close-cellular scaffold included a truncated octahedron, rhombicuboctahedron, and rhombitruncated cuboctahedron. In addition, polyhedrons suitable for use as open-cellular scaffold libraries included a hexahedron, truncated octahedron, truncated hexahedron, cuboctahedron, rhombicuboctahedron, and rhombitruncated cuboctahedron. The truncated octahedron and other polyhedrons have already been investigated.

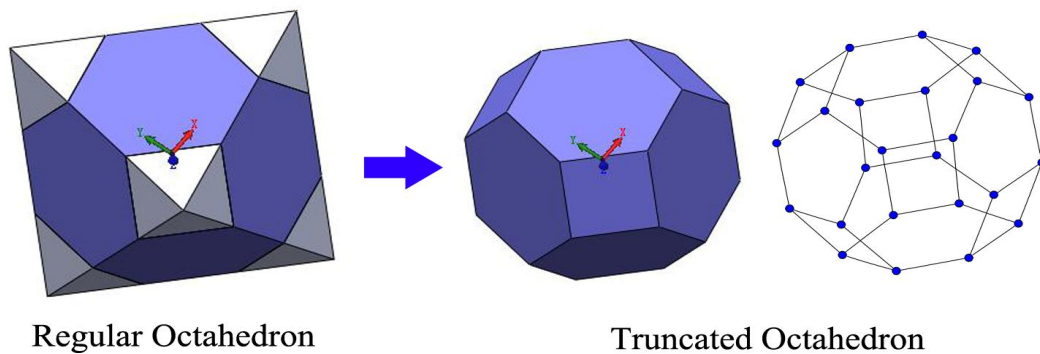


Figure 3.12: Method to achieve the truncated octahedron.

Figure 3.13 shows the harmonic-structure material composed of the CG cores and UFG shell. Because of efficient space filling, this model can maintain almost the same thickness as the actual object throughout the shell. In contrast to this research, a sphere is often chosen as the shape of an inclusion in FE models, in which the range of the volume fraction is limited.

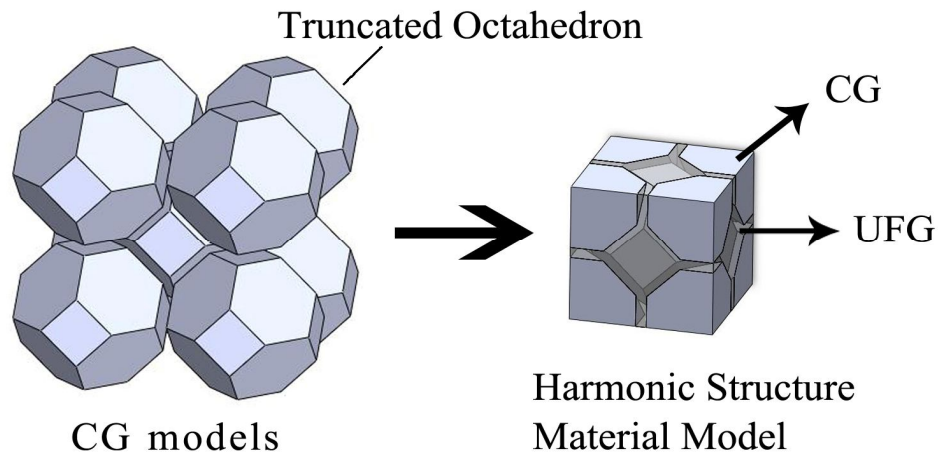


Figure 3.13: Harmonic structure model constituted by truncated octahedron.

3.2.2 Block dividing of harmonic structure model for meshing

Thanks to the symmetry, $1/8$ of the model can be employed in mesh process. In this research, the hexahedral mesh has been chosen considering the regular shape of a truncated octahedron. The hexahedral mesh is preferred to the tetrahedral mesh in FE methods for numerical simulation owing to reduced error and a smaller number of elements. However, building hexahedral mesh is more difficult than tetrahedral mesh because it is not an automatic process but handy process. Moreover, because hexahedral mesh is not generic, in order to obtain the hexahedral mesh, hexahedral blocks should be applied [20]. The model is combined by some hexahedral blocks, because the model is not a regular shape. A large block for the model is defined. Through dividing and distortion, it has become some smaller hexahedral blocks. Then the blocks' vertices, edges, faces should be associated to the model's points, curves, surfaces. Figure shows the blocks of $1/8$ harmonic structure model.

In blocking methods, the most significant thing is to make every block as the hexahedron, therefore, the Y-grid, O-grid and C-grid and L-grid method are widely applied for meshing (Figure 3.14). Y-grid is often used to deal with the triangular prism shape, which is applied to divide a triangular prism into 3 hexahedrons.

However, O-grid is often employed to handle cylinder shape, which makes the arrangement of blocks as ray and evades the bad mesh quality in the angle of original cube. C-grid and L-grid are $3/4$ and $1/2$ O-grid, respectively. For the specific steps of setting blocks for the harmonic structure, first step is to make a $1/8$ truncated octahedron. Then after mirroring and rotating, two $1/8$ truncated octahedron parts which are used to be cores have been prepared. After extending the faces of blocks and merging the vertexes, the shell region has been established. Finally, the blocks of $1/8$ model have been divided.

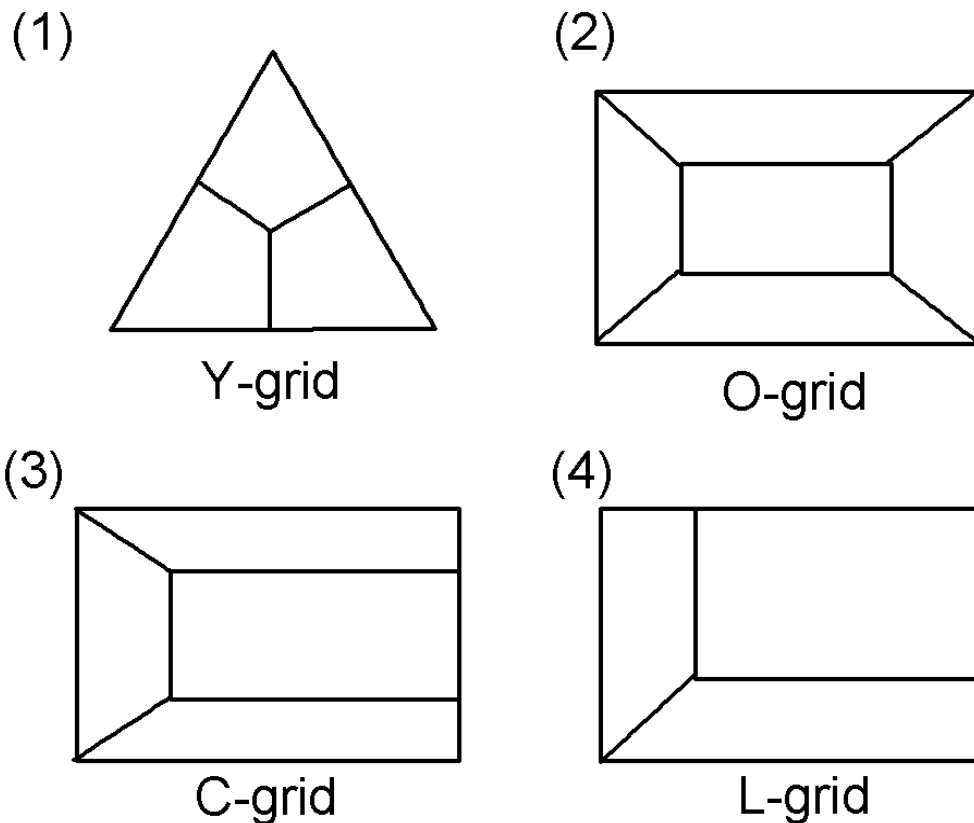


Figure 3.14: Significant block dividing methods. (1) Y-grid; (2) O-grid; (3) C-grid and (4) L-grid.

The block dividing procedure for harmonic structure is shown in Figure 3.15. On the whole, in this research, the generalized steps are: first, building one $1/8$ core; second, building another $1/8$ core by copying and rotating it; third, stretching the shell

region. Hence, blocks for the $1/8$ model (Figure 3.16) can be generated.

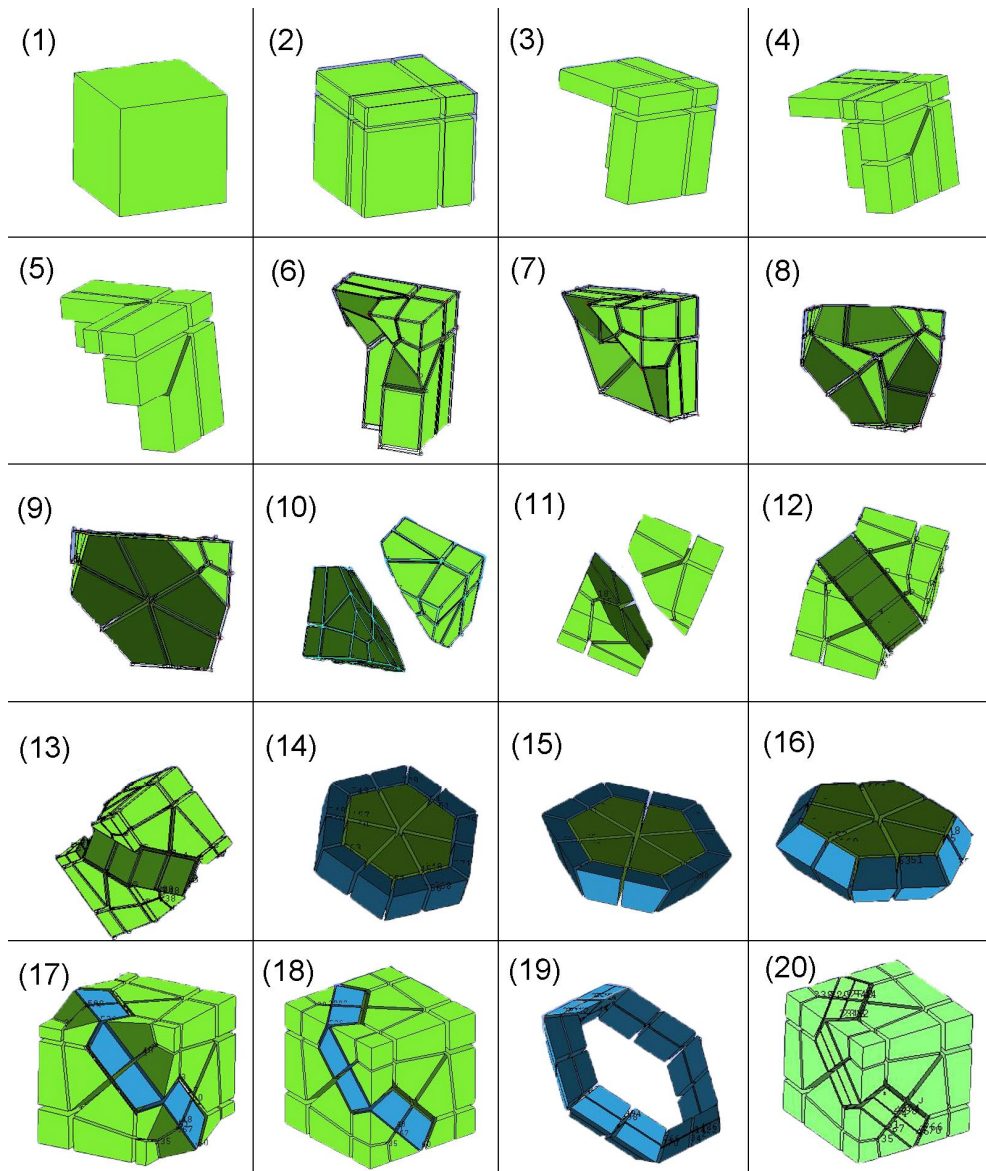


Figure 3.15: The block dividing procedure for harmonic structure.

3.3 Material characteristics of CG and UFG based on

Hall-Petch rule

An isotropic elastoplastic constitutive model based on Hooke's elasticity and Von Mises-type plasticity has been employed for the CG and UFG phases in this study. The isotropic hardening is employed in the setting for the plastic characteristics for CG and UFG phases. The same elastic constants of SUS304L are used: i.e., Young's modulus of 194,020 MPa and Poisson's ratio of 0.25. The user-defined material model (UMAT) has not been employed in this research. Hence, plastic deformation gradient (dfgrd) has not been defined.

For plasticity, the relationship between the equivalent stress and plastic strain should be determined. In the present work, the average grain size of the existing homogeneous CG SUS304L material is 35.0 μm . Qu et al. (2008) investigated the mechanical properties of homogeneous UFG SUS304L material with grain size of 1.0 μm [21]. Furthermore, the grain sizes of the CG and UFG materials of the SUS304L harmonic structure are measured to be 17.6 and 2.0 μm , respectively, by EBSD. The known yield stress values of the existing homogeneous CG SUS304L material and homogeneous UFG SUS304L material are 251 and 652 MPa, respectively. Therefore, using the Hall-Petch relationship (Eq.2, Figure 3.18) [22,23], the yield stress values of the CG and UFG materials of the SUS304L harmonic structure can be calculated to be 284 and 530 MPa, respectively.

$$\sigma = \sigma_0 + k \times \frac{1}{\sqrt{d}} \quad (\text{Eq.3})$$

Where σ is the yield stress, σ_0 is the lattice friction stress required to move individual dislocations, k is a constant, and d is the grain size. For the MM 180 ks SUS304L harmonic-structure material, σ_0 is 169 MPa and k is 483 $\text{MPa} \cdot \mu\text{m}^{0.5}$.

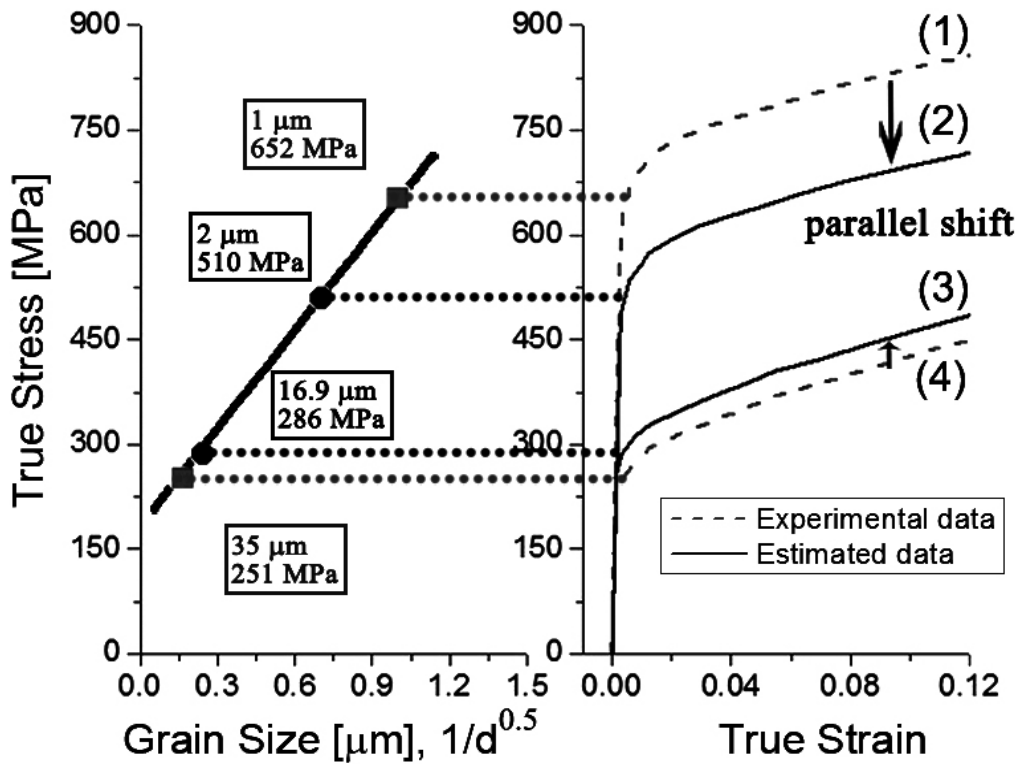


Figure 3.18: The estimated s-s curve of CG and UFG based on Hall-Petch rule.

In this research, not just the yield stress but also the stress–strain curve of the CG and UFG materials is required for the simulation. To imitate the stress–strain curve of the UFG and CG materials in the harmonic structure, the yield stress is calculated by the Hall–Petch relationship (Eq.2), and the shape of the stress–strain curve is maintained according to the nature of the nearby yield stress material. In Figure 3.18, the top and bottom dashed curves are the true stress–strain curves for the experimental homogeneous UFG and CG data, respectively. By the parallel shifting of the true stress–strain curves, the estimated true stress–strain curves (solid curves) of the UFG and CG materials of the SUS304L harmonic structure are obtained. These estimated curves are used for the FE analyses.

After material characteristics have been set, simulation parameters should be settled. In this research, the general state structure simulation has been chosen. Figure

3.19 shows the parameters of the harmonic structure finite element analysis. In this research, because not dynamic structure simulation which is often chosen to solve impact problem but just static structure simulation has been applied in this research, it has been validated that the result always keep same no matter how time period option changed. Hence, in order to guarantee the convergence, the time period option can be more while rising the time period will extend the simulation duration.

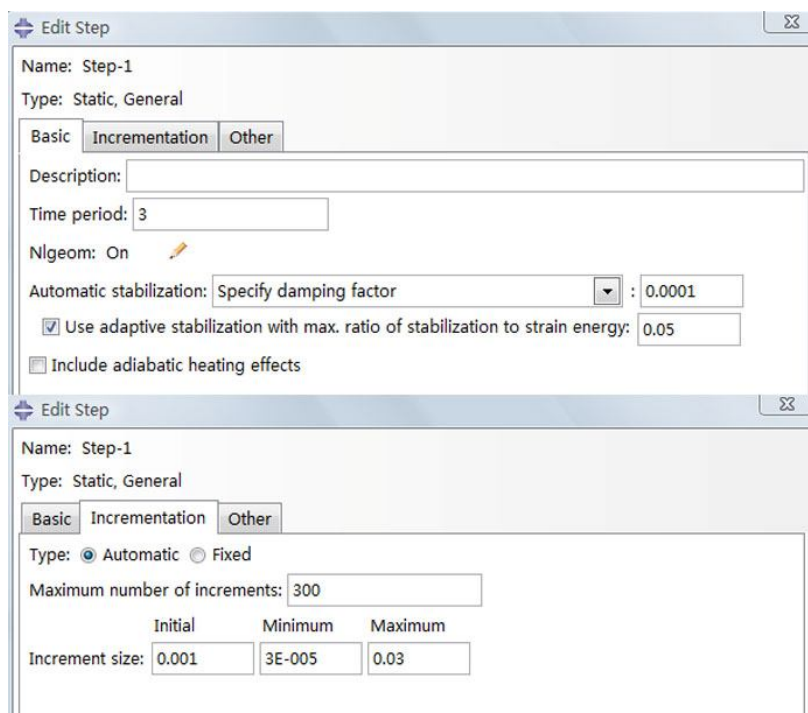


Figure 3.19: The parameters for simulation step setting.

References

- [1] Allaire, G., 1992. Homogenization and two-scale convergence. *SIAM J. Math. Anal.* 23 (6), 1482 - 1518.
- [2] Guedes, J., Kikuchi, N., 1990. Preprocessing and postprocessing for materials based on the homogenization method with adaptive finite element methods. *Comput. Meth. Appl. Mech. Eng.* 83 (2), 143 - 198.
- [3] Terada, K., Saiki, I., Matsui, K., Yamakawa, Y., 2003. Two-scale kinematics and

- linearization for simultaneous two-scale analysis of periodic heterogeneous solids at finite strain. *Comput. Meth. Appl. Mech. Eng.* 192 (31C32), 3531 - 3563.
- [4] Watanabe, I., Terada, K., 2010. A method of predicting macroscopic yield strength of polycrystalline metals subjected to plastic forming by micro–macro de-coupling scheme. *Int. J. Mech. Sci.* 52 (2), 343 - 355.
- [5] Zhang, C., Xu, X. W., Yan, X., 2013. General periodic boundary conditions and its application on micromechanical finite element analysis of textile composites. *Acta Aero. et Astro. Sini.* 34 (7), 1636 - 1645.
- [6] Li, Q., Yang, X. X., 2013. Numerical simulation for effective elastic behavior of carbon black filler particle reinforced rubber matrix composites based on periodic boundary conditions. *J. Fuzhou Uni.(Nat. Sci. Edi.)* 41, 97 - 103.
- [7] Jacques, S., Baere, I. D., Paepegem, W. V., 2014. Application of periodic boundary conditions on multiple part finite element meshes for the meso-scale homogenization of textile fabric composites. *Compos. Sci. Tech.* 92, 41 - 54.
- [8] Huang, H. T., Chang, S. L., Chien, C. S., Li, Z. C., 2009. Superconvergence of high order FEMs for eigenvalue problems with periodic boundary conditions. *Comput. Method. Appl. M.* 198(30), 2246-2259.
- [9] Sorohan, S., Sandu, M., Constantinescu, D. M., Sandu, A. G., 2015. On the evaluation of mechanical properties of honeycombs by using finite element analyses. *INCAS Bulletin.* 7(3), 135-150.
- [10] Coppoli, E. H. R., Mesquita, R. C., Silva, R. C., 2009. Periodic boundary conditions in element free Galerkin method. *COMPEL-Int. J. Comput. Math. Elect. Electron. Eng.* 28(4), 922-934.
- [11] Coppoli, E. H. R., Mesquita, R. C., Silva, R. C., 2012. Induction machines modeling with meshless methods. *IEEE Trans. Magn.* 48(2), 847-850.
- [12] Goncalves, B., Afonso, M., Coppoli, E., Schroeder, M. A., Alipio, R., Ramdane, B., Marechal, Y., 2016. Periodic Boundary Conditions in Natural Element Method.

- IEEE. T. Magnet. 52(3), 7207604.
- [13] Abaqus Analysis User's Manual (6.9),
<http://abaqusdoc.ucalgary.ca/v6.9/books/usb/default.htm>
- [14] Li, S. G., 2008. Boundary conditions for unit cells from periodic microstructures and their implications. *Compos. Sci. Technol.* 68(9), 1962-1974.
- [15] De Leo, R., 2006. Topology of plane sections of periodic polyhedra with an application to the Truncated Octahedron. *Exp. Math.* 15(1), 109-124.
- [16] Chantarapanich, N., Puttawibul, P., Sucharitpwatskul, S., Jeamwatthanachai, P., Inglam, S., Sitthiseripratip, K., 2012. Scaffold library for tissue engineering: A geometric evaluation. *Comput. Math. Meth. Med.* 14 pages.
- [17] Yang, W. L., Peng, K., Zhou, L. P., Zhu, J. J., Li, D. Y., 2014. Finite element simulation and experimental investigation on thermal conductivity of diamond/aluminium composites with imperfect interface. *Comput. Mater. Sci.* 83, 375 - 380.
- [18] Watanabe, I., Nakamura, G., Yuge, K., Setoyama, D., Iwata, N., 2015. Maximization of strengthening effect of microscopic morphology in duplex steels. In: *From Creep Damage Mechanics to Homogenization Methods*. Vol. 64. Springer, pp. 541 - 555.
- [19] Gantapara, A. P., de Graaf, J., van Rooij, R., Dijkstra, M., 2015. Phase behavior of a family of truncated hard cubes. *J. Chem. Phys.* 142(5), 054904.
- [20] ANSYS ICEM CFD Tutorial Manual,
<http://148.204.81.206/Ansys/150/ANSYS%20ICEM%20CFD%20Tutorial%20Manual.pdf>.
- [21] Qu, S., Huang, C., Gao, Y., Yang, G., Wu, S., Zang, Q., Zhang, Z., 2008. Tensile and compressive properties of AISI 304L stainless steel subjected to equal channel angular pressing. *Mater. Sci. Eng.: A* 475 (1C2), 207 - 216, international Symposium on Inorganic Interfacial Engineering 2006.

- [22] Hall, E. O., 1951. The deformation and ageing of mild steel: III discussion of results. Proc. Phys. Soc. Sec. B 64 (9), 747 - 753.
- [23] Petch, N., 1953. The cleavage strength of polycrystals. J. Iron Steel Inst. 174 (1), 25 - 28.

Chapter 4: Modeling of random structure and simulation results comparison with harmonic structure

4.1 Random structure's FEM model for comparative simulation

4.1.1 Block dividing of random structure model for meshing

For traditional composite material field, in order to toughen homogeneous material, a common method is introducing high strength particles in the high elongation matrix. It is known that rigid nanofillers can improve the fracture toughness, stiffness, and even strength of the material. Common structure of the composite is bi-model random structure. Moreover, the bi-model structure is widely acknowledged that the UFG phase supports the strength while the CG phase supports the elongation. However, the discussions for structure and arrangement are always ignored in the previous researches [1-18]. In this research, the objective experiment results of HS and random structure show that, the structure and arrangement have affected the macro deformation properties. In order to find out the mechanism which brings the different mechanical deformation properties between harmonic structure and general random structure, the FEM model for random structure has been raised. In some researches, Voronoi tessellation is often employed to describe the random structure [19-27]. In mathematics, a Voronoi diagram is a partitioning of a plane into regions based on distance to points in a specific subset of the plane. That set of points (called seeds, sites, or generators) is specified beforehand, and for each seed there is a corresponding region consisting of all points closer to that seed than to any other. These regions are called Voronoi cells. The Voronoi diagram of a set of points is dual to its Delaunay triangulation [28]. As Figure 4.1 shown, I drew a 2D Voronoi picture

by Rhinoceros [29]. I drew a 3D Voronoi sketch map by soft of Rhinoceros as Figure 4.2 shown.

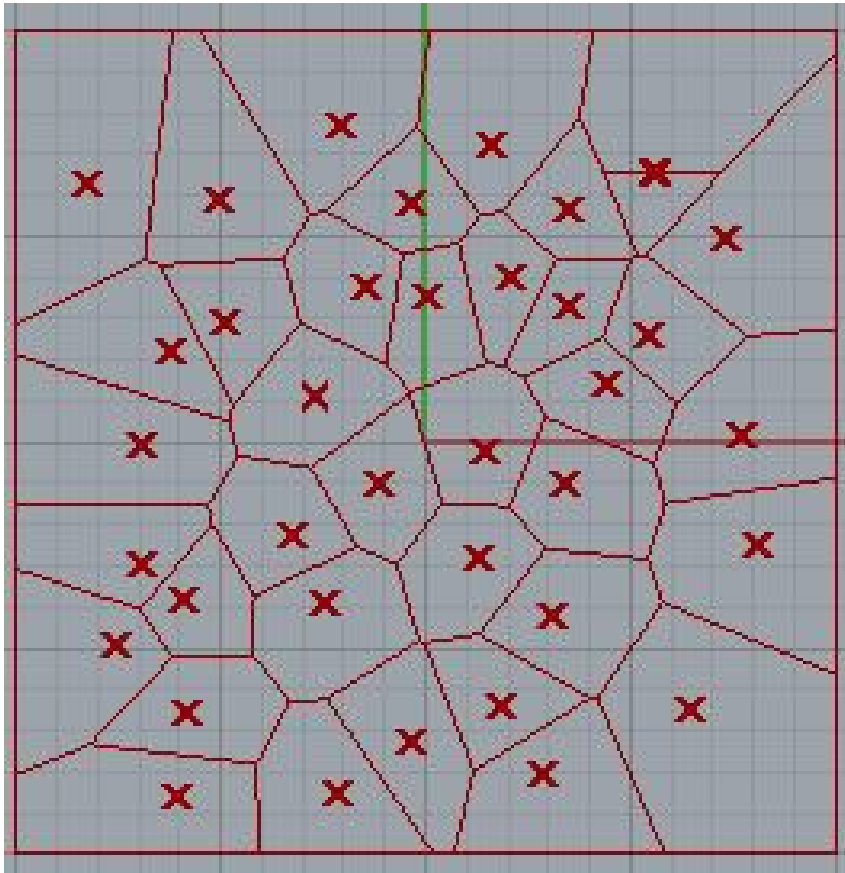


Figure 4.1: 2D Voronoi picture drawn by software of Rhinoceros.

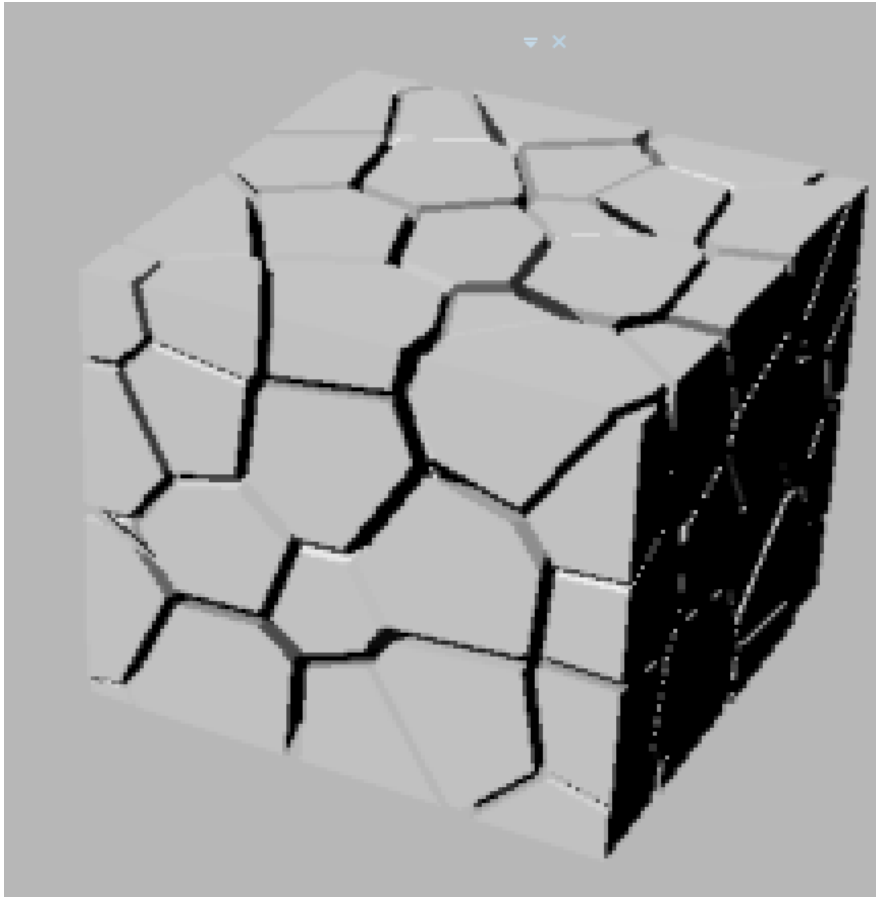


Figure 4.2: 3D Voronoi model drawn by software of Rhinoceros.

Nevertheless, for the Voronoi model, the volume fraction of UFG can not be determined, precisely. Because every cell of the Voronoi model has different volume, we can not use the percentage of the grains' numbers to describe the volume fraction of UFG. Moreover, the periodic boundary condition can not be applied in the Voronoi model according to the definition of the periodic boundary condition described in Chapter 3, which the nodes on the opposite sides should be one-one correspondence. For the Voronoi model, after thrice mirroring, the model will meet the requirement that the nodes on the opposite sides one-one correspondence. However, the plane of symmetry will be particularly conspicuous because it is the only regular part in the irregular model. Hence, the same volume cell model should be built to solve this problem.

In order to compare with harmonic structure, the base shape of random structure

should also be truncated octahedron. Random structure model can be regarded as space-filling truncated octahedron without shell region.

4.1.2 Random materials setting

The RVE should also be applied to the comparative simulation of a random structure. As shown in Figure 4.3 (1), the space-filling truncated octahedron can also be employed for the random-structure model. One quarter of the truncated octahedron is split into 12 parts, which have the same shape and volume. By mirroring and arraying the unit model, the entire RVE, which has 54 truncated octahedrons, is obtained. The entire model contains 2,592 individual parts. The contrasting feature of the random structure is the unordered arrangement of the CG and UFG structures. By defining the different parts with different material characteristics randomly, a random distribution structure can be modeled.

The mainly block dividing procedure for random structure is shown in Figure 4.3. The main point of random structure block dividing is to produce little units with same shape and volume as Figure 4.4 shown. First step is to build a 1/8 truncated octahedron as same as harmonic structure. However, there is difference between harmonic structure model and random structure model. For random structure, 1/8 truncated octahedron should has several same individual triangular prism parts but harmonic structure doesn't have. Harmonic structure model mesh can pay more attention to the direction compatibility between tensile test direction and mesh direction. While in random structure, the direction compatibility is secondary. The most significant factor of random structure block dividing is guaranteeing the oneness of parts. Hence, 6 same triangular prisms are built. After Y-grid dividing for these 6 triangular prisms, every triangular prism is divided into 3 little hexahedron blocks.

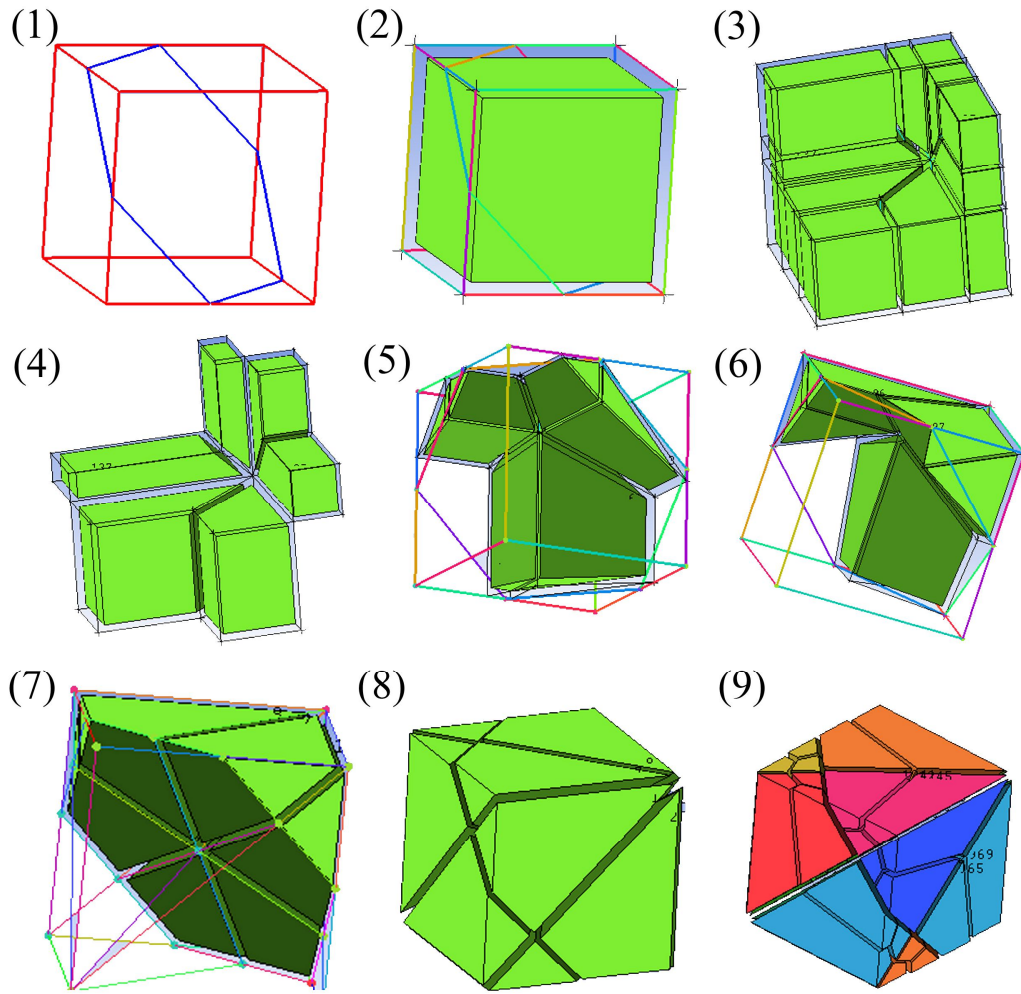


Figure 4.3: The mainly block dividing procedure for random structure.

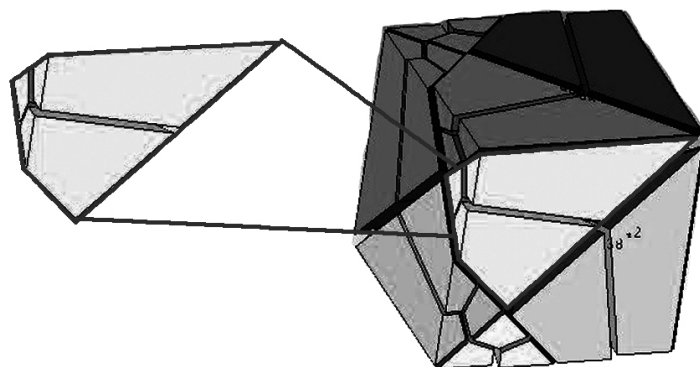


Figure 4.4: General random model block dividing based on truncated octahedron.

However, in meshing software ANSYS-ICEM, if we directly mirror and array the unit model, there will be not 2,592 individual parts in the model. There will only be just 12 individual parts, because the meshes which are mirrored or arrayed will have the same characteristics with the origin meshes. In order to obtain the individual parts, the ABAQUS mesh file ‘.inp’ should be modified directly.

ABAQUS mesh file is composed by nodes’ coordinates and elements messages. We must make the programs to deal with the mirroring and arraying of the meshes. Figure 4.5 shows the inp file of ABAQUS. The basic part for the mesh message is about the nodes and the elements and groups of elements prepared for material definition. “Node” means the node’s number and coordinates of x/y/z. “Element” means the element’s number and the nodes which constitute the mesh. “Elset” sets the element groups. “Solid Section” connects the element group with the material. Hence, for the mirroring and arraying, these four key points should be added new items, while the remaining commands of the inp file keep intact.

```

** *****
**Heading
** Job name: Job-1 Model name: a
** Generated by: Abaqus/CAE 6.12-1
**Preprint, echo=NO, model=NO, history=NO, contact=NO
**
** PARTS
**
**Part, name=PART-1
*Node
1, 0.133870006, 0., -0.00708445767
2, 0.133870006, 0., 0.
3, 0.133870006, -0.00654025283, -0.00654131593
4, 0.133870006, -0.00708330609, 0.
.....
9062, 0., -0.152286664, -0.218869999
*Element, type=C3D8
1, 1, 2, 4, 3, 5, 6, 8, 7
2, 5, 6, 8, 7, 9, 10, 12, 11
3, 9, 10, 12, 11, 13, 14, 16, 15
.....
8727, 5786, 9018, 5808, 5785, 5790, 9020, 5811, 5789
*Elset, elset=THOSEBLOCKS/CORE1_ELSET
1, 2, 3, 4, 5, 6, 7, 8, 9, 10, 11, 12, 13, 14,
15, 16
17, 18, 19, 20, 21, 22, 23, 24, 25, 26, 27, 28, 29, 30,
31, 32
33, 34, 35, 36, 37, 38, 39, 40, 41, 42, 43, 44, 45, 46,
47, 48
.....
** Section: Section-1-THOSEBLOCKS/CORE1_ELSET
**Solid Section, elset=THOSEBLOCKS/CORE1_ELSET, material=MAT1
** Section: Section-2-THOSEBLOCKS/SHELL1_ELSET
**Solid Section, elset=THOSEBLOCKS/SHELL1_ELSET, material=MAT2
** Section: Section-3-THOSEBLOCKS/CORE2_ELSET
**Solid Section, elset=THOSEBLOCKS/CORE2_ELSET, material=MAT1

```

Figure 4.5: Inp file for ABAQUS.

In this research, I choose VB to make these two programs. For arraying (Figure 4.6), the main step is to calculate the length of the model. The coordinates of new nodes should be the origin coordinates of origin nodes plus length of the model. The

new elements constituted by new nodes should be added in the file. For y direction, the modified node numbers and element numbers made by x direction arraying are the basement data. For z direction, the modified node numbers and element numbers made by x/y direction arraying are included in the basement data. The new element groups just use the original material. Modifying “Solid Section”, the material can be defined. Making an arraying program is relatively easier compared to mirroring.

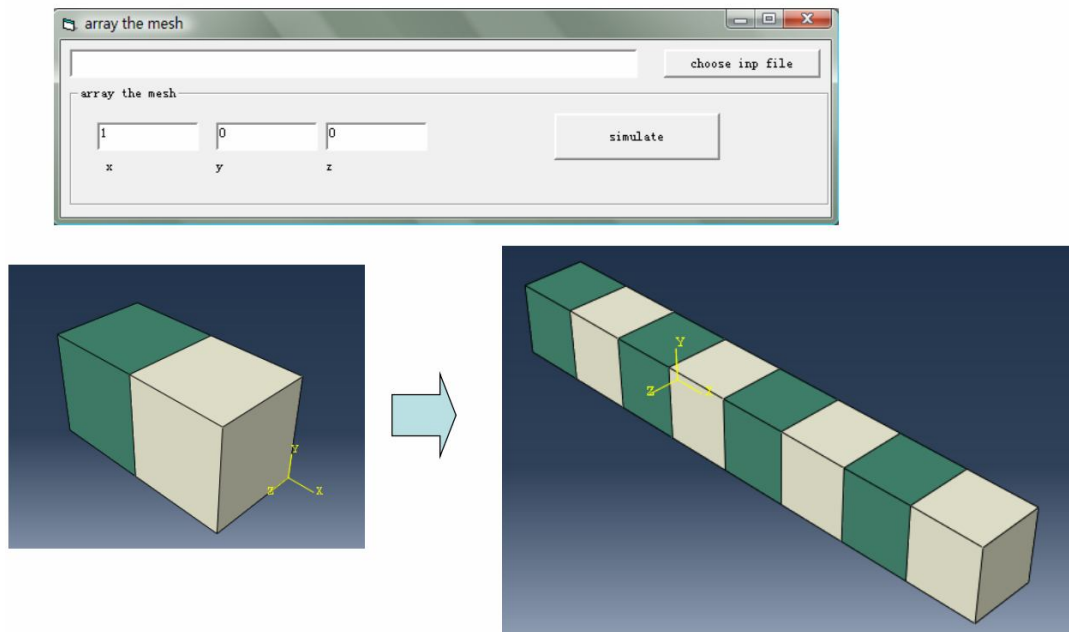


Figure 4.6: Array the mesh.

For mirroring, the orders of the nodes and the elements should be paid attention to. After programming, I found the mirrored meshes disappeared in the ABAQUS, however they are displayed in ICEM. The reason is that the mirrored meshes become minus meshes, because the orders of the nodes are clockwise according to using the nodes number directly. For one hexahedron mesh, there are eight nodes. The clockwise can be changed into inverse hour by exchanging the second node with the fourth node, the sixth node with the eighth node. This time, the mirrored meshes are displayed in ABAQUS (Figure 4.8). Even the model is prepared for random structure, the order for setting the material blocks should be paid attention to, which helps to identify the location of the blocks. After mirroring and arraying the meshes, there are duplicated nodes. The duplicated nodes can be merged in ABAQUS.

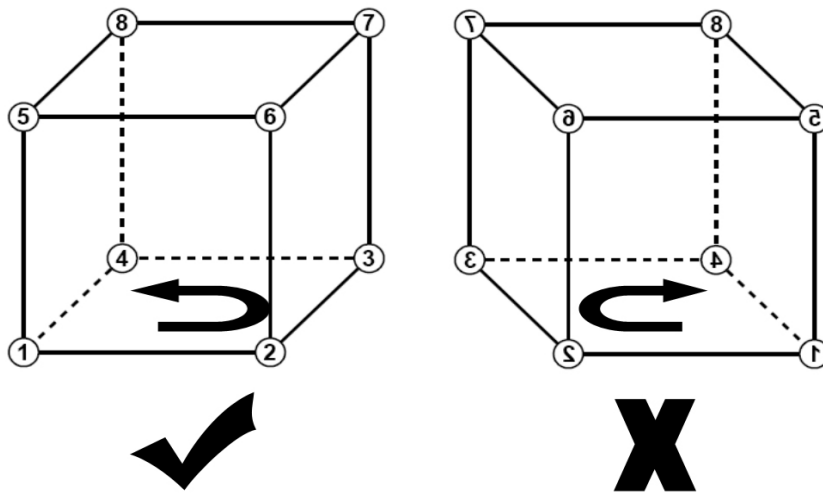


Figure 4.7: Inverse hour order of nodes for mesh.

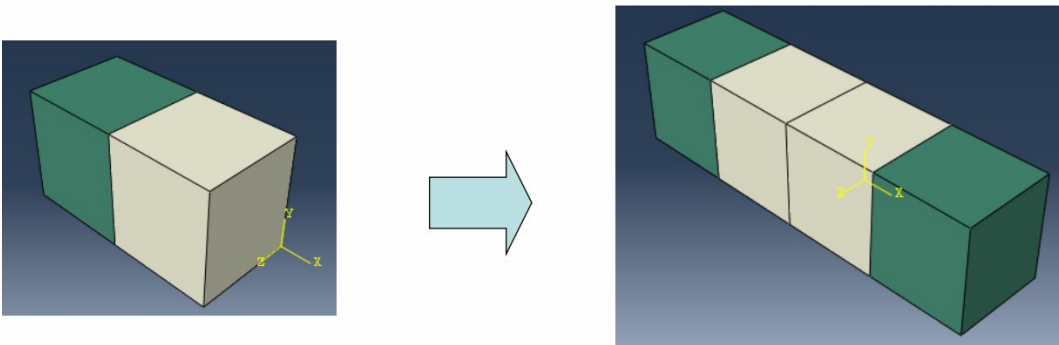
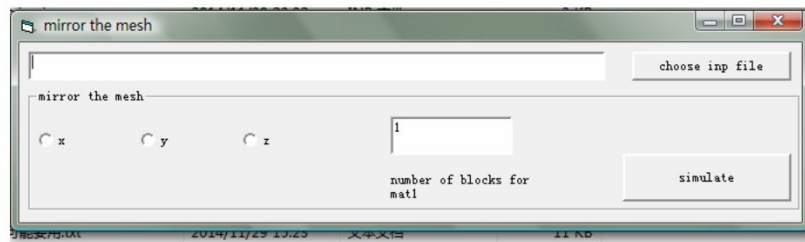


Figure 4.8: Mirror the mesh.

By controlling the percentage of the parts that constitute the UFG material of the random-structure model, the UFG volume fraction of the random-structure model is made equal to the UFG volume fraction of the harmonic-structure model shown in Figure 4.9. Thus, the structural effect can be distinguished. In this research, the UFG

volume fraction of the harmonic-structure model is 20.7%. The number of individual parts in the entire random-structure model is 2,592; therefore, 20.7% of 2,592 equals 537. Thus, 537 individual parts should be stochastically defined as the UFG material and the remaining 2,055 individual parts should be defined as the CG material. As shown in Figure 4.9, by defining the material of the units, an RVE of the random-structure model can be built. The light gray parts are the CG regions, whereas the dark gray parts represent the UFG regions.

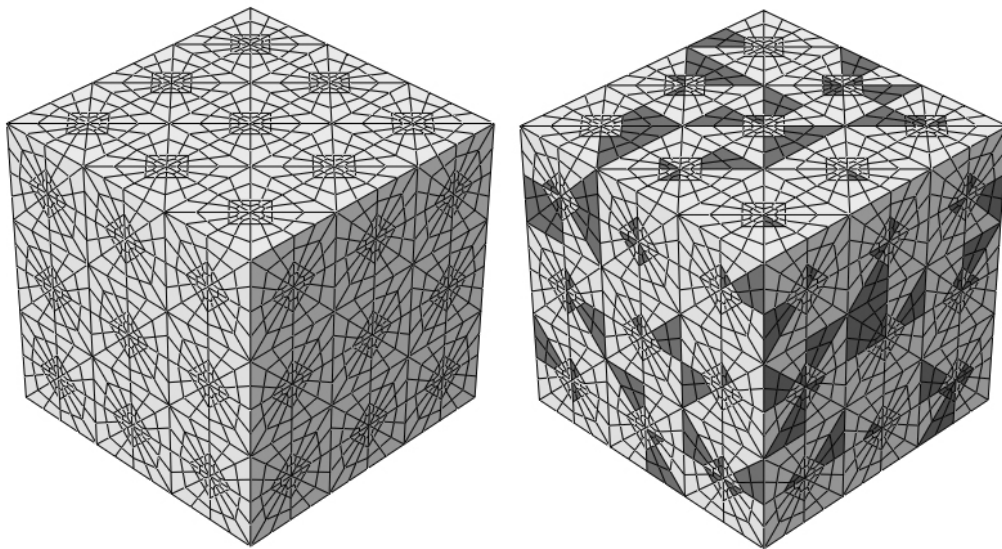


Figure 4.9: Constructing the SUS304L general random structure mesh, IP+MM360ks
(weight ration=1:1) compact.

4.2 Simulation results comparison between harmonic structure and random structure

4.2.1 True stress-strain curves

Figure 4.10 shows the true stress-strain curve of the SUS304L material. The dashed line and dotted line correspond to the estimated curve of SUS304L harmonic and random structure materials, respectively, while the solid line shows the experimental data of SUS304L harmonic structure material. By comparing the true stress-strain curve of the estimated results of multi-scale FEA to the experimental

result, the superposition of the shape of these curves can be obtained, ensuring the validity of the multi-scale FEA model.

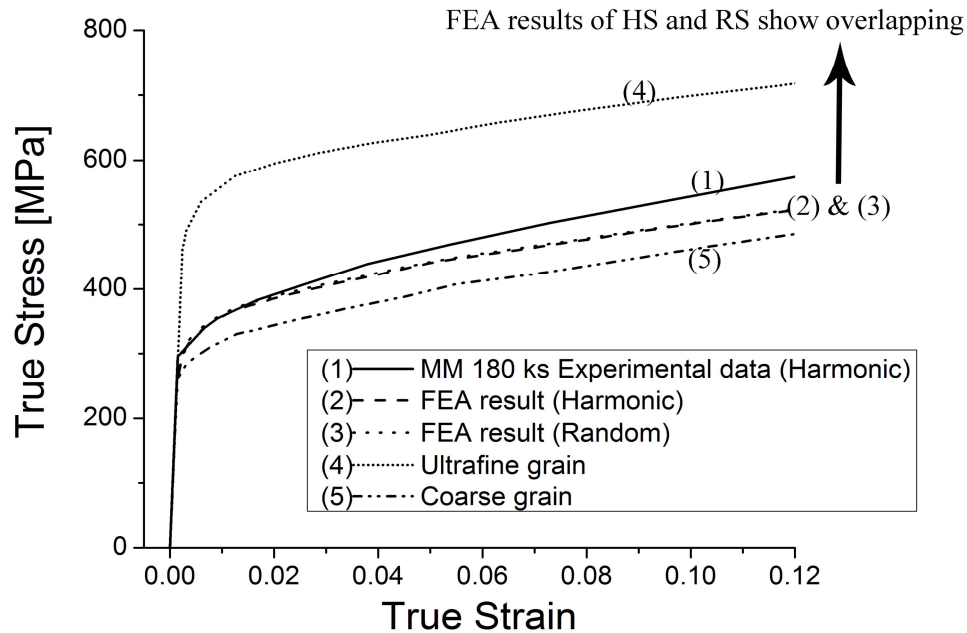


Figure 4.10: Simulation and experiment's true s-s curves comparison of SUS304L material.

4.2.2 Stress & strain contour distribution

Figure 4.11(a) shows the Von Mises Stress distribution of the harmonic structure model and the general random structure model. The results demonstrate that the highest Mises stress value of the harmonic structure model is 740MPa, while the highest Mises stress value of the general random structure model is 760MPa. The common point of these two figures is the main degree of Von Mises Stress distributed on the UFG (ultra fine grain) parts. However, the results indicate that the general random structure still shows lots of stress location parts, while the stress distribution of the harmonic structure model demonstrates uniformity comparatively.

Figure 4.11(b) shows the max. principal plastic strain distribution of the harmonic structure model and the general random structure model. For the strain distribution, max. principal plastic strain and plastic equivalent strain can both be employed to

describe the strain distribution. However, as this research is about the Uniaxial Tensile Test problem, because the tensile direction is single axle, both max. principal plastic strain and plastic equivalent strain are applicable. Moreover, I have used these two ways to observe the strain distribution maps, and there is hardly any difference between these two methods' results. The value label is the auto label of the harmonic structure result. The light grey part of the label is in order to express the highest value of the random structure result. The highest strain value of the harmonic structure model is 0.146, while the highest strain value of the general random model is 0.22. It demonstrates there are still some strain localizations happening in the random structure. For the general random structure model, while expressing strain hardening through the process of deforming, it will show higher distortion resistance earlier than the harmonic structure model. Hence, the general random structure model will witness show plastic instability phenomenon earlier, consequently expressing cracks earlier. Moreover, from the strain distribution, UFG phase and CG phase in harmonic structure can be distinguished very clearly. Comparatively speaking, for harmonic structure strain distribution, high value regions represent CG phase, low value regions represent UFG phase, respectively. However, for random structure strain distribution, it is difficult to distinguish UFG phase and CG phase from contour distribution. Some CG regions demonstrate strain localization, while some UFG region also show strain localization. It indicates that, in random structure, CG phase will not assist UFG phase supporting strain, while in harmonic structure, CG phase undertakes some strain which UFG phase ought to take. CG phase protects the fragile UFG phase.

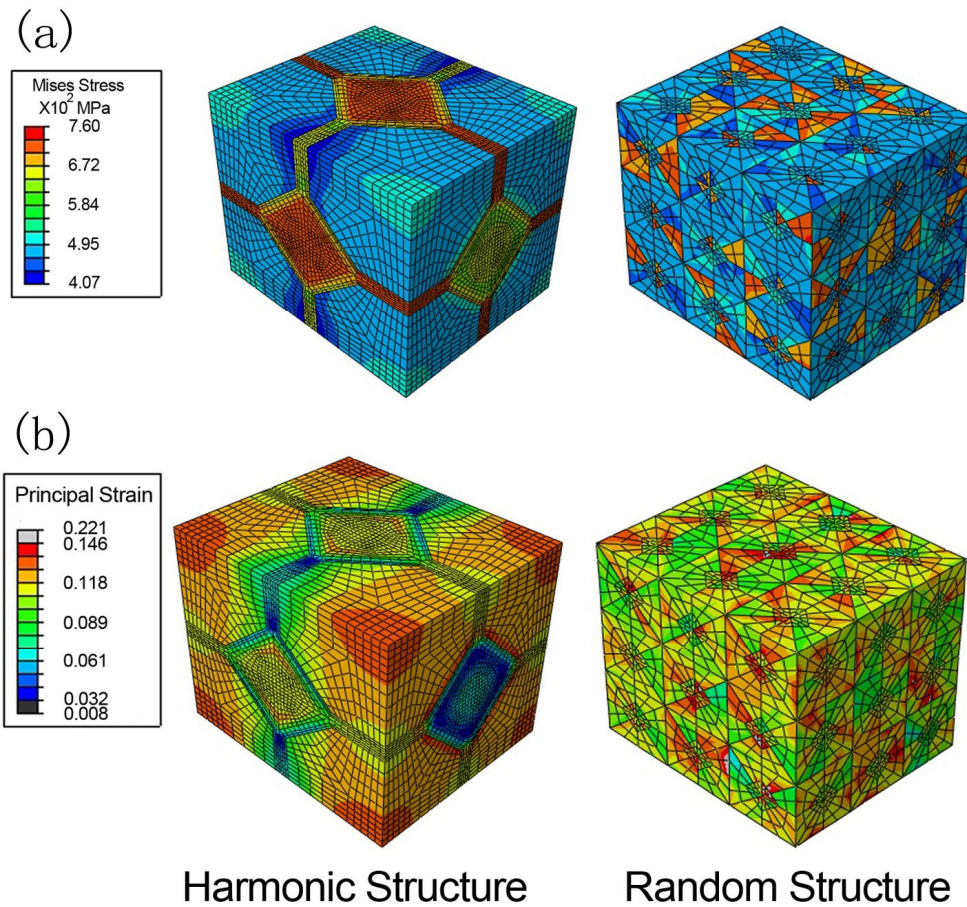


Figure 4.11: (a) Von Mises Stress and (b) max. principal plastic strain distribution of harmonic and random structures.

4.2.3 Histograms of the stress and strain distribution frequency

In order to confirm the disparity of the stress and strain distribution for these two types of structure models, the histograms of the stress and strain distribution have been applied. The data in Gauss quadrature integral points and the meshes' volume were utilized. For the strain and stress distributions, the horizontal axis represents the strain or Mises Stress [MPa], while the vertical axis represents volume fraction in the whole model within the scope of stress and strain. In ABAQUS, the valid point for calculation is Gauss quadrature integral point which is inside of mesh but not the node

of the mesh. In order to avoid the cognitive errors of material duplication definition of the node in the boundary of the two different material characteristics meshes, the Gauss quadrature integral point inside the mesh has been employed. Moreover, as the parameter called averaging threshold in ABAQUS changed, the contour distribution will be changed, because the parameter decides the contour continuity of the adjacent meshes. However, the result of Gauss quadrature integral point is exact value which is used in calculation, while the results of the node and the remaining parts of the mesh are derivation values. Hence, in the histograms, the data of Gauss quadrature integral points are employed. In this research, because the hexahedral mesh has been applied, there are 8 Gauss quadrature integral points in one mesh in order to match along with 8 nodes. Because every mesh's volume is different from other meshes', for the accuracy of the histogram result, the mesh's volume should be added into the calculation instead of merely calculating for mesh numbers. Hence, the occupancy of one mesh in whole model can be calculated, while occupancy of one Gauss quadrature integral point accounts for $1/8$ of this mesh's occupancy. Hence, file for data in Gauss quadrature integral points and file for meshes' volume should be dealt with together. For harmonic structure, even for the whole model, there are just three parts in whole model, two for cores, and one for shell. Therefore, the needless parts which are the introductions for the data can be deleted by hand. While for random structure, there are 2592 individual parts and not only one working condition is simulated, thus, extracting the data by hand is unrealistic. In this research, I made programs to extract and calculate the data. Hence, the frequency of the stress/strain distribution can be observed, intuitively.

For the data expression, on a linear scale, the lower value is always ignored compared to the higher value; therefore, in this research, instead of a simple linear scale, a probability scale is used to describe the vertical axis of the volume fraction. The probability scale represents the inverse of a cumulative Gaussian distribution. Plotting a cumulative Gaussian distribution produces a sigmoid-shaped curve which comes from the function called `norminv`. This curve, when displayed on a probability scale, appears as a straight line. Because probabilities are expressed as percentages,

all values must fall between 0 and 100. The probability scale range is from 0.0001 to 99.999. The probability scale specializes in displaying the frequency problem exactly as required in this research. In contrast to the linear scale, the probability scale emphasizes the lower value while also showing the higher value well.

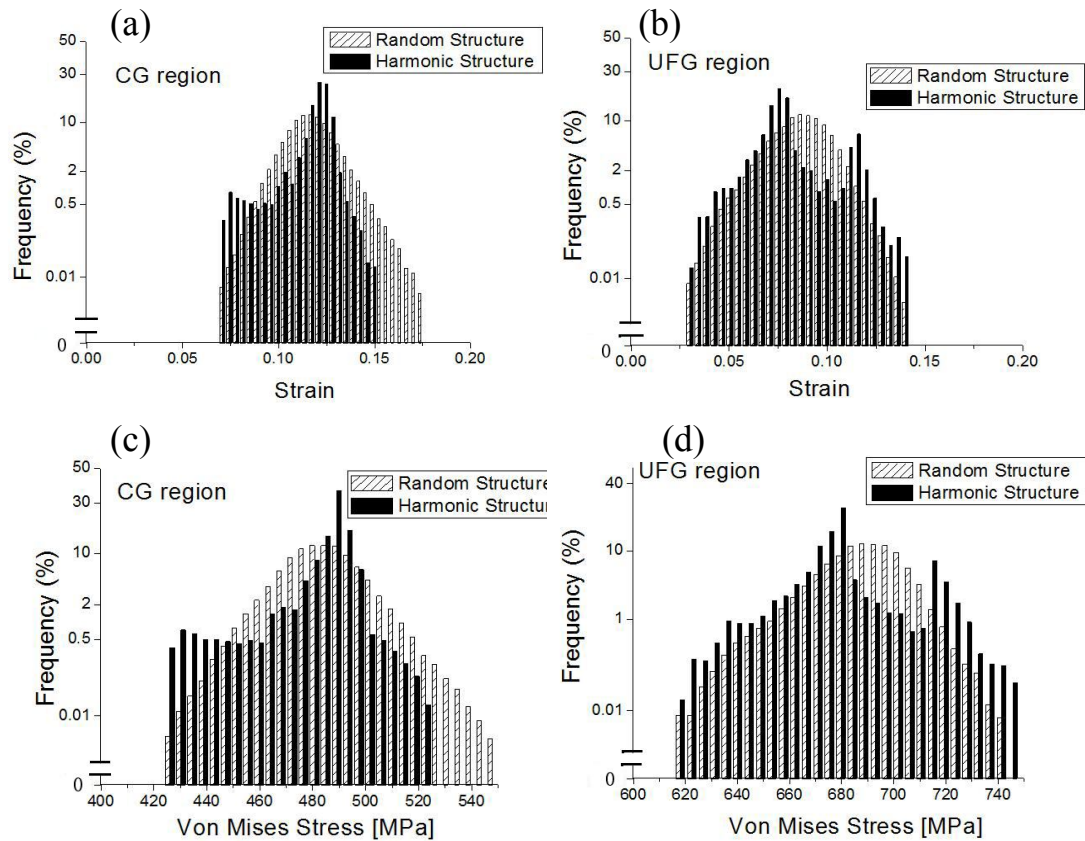


Figure 4.12: Strain frequency histogram: (a) CG; (b) UFG;

Stress frequency histogram: (c) CG; (d) UFG.

From the strain histogram figure of CG, UFG (Figure 4.12 a,b), it can be observed that: The harmonic structure results distribute intensively, with the highest value at 0.148, while the general random structure results distribute dispersedly, with the highest value at 0.176. It demonstrates that in random structure, without the connection of the UFG phase, the CG phase deforms willfully. The highest value strain domains in random structure would be the weak parts as the deforming continuing. Furthermore, the strain distributes wider range in random structure than the harmonic structure. It signified the narrow CG phase strain distributes more

uniform deformation in harmonic structure. Owing to the connection of UFG phase in harmonic structure, the non-uniform structure can lead to uniform deforming. However, in the histogram figure for CG, it can be seen that the peak of the general random model is 0.117, while the peak of the harmonic structure model is 0.124. Compared with the general random model, the peak of the harmonic structure model moved to the higher value in CG area. The result demonstrates that in the harmonic structure model the course grain phase undertakes the major strain. While in the general random model, the course grain phase doesn't show the elongation function enough. Moreover, in the histogram figure of UFG, it can be shown that the peak of the general random model happens close to 0.09, while the peak of the harmonic structure model happens near 0.07. The results reveal that in harmonic structure material, the UFG phase suffers less strain than in general random structure material. It means that the CG phase in harmonic structure material suffers more strain and carries enormous importance of elongation improvement.

From the Von Mises Stress histogram figure of CG, UFG (Figure 4.12 c,d), it can be demonstrated that for CG phase, the harmonic structure results distribute intensively as the strain results show, with the highest value at 523MPa, as the general random structure results distribute dispersedly, with the highest value at 550MPa. The results also demonstrate that the general random structure still shows stress localization.

4.3 Conclusions

In this chapter, random structure FEM model has been raised to compare with Harmonic structure. The results show that in the random micro-structure, stress and strain localization occurred, whereas in the harmonic-structure materials, the network structure of the UFG phase prevented stress and strain localization. Especially in strain distribution of random structure, the difference between CG phase and UFG phase is hardly shown at all. It indicates that, for random structure, UFG phase should undertake the strain as the CG phase takes. In contrast, in harmonic structure, CG

phase assists to undertake some strain which UFG phase ought to support, which prevents the strain localization happening in the UFG phase. Hence, compared to the random micro-structure, the harmonic-structure materials exhibit better mechanical performance. Owing to the connection of the UFG phase in the harmonic structure, a non-uniform structure is formed, leading to uniform deformation.

References

- [1] Zhao, M. C., Yin, F. X., Hanamura, T., Nagai, K., Atrens, A., 2007. Relationship between yield strength and grain size for a bimodal structural ultrafine-grained ferrite/cementite steel. *Scripta Mater.* 57 (9), 857 - 860.
- [2] Sano, T., Rohrer, G. S., 2007. Experimental evidence for the development of bimodal grain size distributions by the nucleation-limited coarsening mechanism. *J. Am. Cera. Soc.* 90 (1), 211 - 216.
- [3] Chakrabarti, D., Davis, C., Strangwood, M., 2007. Characterisation of bimodal grain structures in HSLA steels. *Mater. Charact.* 58(5), 423 - 438.
- [4] Tejedor, R., Rodriguez-Baracaldo, R., Benito, J., Cabrera, J., Prado, J., 2008. Plastic deformation of a nanostructured and ultrafine grained Fe-1%Cr with a bimodal grain size distribution. *Int. J. Mater. Forming* 1 (1), 487 - 490.
- [5] Wang, T. S., Zhang, F. C., Zhang, M., Lv, B., 2008. A novel process to obtain ultrafine-grained low carbon steel with bimodal grain size distribution for potentially improving ductility. *Mater. Sci. Eng.: A* 485 (1), 456 - 460.
- [6] Afshar, A., Simchi, A., 2009. Flow stress dependence on the grain size in alumina dispersion-strengthened copper with a bimodal grain size distribution. *Mater. Sci. Eng.: A* 518 (1), 41 - 46.
- [7] Prasad, M., Suwas, S., Chokshi, A., 2009. Microstructural evolution and mechanical characteristics in nanocrystalline nickel with a bimodal grain-size distribution. *Mater. Sci. Eng.: A* 503 (1), 86 - 91.
- [8] Zhao, D. P., Liu, Y., Liu, F., Wen, Y. R., Zhang, L. J., Dou, Y. H., 2011. ODS

- ferritic steel engineered with bimodal grain size for high strength and ductility. *Mater. Lett.* 65(11), 1672 - 1674.
- [9] Gollapudi, S., 2012. Grain size distribution effects on the corrosion behavior of materials. *Corros. Sci.* 62, 90 - 94.
- [10] Patra, S., Hasan, S. M., Narasaiah, N., Chakrabarti, D., 2012. Effect of bimodal distribution in ferrite grain sizes on the tensile properties of low-carbon steels. *Mater. Sci. Eng.: A* 538, 145 - 155.
- [11] Raju, K. S., Sarma, V. S., Kauffmann, A., Hegedus, Z., Gubicza, J., Peter-lechner, M., Freudenberger, J., Wilde, G., 2013. High strength and ductile ultrafine-grained Cu-Ag alloy through bimodal grain size, dislocation density and solute distribution. *Acta Mater.* 61 (1), 228 - 238.
- [12] Casas, C., Tejedor, R., Rodriguez-Baracaldo, R., Benito, J., Cabrera, J., 2015. The effect of oxide particles on the strength and ductility of bulk iron with a bimodal grain size distribution. *Mater. Sci. Eng.: A* 627, 205 - 216.
- [13] Hilger, I., Bergner, F., Weißgarber, T., 2015. Bimodal grain size distribution of nanostructured ferritic ODS Fe - Cr alloys. *J. Am. Ceram. Soc.* 98 (11), 3576 - 3581.
- [14] Kidder, S., Hirth, G., Avouac, J.-P., Behr, W., 2015. The influence of stress history on the grain size and microstructure of experimentally deformed quartzite. *J. Struc. Geo.* 83, 194 - 206.
- [15] Oskooie, M. S., Asgharzadeh, H., Kim, H., 2015. Microstructure, plastic deformation and strengthening mechanisms of an Al-Mg-Si alloy with a bimodal grain structure. *J. Alloy. Compd.* 632, 540 - 548.
- [16] Szabó, P. J., Field, D. P., Jóni, B., Horvák, J., Ungár, T., 2015. Bimodal Grain Size Distribution Enhances Strength and Ductility Simultaneously in a Low-Carbon Low-Alloy Steel. *Metall. Mater. Trans. A* 46 (5), 1948-1957.
- [17] Sabooni, S., Karimzadeh, F., Enayati, M. H., Ngan, A. H. W., 2015. The role of martensitic transformation on bimodal grain structure in ultrafine grained AISI 304L stainless steel. *Mater. Sci. Eng.: A* 636, 221-230.
- [18] Shen, M. J., Zhang, M. F., Ying, W. F., 2015. Processing, microstructure and

- mechanical properties of bimodal size SiC_p reinforced AZ31B magnesium matrix composites. *J. Magn. Alloy.* 3 (2), 162 - 167.
- [19] Nygard, M., Gudmundson, P. (2002). Three-dimensional periodic Voronoi grain models and micromechanical FE-simulations of a two-phase steel. *Comput. Mater. Sci.* 24(4), 513-519.
- [20] Wang, Y. L., Liang, S. H., Xiao, P., Zou, J. T., 2011. FEM simulations of tensile deformation and fracture analysis for CuW alloys at mesoscopic level. *Comput. Mater. Sci.* 50 (12), 3450 - 3454.
- [21] Greco, F., Gagliardi, F., Filice, L., Gonzalez, D., Alfaro, I., Cueto, E., 2011. A Voronoi - Based Nodal Integrated FEM Simulation of Extrusion Process. In the 14th International Esaform Conference of Material Forming: Esaform 2011 (Vol. 1353, No. 1, pp. 1157-1162). AIP Publishing.
- [22] Mollon, G., Zhao, J., 2012. Fourier–Voronoi-based generation of realistic samples for discrete modelling of granular materials. *Granular. Matter.* 14(5), 621-638.
- [23] Regener, B., Kremaszky, C., Werner, E., & Stockinger, M., 2012. Modelling the micromorphology of heat treated Ti6Al4V forgings by means of spatial tessellations feasible for FEM analyses of microscale residual stresses. *Comput. Mater. Sci.* 52(1), 77-81.
- [24] Luo, L., Jiang, Z., Lu, H., Wei, D., Linghu, K., Zhao, X., Wu, D., 2014. Optimisation of size-controllable centroidal voronoi tessellation for FEM simulation of micro forming processes. *Proc. Eng.* 81, 2409-2414.
- [25] Tang, L., Shi, X., Zhang, L., Liu, Z., Jiang, Z., Liu, Y., 2014. Effects of statistics of cell's size and shape irregularity on mechanical properties of 2D and 3D Voronoi foams. *Acta Mechanica.* 225(4-5), 1361-1372.
- [26] Mollon, G., 2015. A numerical framework for discrete modelling of friction and wear using Voronoi polyhedrons. *Trib. Inter.* 90, 343-355.
- [27] Wang, H., Qin, Q. H., Xiao, Y., 2016. Special n-sided Voronoi fiber/matrix elements for clustering thermal effect in natural-hemp-fiber-filled cement composites. *Inter. J. Heat. Mass. Transf.* 92, 228-235.
- [28] Voronoi diagram, wikipedia. https://en.wikipedia.org/wiki/Voronoi_diagram.

[29] Rhinoceros 3D, wikipedia. https://en.wikipedia.org/wiki/Rhinoceros_3D.

Chapter 5: Comparative simulations of 4 kinds 50% UFG volume fraction bi-modal heterogeneous models

5.1 4 kinds of 50% UFG volume fraction models based on same geometry of truncated octahedron

50% UFG volume fraction is a special balance status for bi-model which constituted by half UFG region and CG region. Via exchanging the material of shell region and cores region of harmonic structure, the inverse harmonic structure model can be built. In Chapter 4, we compared the harmonic structure with general random structure. We found that comparing with irregular random structure, harmonic structure with network structure can achieve higher mechanism capabilities. In this chapter, we choose different kinds of 50% UFG volume fraction models to compare with each other to discuss if there are other structural factors for harmonic structure deciding the mechanism characteristics.

Figure 5.1 shows 4 kinds of 50% UFG volume fraction models based on truncated octahedron. The light gray parts are the CG regions, whereas the dark gray parts represent the UFG regions. These 4 kinds of 50% UFG volume fraction models are (1) harmonic structure (HS); (2) inverse harmonic structure (inv. HS); (3) random structure; (4) 3D fabric structure. Thanks to the space-filling function of truncated octahedron, the foundation shapes of these four models are all truncated octahedron what makes the comparison feasible.

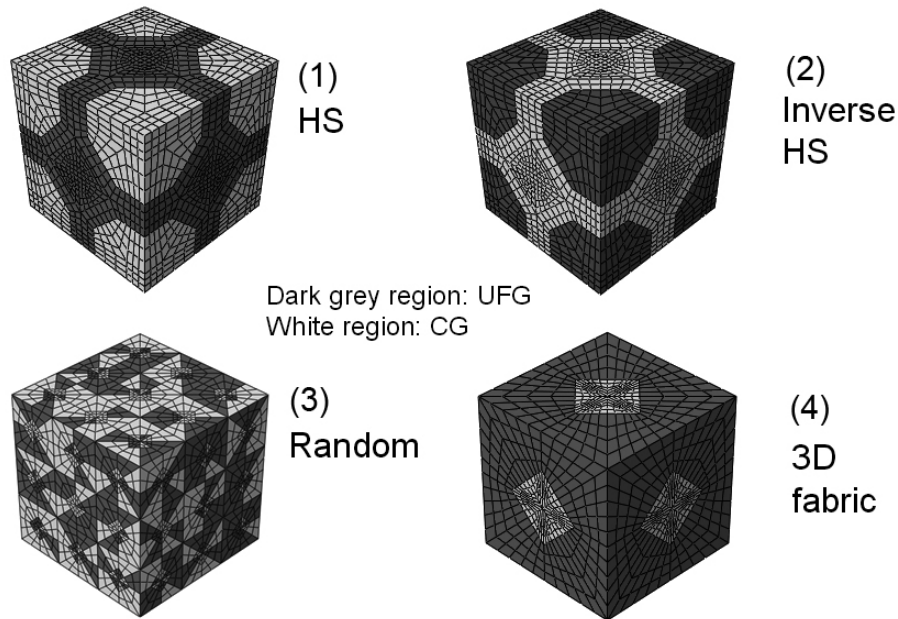


Figure 5.1: 4 kinds of 50% UFG volume fraction models based on truncated octahedron.

(1) HS; (2) inv. HS; (3) random structure; (4) 3D fabric structure.

Traditionally, in the field of composite materials, homogeneous materials are toughened by introducing high-strength particles in the matrix. It is known that rigid nanofillers can improve the fracture toughness, stiffness, and even strength of a material (Wang et al. (2013)); the inverse harmonic structure is often used to represent this improvement. The inv. HS (Figure 5.1 (2)) with a high-elongation shell and high-strength cores has been widely used for improving material strength, and its composition is opposite to that of a HS (Figure 5.1 (1)).

The Figure 5.1 (3) shows the random structure model for 50% UFG volume fraction model. Random structure model is built in Chapter 4. As there are 2,592 individual units in the random structure model, therefore, 50% of 2,592 equals 1,296. Hence, 1,296 individual parts should be stochastically defined as the UFG material and the remaining 1,296 individual parts should be defined as the CG material.

The fabric structure has been validated as the high mechanical performance [5-11]. In this research, the fabric structure model based on truncated octahedron has been used. Figure 5.1 (4) shows the 3D fabric structure model with 50% UFG volume fraction. As the periodic boundary has been employed, the CG region and UFG region

are both connected as the 3D network, respectively. Because the 3D fabric model showed in figure is based on truncated octahedron, in order to make the model structure composition clear to understand, regular cubic 3D perfect fabric model illustration based on cube (Figure 5.2) has been built to compare with 3D fabric structure from truncated octahedron. From the regular cubic 3D perfect fabric model illustration, it can be observed that the model has two same cross banding fabric structures. These two cross banding fabric constitutes constitute space filling structure with connection, collaboratively. Then the 3D fabric structure model based on truncated octahedron is constituted in the same way, while the cross banding fabric structure is not as perfect as the shape of cube.

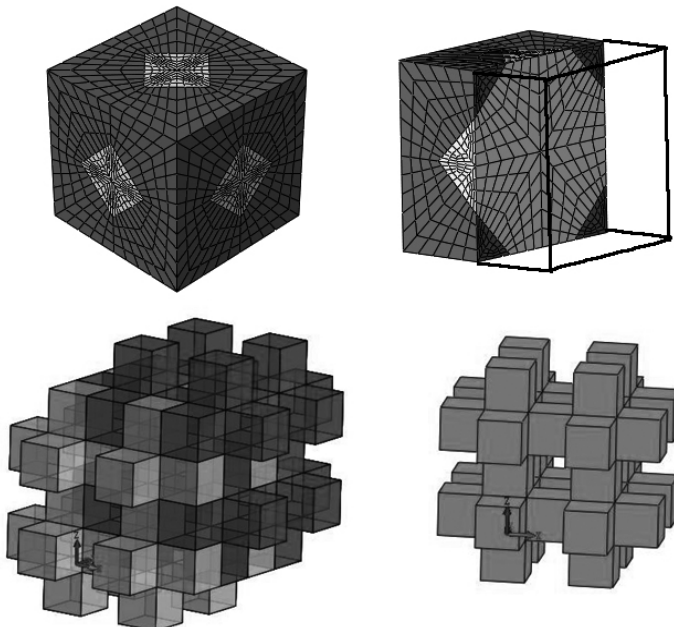


Figure 5.2: 3D fabric structure based on truncated octahedron and 3D fabric structure based on cube.

In order to understand the difference in the mechanisms of the HS, inv. HS, random structure and 3D fabric structure model. Multi-scale FEM simulations for these four models have been raised. The grain sizes of the CG and UFG materials are set as 17.6 and 2.0 μm , respectively, as same as the SUS304L harmonic structure. The strain obtained from the tensile test simulation is 12%.

5.2 Results

5.2.1 True stress-strain curves

Figure 5.3 shows the true stress-strain curves of these four models. Except the orange and purple lines which represent ultrafine grain and coarse grain, the left four curves which represent four models show almost superposition as the previous conclusion that the strength is almost equal while the volume shell fraction and grain sizes are the same, which is in keeping with the experiment results of HS and random structure, for SUS304L structure. The results demonstrate that there is no relationship between yield strength and bi-modal structures no matter the bi-modal structures have any constitution.

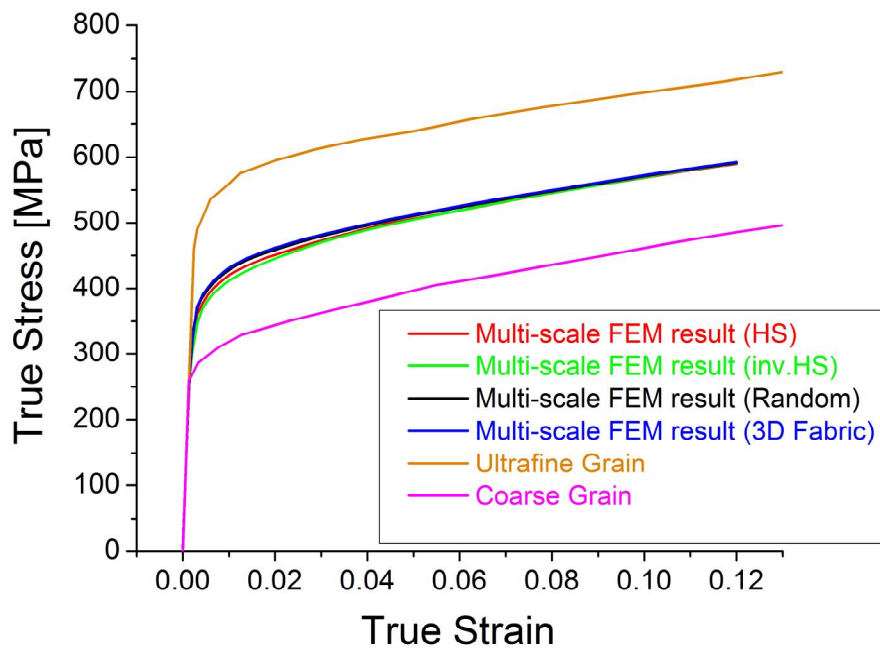


Figure 5.3: True s-s curves comparison of 4 kinds of 50% UFG volume fraction models by multi-scale FEM.

5.2.2 Stress & strain contour distribution

Figure 5.4 shows the Von Mises Stress distribution of these four models. The results demonstrate that the highest Von Mises Stress value of the harmonic structure model is 750 MPa, while the highest Von Mises Stress value of the inv. HS is 771 MPa, the general random structure model is 789 MPa and the 3D fabric structure is 793 MPa. The common point of these two figures is the main degree of Von Mises Stress distributed on the UFG (ultra fine grain) parts. However, the results indicate that the other 3 models still show lots of stress localization parts, especially the random structure and 3D fabric structure, while the stress distribution of the harmonic structure model demonstrates uniformity comparatively.

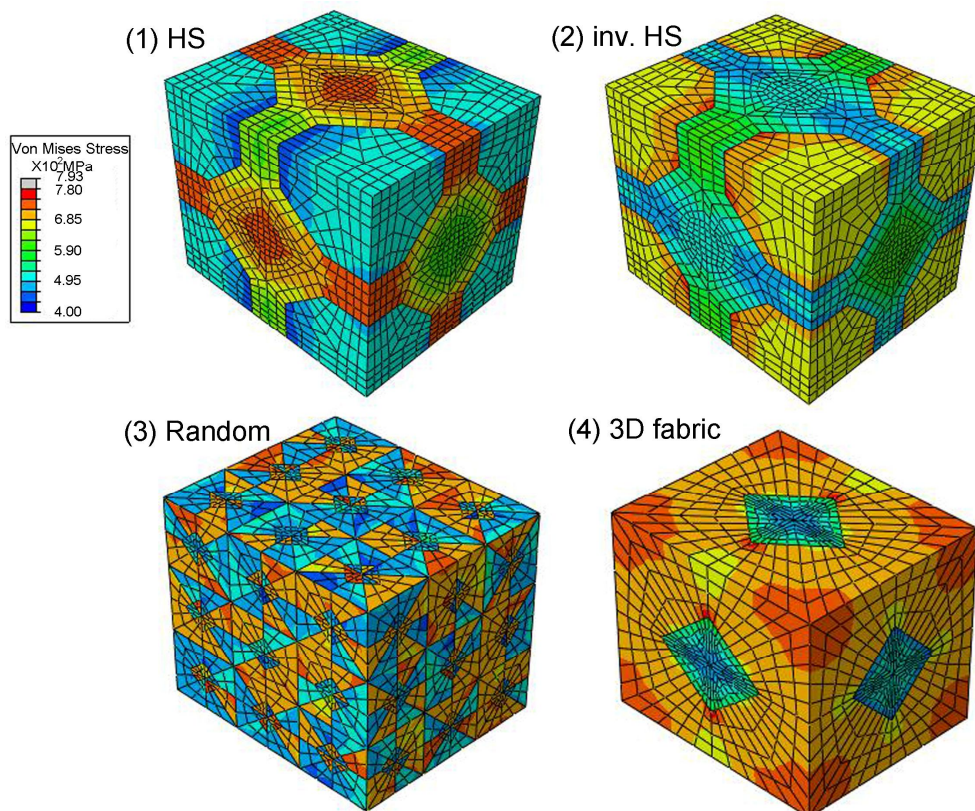


Figure 5.4: Von Mises Stress distribution of 4 models. (1) HS; (2) inv. HS; (3) random structure; (4) 3D fabric structure.

Figure 5.5 shows the max. principal plastic strain distribution for the 4 kinds of models. The values in the legend are the actual values obtained from the

harmonic-structure results. The maximum value in the light gray part (i.e., 0.249) represents the highest value obtained from the inv. HS results, whereas the maximum value in the red part (i.e., 0.155) represents the highest value obtained from the harmonic-structure results. Note that even though the maximum value (i.e., 0.155) is set as the highest value of the harmonic structure, the software ABAQUS automatically shows the region in which the value exceeds 0.155 as the light gray part. The above results indicate that some strain localization still occurs in the other 3 models except HS. When expressing strain hardening through the process of deformation, the other 3 kinds of models will show higher distortion resistance earlier than the HS model. Thus, the other 3 kinds of models will exhibit plastic instability earlier and will consequently express cracks earlier. Within the 3 kinds of models, compared to the random structure and 3D fabric structure, the inv. HS shows significant difference.

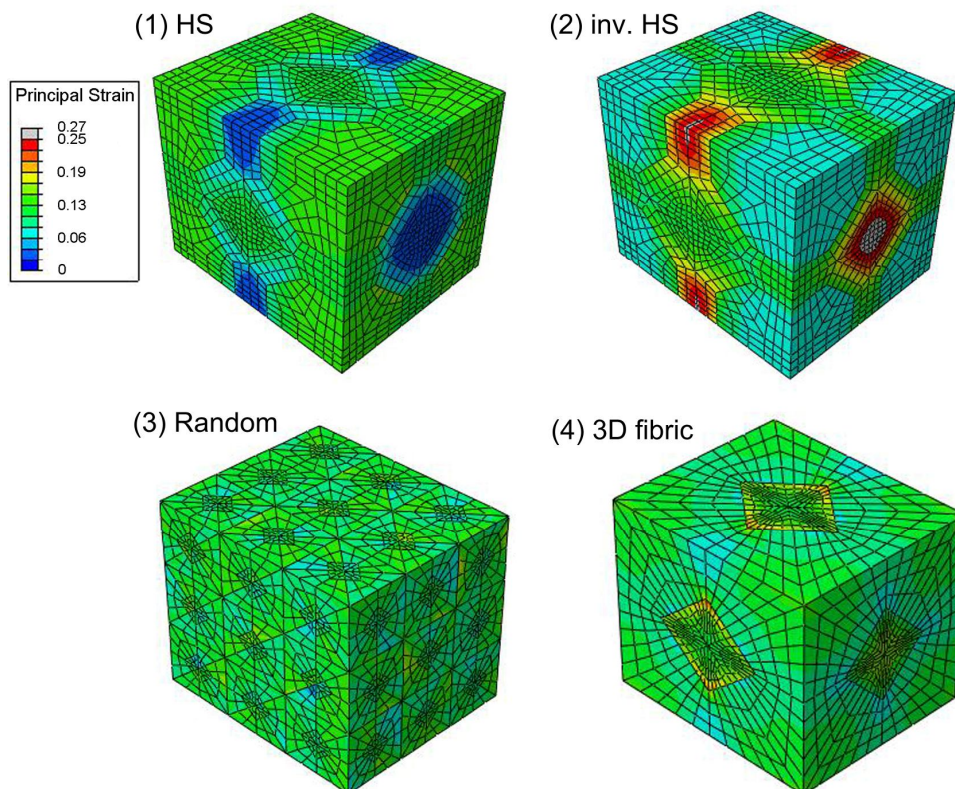


Figure 5.5: Max. principal plastic strain distribution of 4 models. (1) HS; (2) inv. HS; (3) Random structure; (4) 3D fabric Structure.

For the comparison of HS and inv. HS, as Figure 5.4 and 5.5 shown, the Von Mises Stress and max. principal plastic strain distribution of HS model and inv. HS model. The highest stress and strain value of the HS model are 750MPa and 0.155, while the highest stress value of the inv. HS model are 771MPa and 0.257. The results indicate that without the connection of the UFG phase, the inv. HS demonstrate the strain localizations obviously. Without the connection of the UFG phase, the CG phase is forced to undertake more deformation. However, the strain localization of inverse harmonic structure may lead to crack.

From Figure 5.6 to Figure 5.9, the figures demonstrate transition process of Von Mises Stress and max. principal plastic strain distribution along with the deformation for these four kinds of materials. All of the four models have the same tendency that higher stress appears in UFG regions, while mainly strain appears in CG regions.

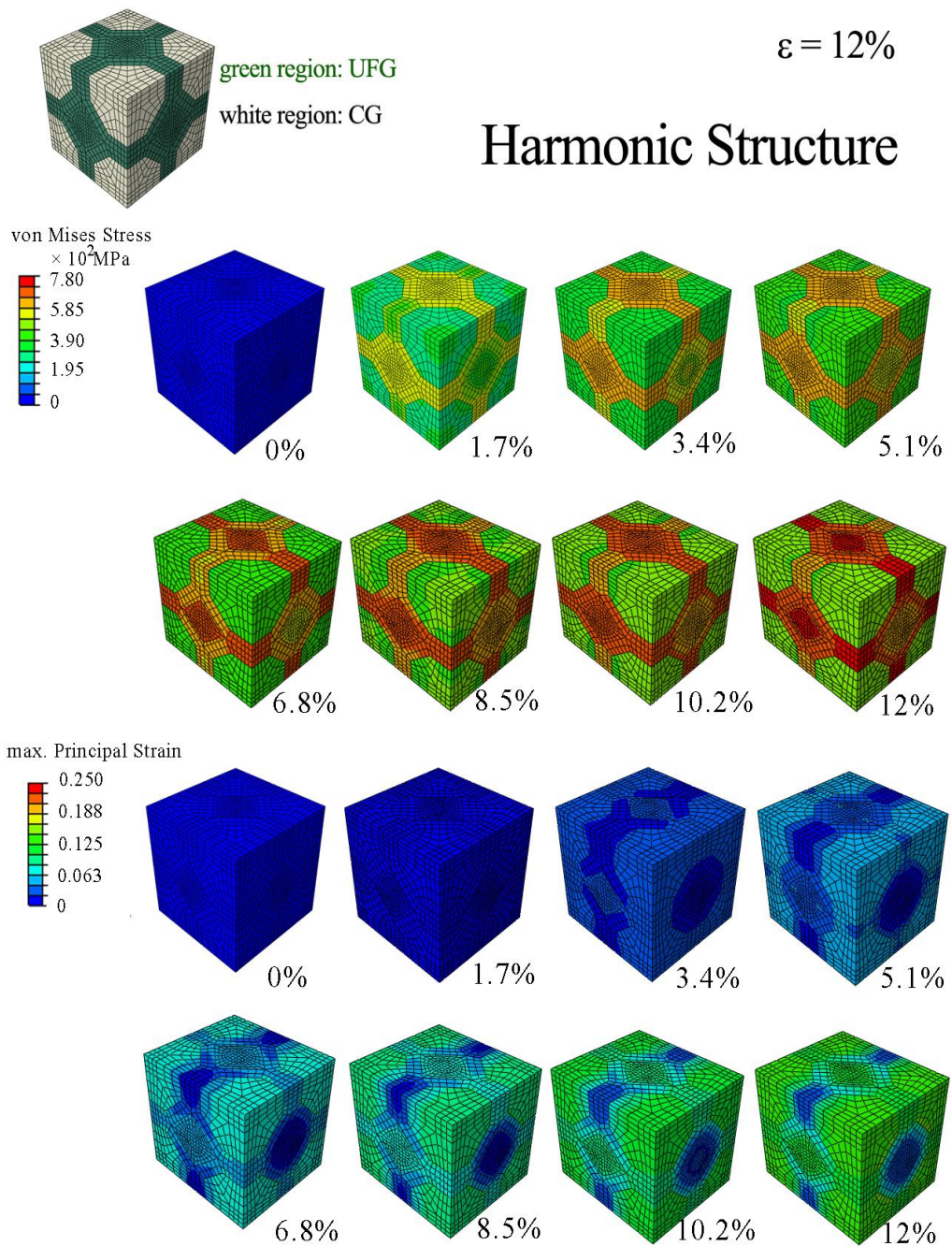


Figure 5.6: Von Mises Stress and max. principal plastic strain distribution along with the deformation for harmonic structure material.

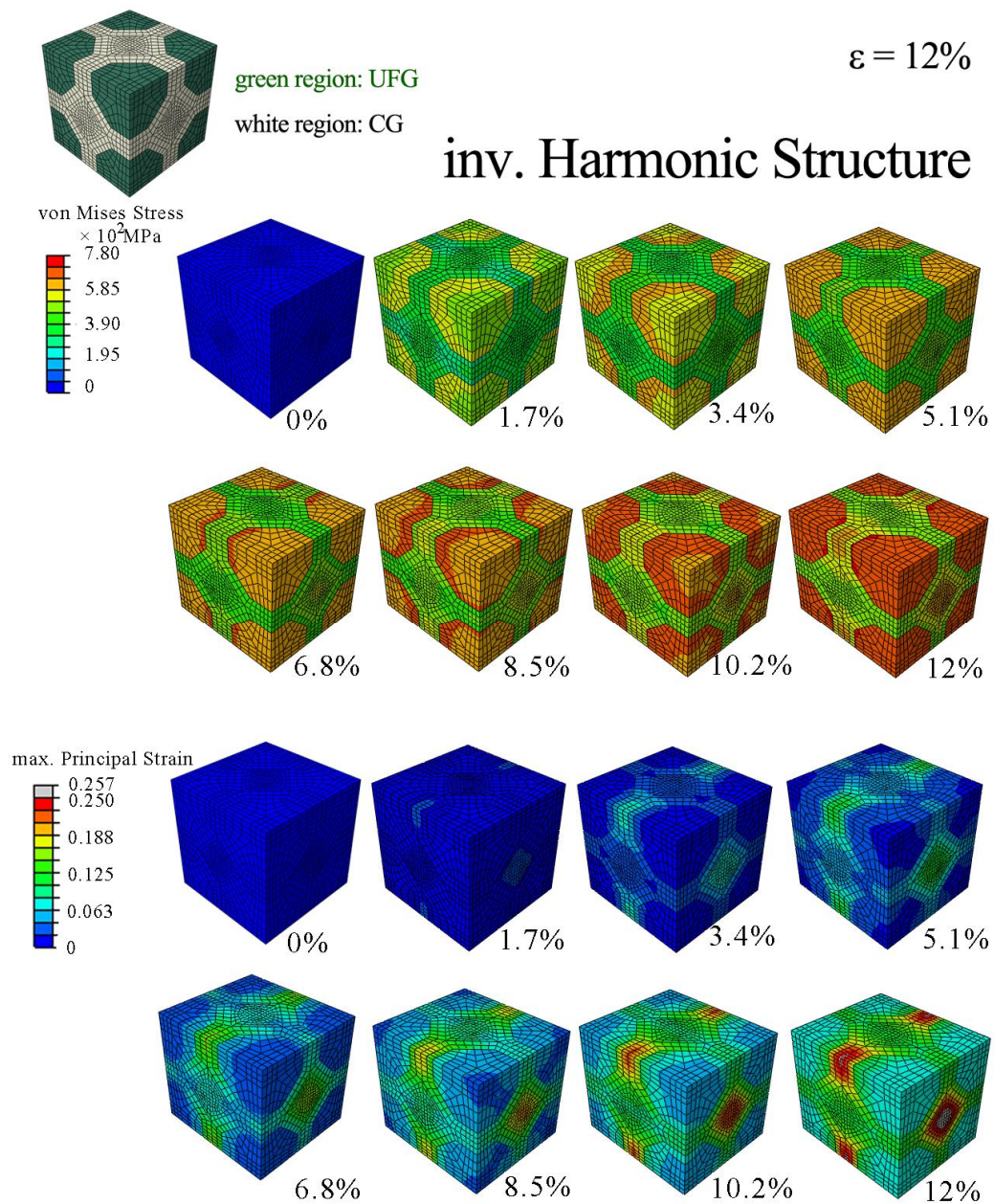


Figure 5.7: Von Mises Stress and max. principal plastic strain distribution along with the deformation for inverse harmonic structure material.

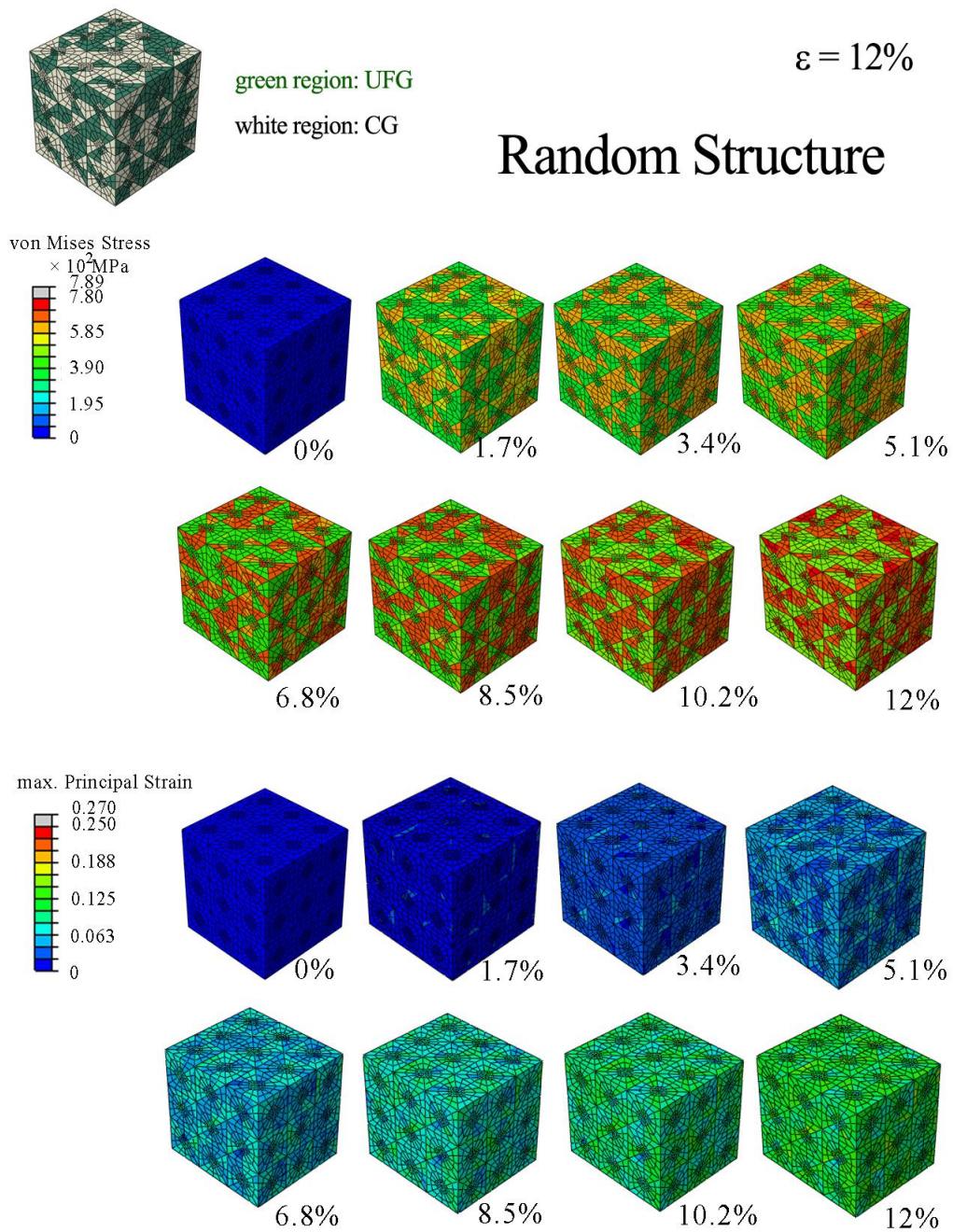


Figure 5.8: Von Mises Stress and max. principal plastic strain distribution along with the deformation for random structure material.

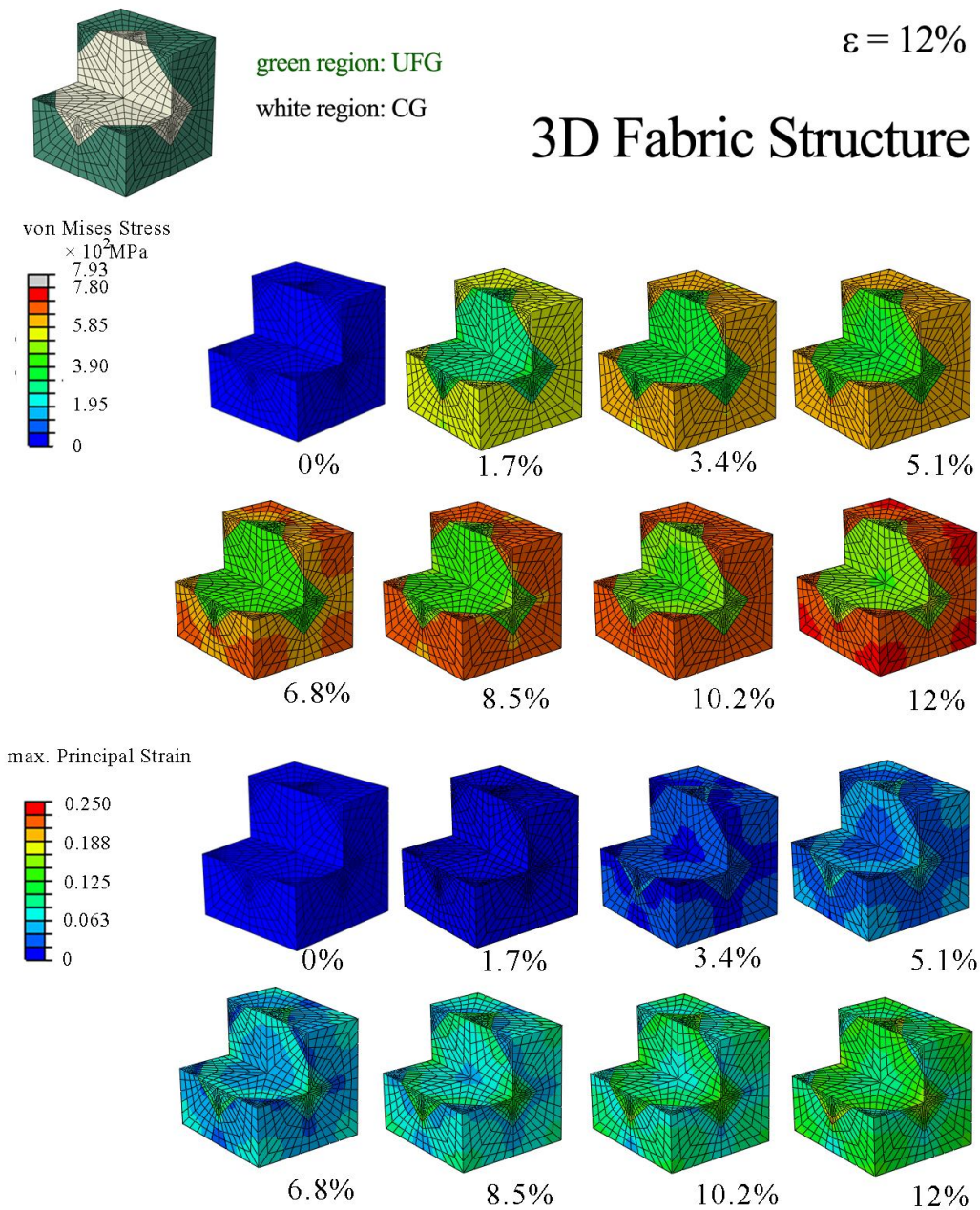


Figure 5.9: Von Mises Stress and max. principal plastic strain distribution along with the deformation for 3d fabric structure material.

5.2.3 Histogram for strain distribution frequency of 4 kinds models

To confirm the disparity between the strain distributions for these four types of structure models, the histograms of strain distribution are obtained. The data in Gauss

quadrature integral point and the elements' volume were utilized. For the strain distributions, the horizontal axis represents the maximum principal strain, whereas the vertical axis represents the volume fraction in the entire model within the scope of the strain. In this result discussion, linear scale and probability scale are both employed for expressing the vertical axis. Linear scale is used to represent the tendency of the whole frequency. Probability scale is applied to represent the strain localization regions because the lower value is always ignored compared to the higher value with linear scale.

Figure 5.10 (1) shows the histogram of CG region strain distribution via linear scale vertical axis. Data represent HS, inv. HS, random structure and 3D fabric structure from the top down, respectively. Through the result, it can be observed that the strain of the HS is concentrated on 0.14, while the other three models show dispersing. The most dispersed model is inv. HS.

Figure 5.10 (3) shows the histogram of CG region strain distribution via probability scale vertical axis. However, the width of the whole bars represents the strain distribution uniformity level of the material. The strain distribution demonstrates more uniform while the width is narrower. Via the result, it can be observed that the HS demonstrates the most uniform strain while the inv. HS shows the most non-uniform. The highest value of HS' model Gauss quadrature integral point strain is 0.156, while inv. HS is 0.254, the random structure is 0.220, the 3D fabric structure is 0.209. It demonstrates that while other three models are showing strain localization in CG region, the HS strain shows well distribution.

Figure 5.10 (2) shows the histogram of UFG region strain distribution via linear scale vertical axis. The lowest peak is shown in inv. HS model near 0.07. The HS shows the second lowest strain peak near 0.09. The random structure and 3D fabric structure shows the strain peak around 0.10. From the result, it can be perceived that the UFG region of inv. HS is most well-protected among the four models, while the UFG region in random structure and 3D fabric structure is almost hardly protected by CG region.

Figure 5.10 (4) demonstrates the histogram of UFG region strain distribution via

probability scale vertical axis. Although the inv. HS shows the lowest peak among the four models, the highest value of HS is 0.14 which is the lowest among the four highest values. It can be demonstrated that the HS strain shows well distribution in UFG region, while the other three models are showing strain localization. However, among these four models, in inv. HS, the width of the whole bars is narrowest, which indicates that the inv. HS UFG region strain distribution uniformity level is highest. The reason the inv. HS shows well strain distribution in UFG region is that the inv. HS is constituted by a high-elongation network CG shell and high-strength UFG cores, which means that the UFG region is well-protected by CG network.

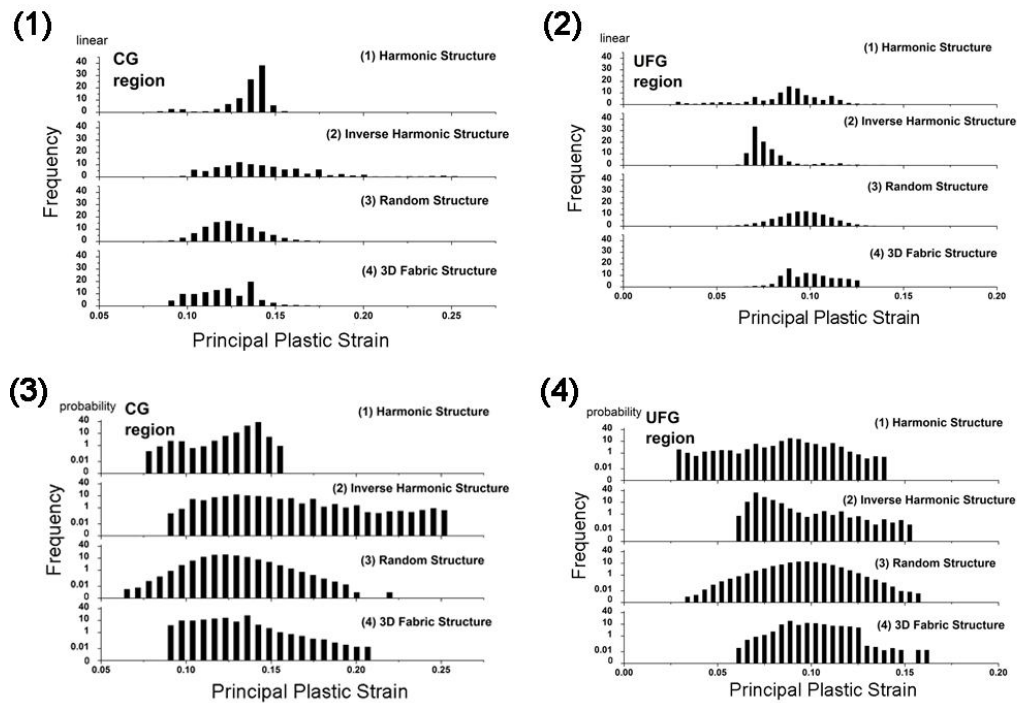


Figure 5.10: Histograms for frequency of max. principal plastic strain: (1) CG region via linear scale vertical axis; (2) UFG region via linear scale vertical axis; (3) CG region via probability scale vertical axis; (4) UFG region via probability scale vertical axis.

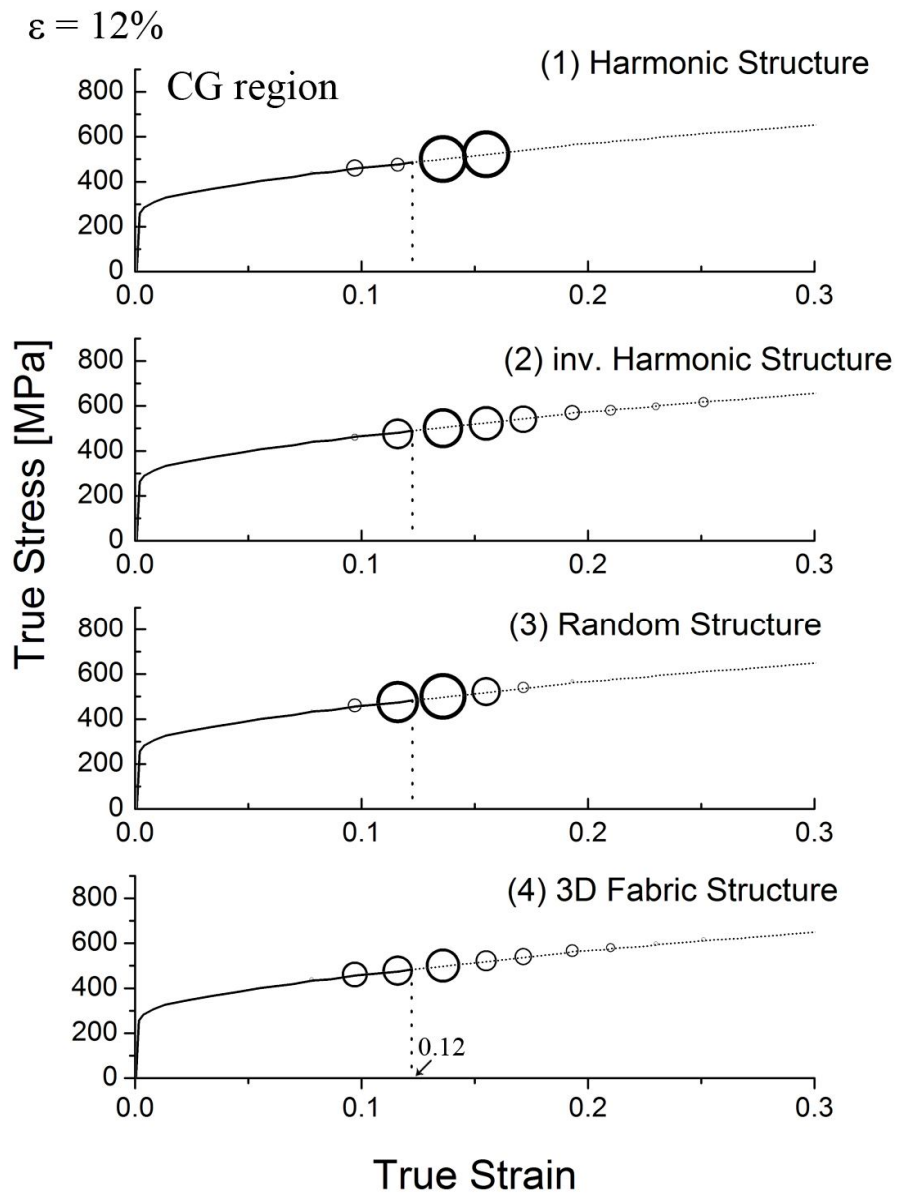


Figure 5.11: Frequency distribution of max. principal plastic strain by circle area of CG region.

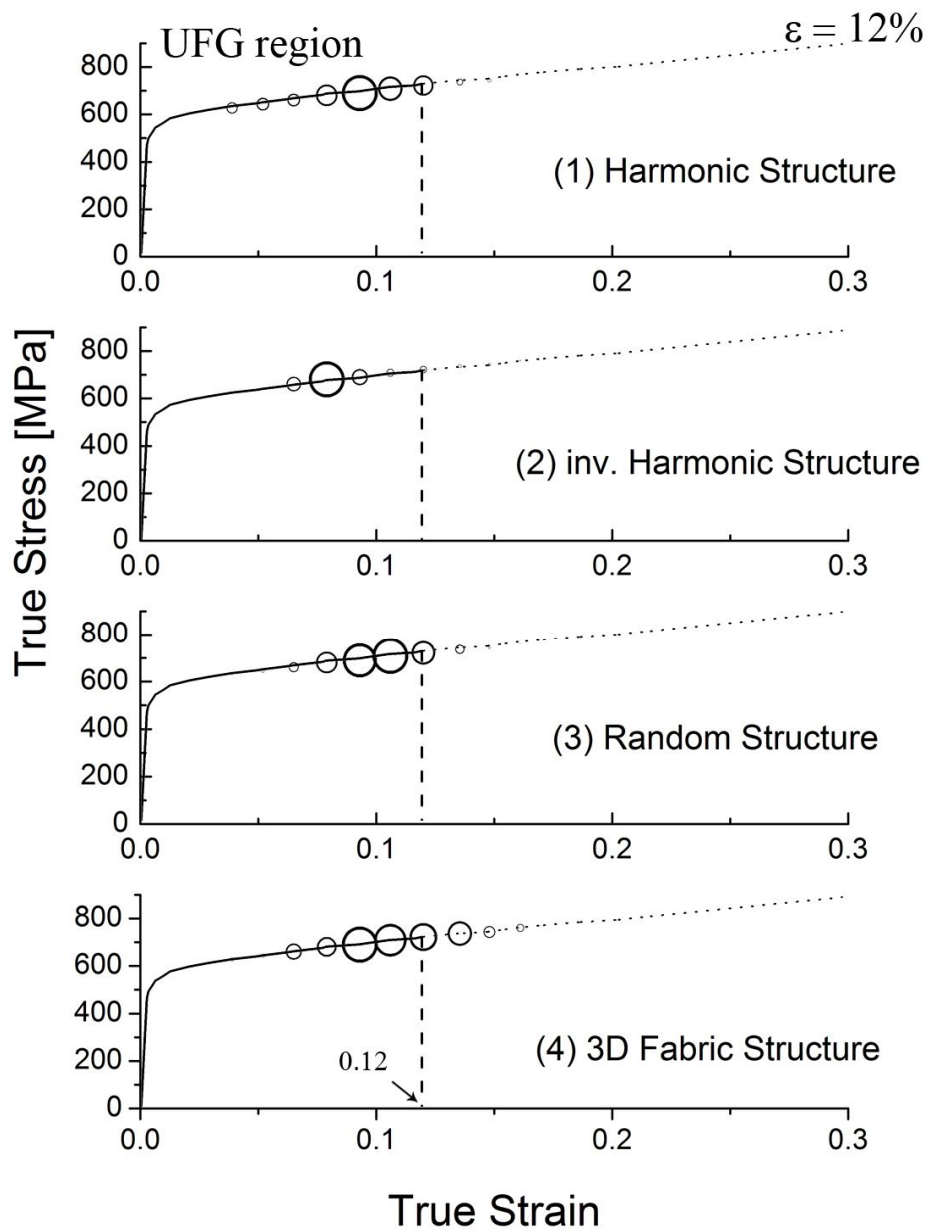


Figure 5.12: Frequency distribution of max. principal plastic strain by circle area of UFG region.

Figure 5.13 demonstrates the histograms for Frequency of max. principal plastic strain of whole region. Figure 5.13 (1) shows the linear scale vertical axis. It can be clearly observed that there are obvious two peaks happened in the HS and inv. HS, while the random structure and 3D fabric structure show nearly one peak. The appearance of two peaks reveals that for HS and inv.HS, the UFG phase suffers less

strain, while the CG phase suffers more strain. It reveals the obvious division of labor that high elongation CG region suffers some strain which should be provided by low elongation UFG region originally. The UFG region is protected by CG region in HS and inv. HS. However, for random structure and 3D fabric structure based on truncated octahedron, there are hardly differences between CG and UFG regions in suffering strain. UFG region in random structure and 3D fabric structure may be the weak parts in where the plastic instability happened. Figure 5.10 (2) demonstrates the probability scale vertical axis for Frequency of max. principal plastic strain. The narrowest distribution range happens in HS. It reveals that the strain of HS shows uniformity in spite of bi-model structure. Moreover, the highest value of HS is smallest in these four kinds of models. While inv. HS shows the widest distribution range and highest max value in these four kinds of models. Although the UFG region is protected by the CG network in inv. HS, CG region will show the cracks early because CG region deforms without restraint.

Wang et al. (2013) raised a 2D FEM simulation to describe nanocomposite failure for epoxy resin with silicon dioxide [2] as Figure 5.14 shown. It is a common example for the traditional compound that introducing hard phase particle contents into matrix to toughen the original homogeneous material. The research reveals the possible scene of tensile test failure part for high strength UFG particle contents filling in high elongation CG matrix. It shows that the UFG particle contents may separate from the CG matrix perpendicular to the tensile test direction. As Figure 5.5 (2) shown, the highest strain happens in the CG region perpendicular to the tensile test direction as same as the Figure 5.14 shown, which shows the research of nanocomposite failure for epoxy resin with silicon dioxide. This phenomenon will make the connection parts between UFG particles and CG matrix decreasing as that just two peak points for each one UFG particle. It will lead to the stress localization happened in the two peak points connecting the UFG particle and CG matrix for each one UFG particle. Hence, although introducing the hard phase contents in soft phase matrix is a common sense to increasing the strength of material, and it has already been widely used. Compared to HS, structure of inv. HS shows obvious weakness

because there is no UFG network structure to restrict the deformation of CG region. Because the elongation of UFG can not keep up with the large deformation happened in a few CG regions. Therefore, the high strain happens in CG region will influence the adjacent UFG region which will bring the high strain happening in the adjacent UFG region and at last tear the adjacent CG and UFG regions because of the strain localization. It can be observed that the connected UFG region plays a significant role in holding high elongation as the bi-modal structure.

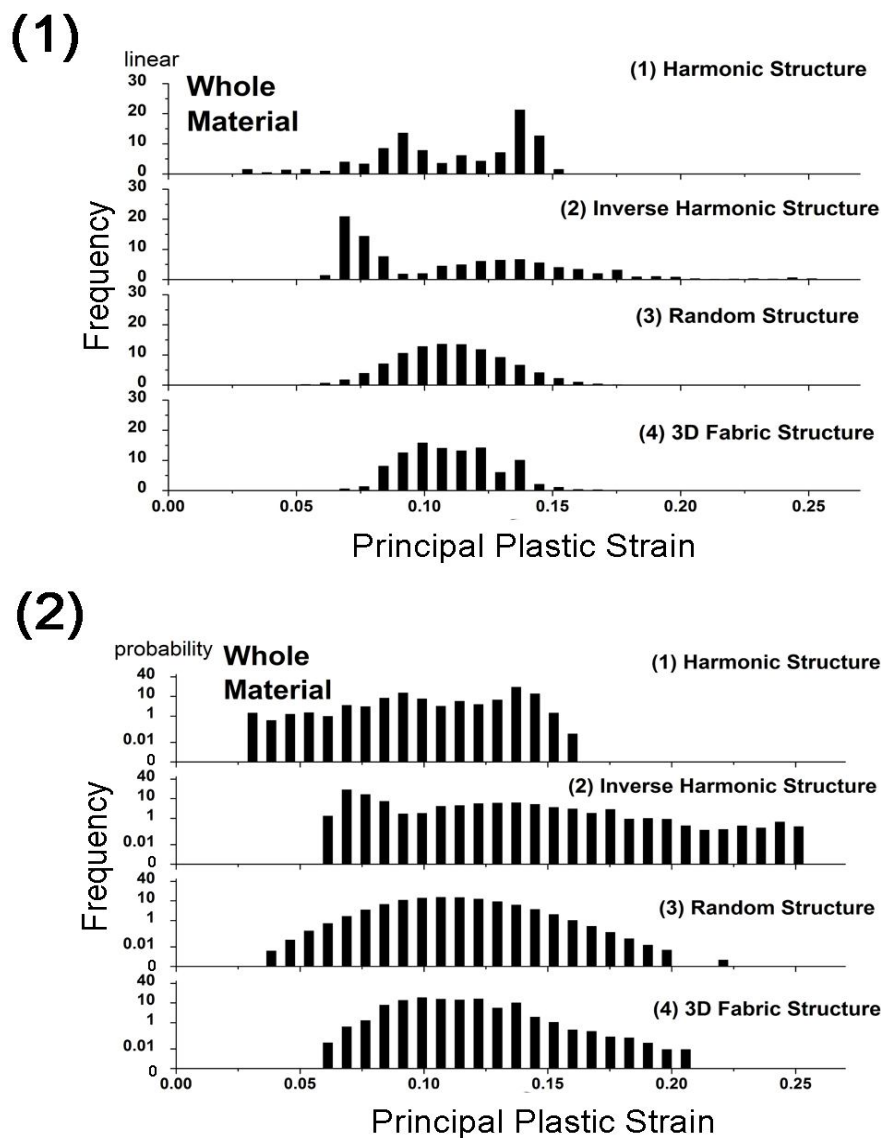


Figure 5.13: Histograms for frequency of max. principal plastic strain of whole region:

(1) via linear scale vertical axis; (2) via probability scale vertical axis.

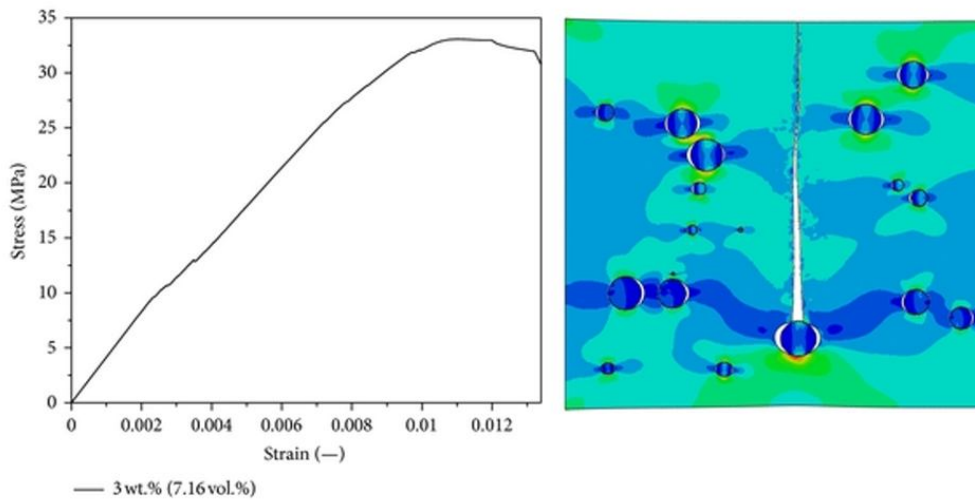


Figure 5.14: Nanocomposite failure for epoxy resin with hard phase particle contents [2].

Copyright © 2013 Zhenqing Wang et al.

5.3 Discussions

5.3.1 Irregular and non-uniform network structure happened

in random structure

From the results, a question is raised why the 3D fabric structure with both UFG and CG network structures doesn't show well performance. If the excellent mechanical performance of HS is just owing to network of UFG region, then the 3D fabric structure should show more superior performance thanks to both UFG and CG network. However, the fact is the 3D fabric structure just show a little better performance than random structure but worse than HS or inv. HS. Hence, the random structure should be got a better view. Figure 5.15 shows the CG region and UFG region of random structure, respectively. From the Figure 5.15, it can be perceived that although the UFG and CG region distributes randomly, but there is hardly individual UFG and CG region. Whatever the connection is tight or loose, the UFG

and CG has been connected by itself chaotically. Put another way, it means that in random structure, UFG and CG region can be treated as a type of chaos and un-regular network structure.

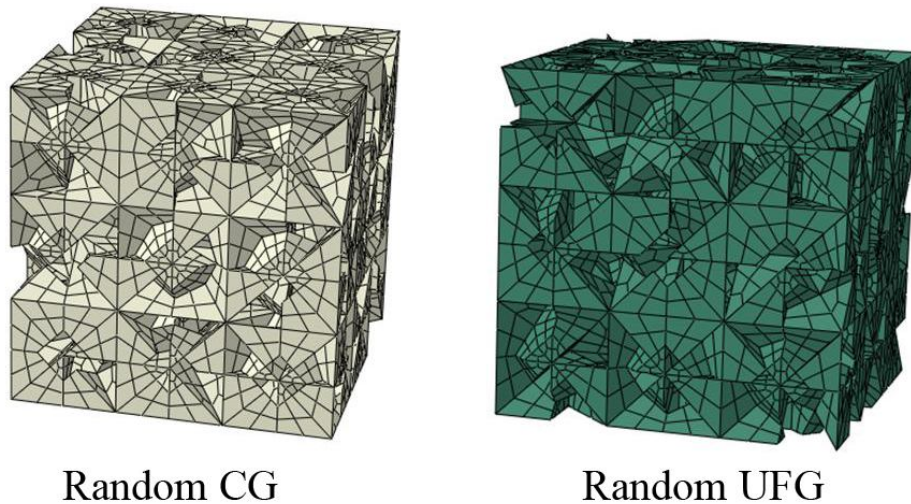


Figure 5.15: CG region meshes for random structure and UFG region meshes for random structure.

Since in random structure, UFG and CG region can be treated as a type of chaos and un-regular network structure. Thus, what is the difference between these network structures in HS and random structure? Figure 5.16 shows the 2D sketch-map of the network structures' connection. For these two models, percentages of black blocks are both 50%. While the widths of every black block in HS network structure are nearly same, widths of black blocks in random structure are varied. In random structure, through widths of some black blocks are thick, in order to make the UFG volume fraction as 50% as HS, some others are very thin as shown in Figure 5.17. However, it is well known that strain and stress localization always happened in the weak region. Hence, no matter how the thick blocks exist, the thin blocks will become the weakness of the whole material. It raised the assumption that not only the network structure but also the thickness here and there of the network decides the mechanical performance. Hence, the random structure shows bad mechanical performance, while the thickness of the network in HS is almost keeping in same value because the shell

is manufactured by MM. After MM, the shape of MM powders has become polygon near sphere. Via gravity and pressure, the powders will array automatically with contact area as large as possible. Hence, it will lead to the result that the thickness of the shell keeps in almost same value.

Network Structure



HS



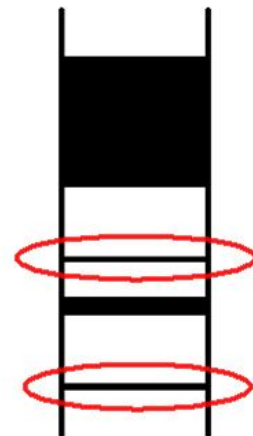
Random

Figure 5.16: The connection network structure for regular HS and irregular random structure.

Network Structure



HS



Random

Figure 5.17: The weakness parts for the network structure of random structure.

5.3.2 The perfect 3D fabric model based on geometry of cube

For the FEM result of 3D fabric structure strain distribution, it can be observed that the strain localization is happened in the connection of CG region. The connection of CG region is the thinnest part of the CG network structure. Because the models are based on truncated octahedron, the thickness of the network is varied. Hence, perfect 3D fabric structure finite element analysis has been raised to validate the assumption as Figure 5.18 shown. Perfect 3D fabric structure is the model with here and there same thickness which is different from the 3D fabric structure based on truncated octahedron. The result demonstrates a uniform strain distribution. Although, there is hardly difference between UFG and CG region, moreover, only from the point of CG region, strain is almost uniform here and there. Strain localization is hardly shown in the perfect 3D fabric structure. The result is in keeping with the general knowledge that the perfect 3D fabric structure shows well mechanical performance, and it is better than the 4 kinds of models which we have discussed earlier. The result shows expectancy which should happened in the 3D fabric model based on truncated octahedron. Hence, the difference between these two kinds of 3D fabric models is significant. However, we found the difference is the uniformity of the connection regions. Consequently, it educed another reason why the HS can demonstrate well mechanical performance, which is the homogeneous thickness of the network.

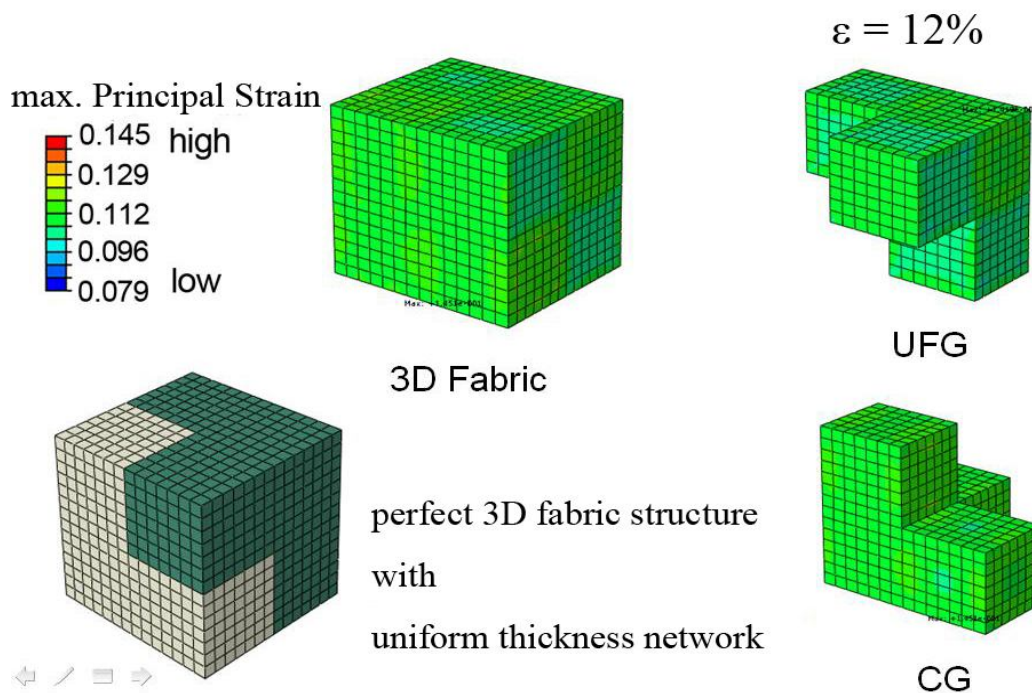


Figure 5.18: Multi-scale FEM model for perfect 3D fabric structure with uniform thickness network; Max. principal strain distribution by $\varepsilon = 12\%$.

Moreover, in HS, not only deformation but also shifting is happened in UFG region (shell region). It will help the UFG region to decrease the stain. As the Figure 5.19 shows, there are two conventional diagrams for deformation and shifting, respectively. For the general deformation in the left side, in order to move the black object from the pink pane into the purple pane, in the horizontal tensile direction, the black object will be stretched. Principal strain of the black object is 30% as the large pane deforming into the small pane. However, for the pure shifting in the right side, the black object just moves from large pane into small pane but not deforms. Principal strain of the black object is 0%. The mechanism of shifting is that the black object has angularity between object itself and tensile direction, while in track of shifting there are no resistance. For HS, as the network structure, most part of UFG region is slanting relative to tensile direction. Moreover, because remaining parts are CG regions, it will lead to the result that in track of UFG region shifting there are less resistance than whole object made by UFG material. Hence, same shifting happens in

UFG region instead of general deformation, which will help the fragile UFG region to defer wrecking process. It will increase the elongation ability of the whole model. Therefore, not only increasing the strength but also ductility, the homogeneous thickness network UFG structure is merit to promote the mechanics properties.

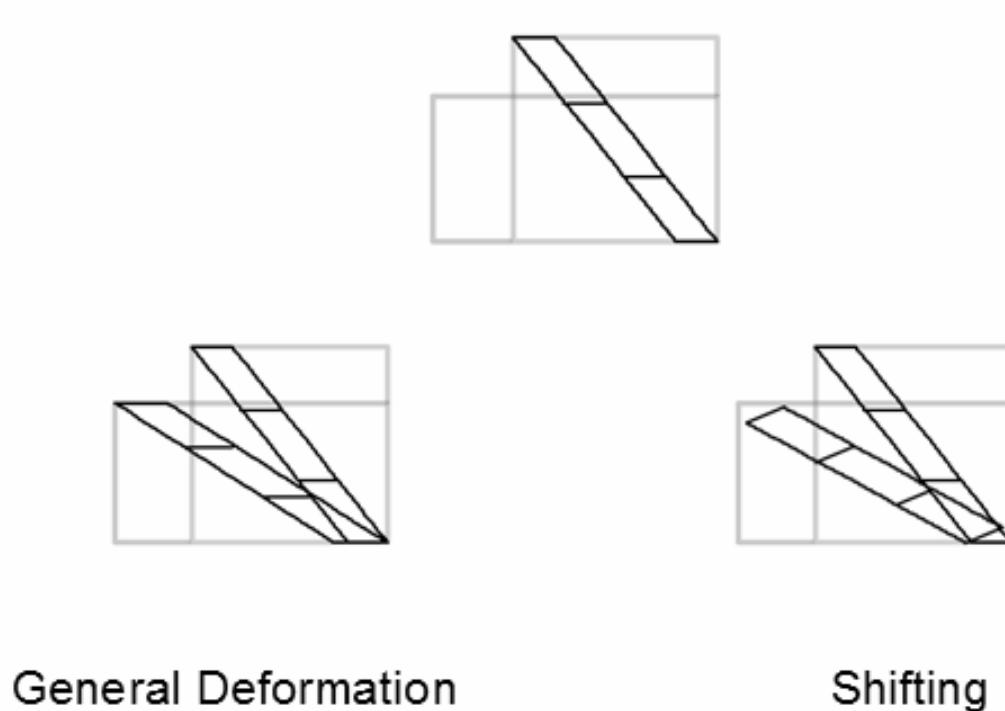


Figure 5.10: The difference between general deformation and shifting.

5.4 Conclusions

1. In this chapter, 4 kinds of 50% UFG volume fraction FEM models based on truncated octahedron have been raised to compare with each other. The results show that all the models show same strength. It indicates that bi-modal materials keep same strength with the same UFG volume fraction and same CG/UFG material characteristics.
2. Harmonic Structure (HS) exhibited better mechanical performance than other three models. Owing to the connection of the UFG phase in the harmonic structure, a non-uniform structure was formed, leading to uniform deformation,

while other models still showed strain localizations.

3. The simulation results for the HS and inv. HS were compared in this chapter. The results indicated that in contrast to HS, without the connection of the UFG phase, the inv. HS clearly experienced strain localization. Without the connection of the UFG phase, the CG phase was forced to undergo more deformation. However, the strain localization of the inv. HS may lead to crack formation, causing these parts to become the weakest regions in the inv. HS material. Hence, the results indicated that with regard to ductility, the HS performed better than the inv. HS.
4. In order to understand if the network structure is the unique characteristic which gives the HS high strength and high elongation, the structure with 3D fabric has been employed in this research. The 3D fabric structure doesn't show expected well mechanical performance because it doesn't have uniform thickness network. It reveals that no matter how many thick regions exist, the thinnest regions of the network will become the shortcomings of the material. Hence, not only the network structure itself, but uniform thickness of network is also significant for ductility increasing.

References

- [1] Yu, E., Sun, J. Y., Chung, H. S., Oh, K. H., 2008. Investigation on thermal properties of Al/SiCp metal matrix composite based on FEM analysis. *Int. J. Mod. Phys. B* 22 (31n32), 6167-6172.
- [2] Wang, Z. Q., Liu, F., Liang, W. Y., Zhou, L. M., 2013. Study on tensile properties of nanoreinforced epoxy polymer: Macroscopic experiments and nanoscale FEM simulation prediction. *Adv. Mater. Sci. Eng.* 2013, 8 pages.
- [3] Kim, Y. R., Souza, F., Teixeira, J., 2013. A two-way coupled multiscale model for predicting damage-associated performance of asphaltic roadways. *Comput. Mech.* 51 (2), 187-201.
- [4] Yang, W. L., Peng, K., Zhou, L. P., Zhu, J. J., Li, D. Y., 2014. Finite element

- simulation and experimental investigation on thermal conductivity of diamond/aluminium composites with imperfect interface. *Comput. Mater. Sci.* 83, 375-380.
- [5] Zhou, D.W., Stronge, W.J., 2006. Low velocity impact denting of HSSA lightweight sandwich panel. *Int J Mech Sci*, 48, 1031–1045
- [6] Shao, D., Gao, D., Wei, Q., Zhu, H., Tao, L., Ge, M., 2010. Structures and properties of the polyacrylonitrile fabric coated with ZnO–Ag composites. *Appl. Surf. Sci.* 257(4), 1306-1309.
- [7] Allaoui, S., Hivet, G., Wendling, A., Ouagne, P., Soulat, D., 2012. Influence of the dry woven fabrics meso-structure on fabric/fabric contact behaviour. *J. Compos. Mater.* 24 pages.
- [8] Lin, H., Ramgulam, R., Arshad, H. Clifford, M.J., Potluri, P., Long, A.C., 2012. Multi-scale integrated modelling for high performance flexible materials. *Comput. Mater. Sci.* 65, 276–286.
- [9] Dinh, T. D., Rezaei, A., Puystiens, S., Van Craenenbroeck, M., Carbonez, K., De Laet, L., Mollaert, M., Van Hemelrijck, D., Van Paepegem, W., 2015. A study of tension fabric membrane structures under in-plane loading: Nonlinear finite element analysis and validation. *Composite Structures*, 128, 10-20.
- [10] Liu, Y., Hu, H., 2015. Finite element analysis of compression behavior of 3D spacer fabric structure. *Int. J. Mech. Sci.*, 94, 244-259.
- [11] Zhou, Y., Chen, X., 2015. A numerical investigation into the influence of fabric construction on ballistic performance. *Compos. Part. B: Eng.* 76, 209-217.

Chapter 6: Effect of UFG volume fraction and CG/UFG material characteristics in harmonic structure material

6.1 Effect of shell volume fraction in harmonic structure material

6.1.1 FEA models with 5 kinds of UFG volume fraction for harmonic structure and random structure

For the harmonic structure, change of UFG volume fraction will decide the thickness of the network. In order to understand the effect of the thickness of the network, different UFG volume fraction simulations for harmonic structure have been raised in this part.

For this discussion, 5 kinds of UFG volume fraction have been employed--20%/ 43%/ 50%/ 57%/ 70% (Figure 6.1). This five numbers are not regular integral number as 30/ 40/ 50 et al. since meshing step for harmonic structure is complex and consuming time. Hence, harmonic structure models with these UFG volume fractions are produced to match along with harmonic structure experiments. This simulation is to reveal the strain distribution tendency with UFG volume fraction change. At the same time, random structure models with same UFG volume fractions have been raised to compare with the harmonic structure. Figure 6.1 shows the HS and random structure models. Green parts represent UFG regions, while the white parts represent CG regions.

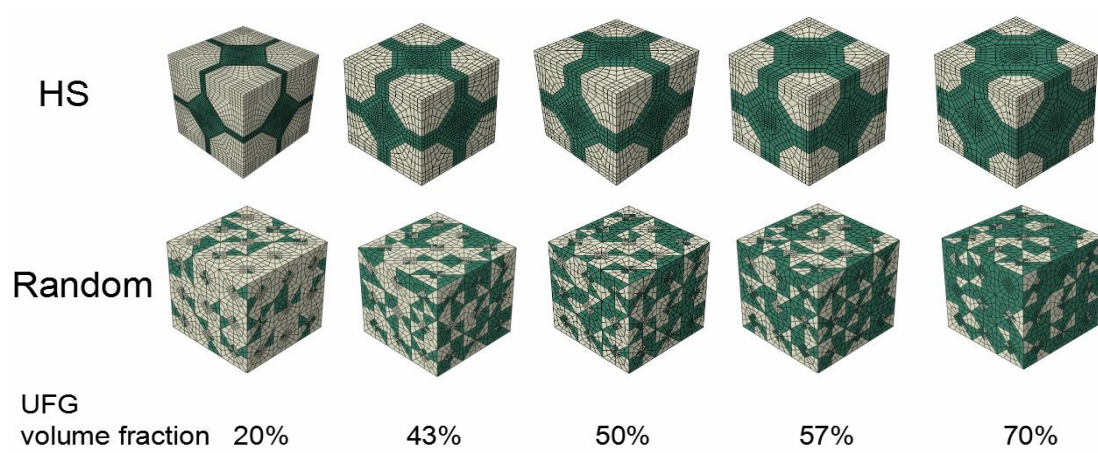


Figure 6.1: Multi-scale FEM models for different UFG volume fractions for harmonic structure and random structure.

Figure 6.2 shows the true stress-strain curve of these bi-modal structure models. Via the results, it can be observed that the yield strength of the bi-modal structure increased with the UFG volume fraction. While with the same UFG shell fraction, the HS and random structure show almost the same yield stress. It can be observed that there are relationships between strength and UFG volume fraction. The value of yield stress is raised with the increment of the UFG volume fraction.

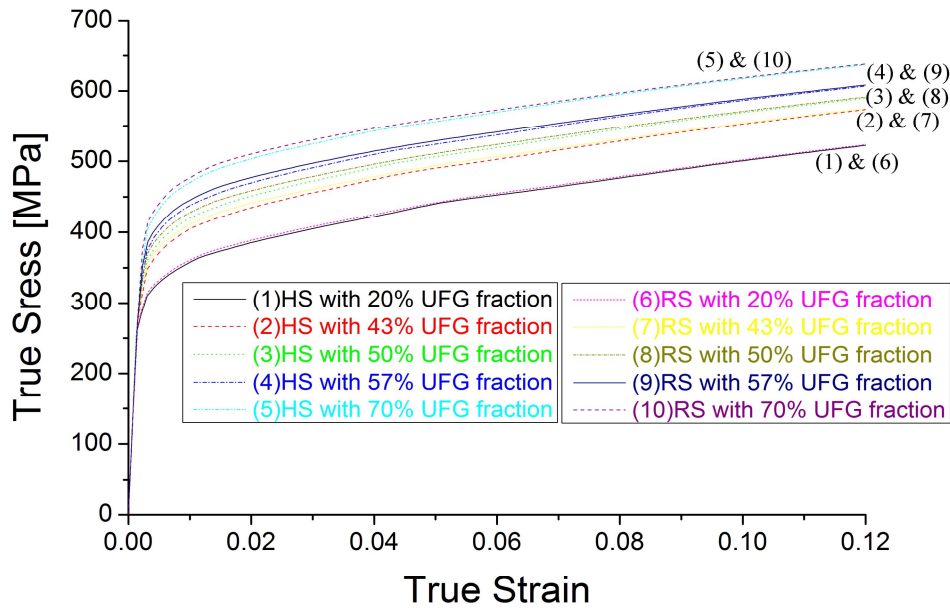


Figure 6.2: Multi-scale FEM results of true strain-stress curves with different UFG volume fraction for harmonic structure and random structure.

6.1.2 Stress and strain contour distribution

For the Von Mises Stress distribution of these models (Figure 6.3), it is clearly observed that main degree of stress happens in UFG region both in HS model and random model. From the different color regions of the stress distribution, the UFG region and CG region can be distinguished obviously both in HS model and random structure model as the red and yellow regions represent UFG regions while the blue regions represent CG regions. Meanwhile, for HS models, it can be clearly observed that Von Mises Stress value of the CG region increase with the increment of UFG volume fraction. Because there is a corresponding relation between stress and strain, it means that, the average CG regions' strain value of the 70% UFG volume fraction model is larger than the average CG regions' strain value of the 20% UFG volume fraction model.

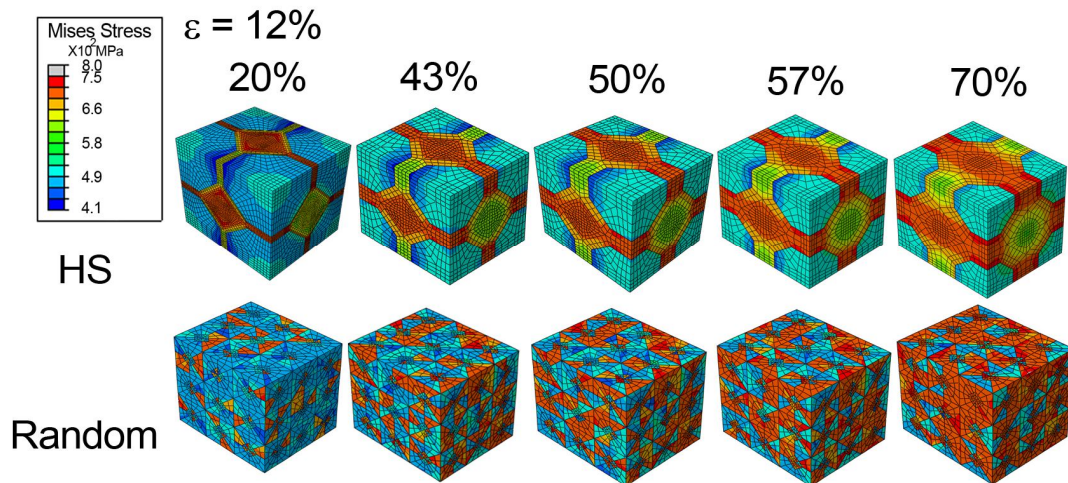


Figure 6.3: Von Mises Stress distribution of the harmonic structure and random structure for different UFG volume fractions.

For the max. principal plastic strain distribution of these models (Figure 6.4), there are obvious differences between HS model and random structure model. For HS, it distinctly shows that CG regions show higher strain relative to UFG regions. Moreover, as the UFG volume fraction increasing, the CG regions show higher strain in HS models tally with Von Mises Stress results (Figure 6.3). In contrast, it is impossible to differentiate different UFG shell fraction random structure models, because all the random structure models show almost same phenomenon. There are a few strain localization happening in the random structure models and the remaining parts in the model show almost same strain. Moreover, the mainly strain localization show in CG regions while some strain localization still show in UFG regions in random structure. Not just CG regions suffer high strain but UFG regions should also suffer parts of high strain.

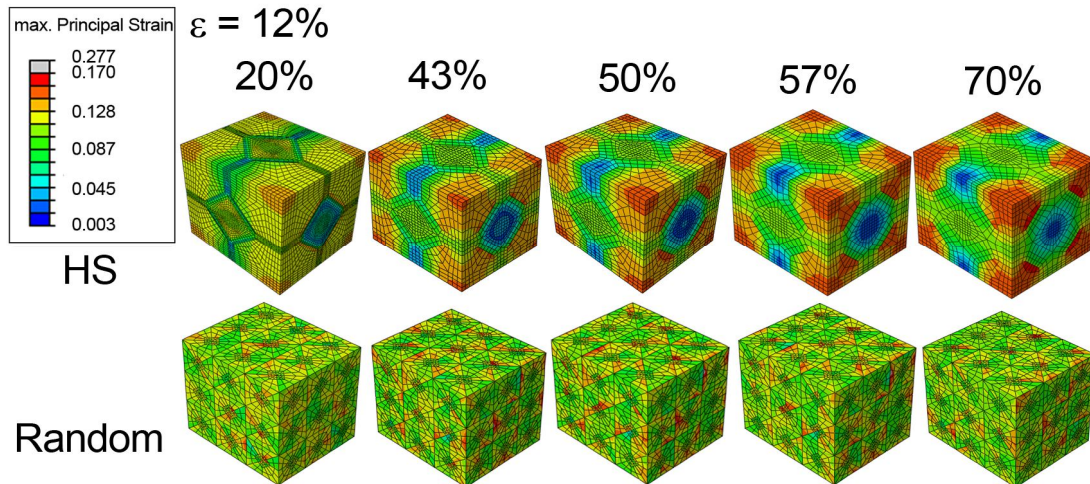


Figure 6.4: Max. principal plastic strain distribution of the harmonic structure and random structure for different UFG volume fractions.

6.1.3 Histograms for strain distribution

Figure 6.5 demonstrates strain frequency histogram of CG region: (a) linear vertical scale; (b) probability vertical scale. The red bars reveal the results of harmonic structure. Meanwhile the black bars reveal the results of random structure. From the Figure 6.5 (a), the peaks of random structure models are almost in the same position which is near 0.12, meanwhile, the peaks of harmonic structure models show obviously movement. Although when the UFG volume fraction is 20%, the peak of plastic strain frequency of harmonic structure is 0.12. While the UFG volume fraction is 70%, the peak of plastic strain frequency of harmonic structure is near 0.15. Along with the UFG volume fraction increasing, peak of plastic strain frequency shift to the right obviously. In the case of 20% UFG fraction, CG regions occupy most regions in the whole model. Hence, the peak of the CG regions is near the whole strain 0.12 which is as regular result. However, in the case of 70% UFG fraction, the peak values of harmonic structure and random structure show large difference. It demonstrates that although the CG volume fraction decrease, the CG regions in harmonic structure suffers much strain which the UFG regions should suffered originally, while the CG regions in random structure almost don't help to share this part of strain. As Figure

6.5 (b) shown, no matter from 20% to 70% UFG volume fraction, distributions of plastic strain frequency in harmonic structure are narrower than frequency in random structure. Especially the random structure results appear in the high strain territory, except of the model with 20% UFG volume fraction, other models show highest strain near 0.2. Nevertheless, the highest value for harmonic structure is just near 0.17. The respectively uniform strain distribution which appears in harmonic structure demonstrates the harmonic structure can show uniform deformation even if harmonic structure is a type of heterogeneous bi-modal structure.

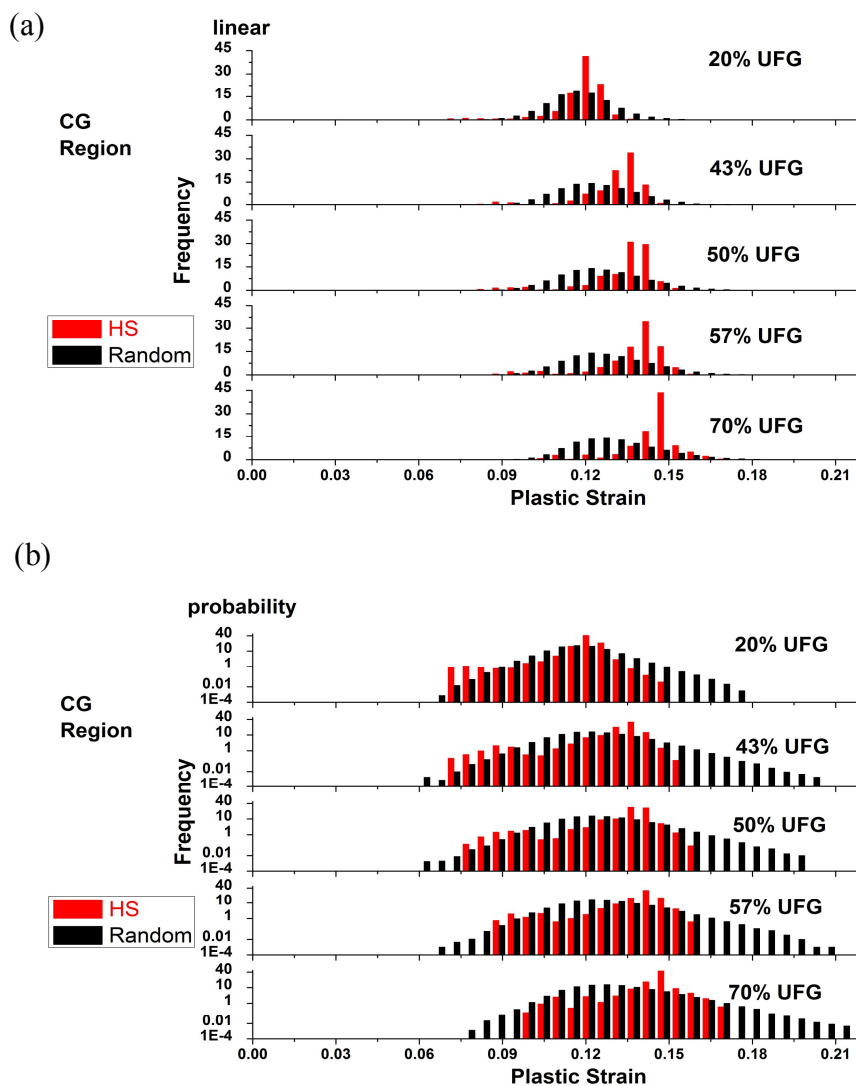


Figure 6.5: Strain frequency histogram of CG region: (a) linear scale; (b) probability scale.

Figure 6.6 reveals strain frequency histogram of UFG region: (a) linear vertical scale; (b) probability vertical scale. It is same with CG region histogram that the red bars reveal the results of harmonic structure. Meanwhile, the black bars reveal the results of random structure. In Figure 6.6(a), the peaks of random structure models are almost in the same position which is near 0.1, which is relatively immobilized to harmonic structure. Along with the UFG volume fraction decreasing, peak of plastic strain frequency shifts to the left obviously. Although in the case of 70% UFG fraction, when UFG regions occupy most regions in the whole model, the peak of harmonic structure shows near 0.1, which is a little left relatively to random structure. In the case of 20% UFG fraction, the peak of harmonic structure is just 0.075. From the results in Figure 6.5 and 6.6, it can be revealed that, in harmonic structure, CG regions suffer more strain and UFG regions suffer less strain than CG regions and UFG regions in random structure, respectively.

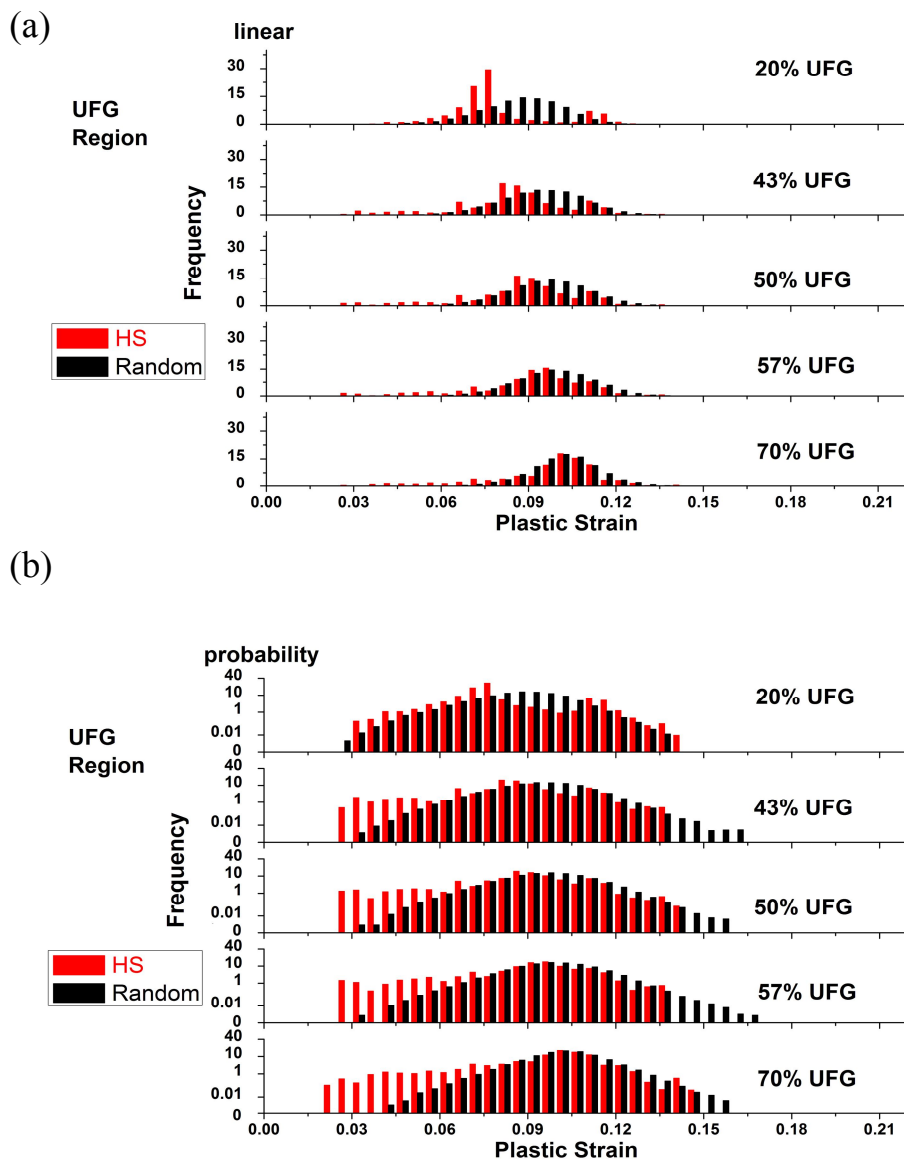


Figure 6.6: Strain frequency histogram of UFG region: (a) linear scale; (b) probability scale.

6.2 Effect of CG/UFG material characteristics in harmonic structure material

6.2.1 FEA models with different CG/UFG material characteristics

Effect of CG/UFG material characteristics in harmonic structure material will be discussed in this part. Via changing CG/UFG material characteristics, it can be observed that how the gap of the CG/UFG material changed the material mechanical

performance. At the same time, random structure models with same CG/UFG material characteristics have been raised to compare with the harmonic structure (Figure 6.7). In this research, a UFG volume fraction of 53% harmonic structure model has been applied. The CG material characteristics of every model are kept in the same value, while the UFG material characteristics changed. As the grain size of CG material is 2/4/10/20 times of UFG grain size. Then, the immovable yield stress of CG material is 274 MPa, at the same time, yield stress of UFG is 314/371/484/611 MPa, respectively.

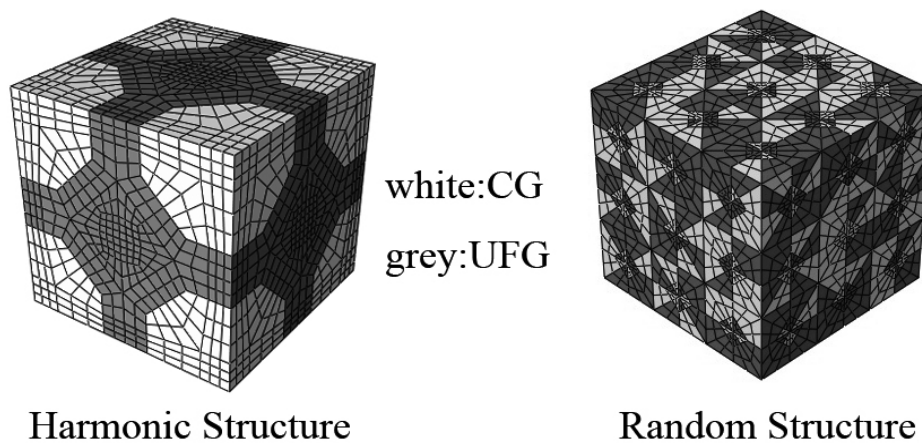


Figure 6.7: Harmonic and random structure multi-scale FEM model with same UFG volume fraction of 53%.

Figure 6.8 shows the multi-scale FEM results of true strain-stress curves with different CG/UFG material characteristics for harmonic structure and random structure. While within the same ratio of CG/UFG material characteristics, the harmonic structure and random structure reveal almost the same yield stress.

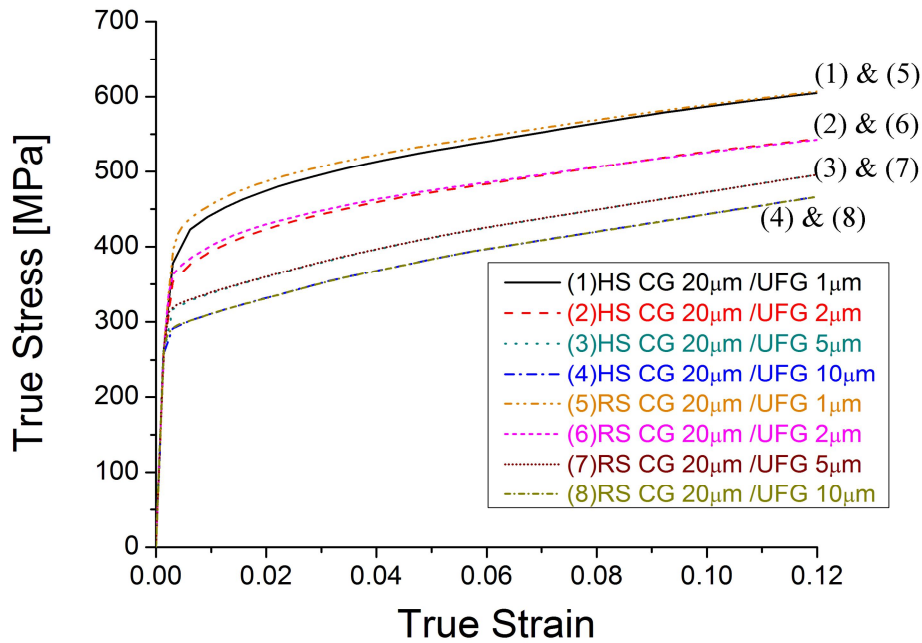


Figure 6.8: Multi-scale FEM results of true strain-stress curves with different CG/UFG material characteristics for harmonic structure and random structure.

6.2.2 Stress and strain distribution

Figure 6.9 shows the Von Mises Stress distribution of these models. From the result, it can be observed that as the gap of CG and UFG grain size enlarging, the von Mises Stress disparities shown between CG and UFG regions increase both for harmonic structure and random structure. Nevertheless, although the CG material characteristics are same for all the models, the Von Mises Stress values shown in CG regions still grow with the gap enlarging of CG and UFG grain size. The Von Mises Stress shown in CG regions is affected by the material characteristics of adjacent UFG regions.

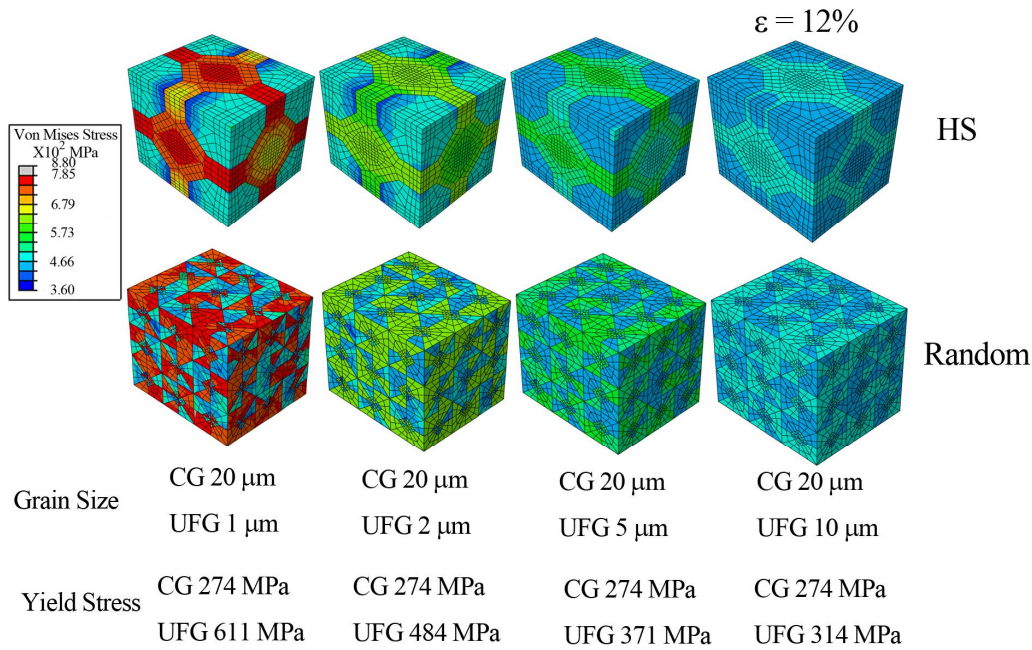


Figure 6.9: Von Mises Stress distribution with different CG/UFG material characteristics in same volume UFG fraction of 53%.

Figure 6.10 shows the max. principal plastic strain distribution of these models. From the results, it can be observed that as the gap of CG and UFG grain size enlarging, strain distribution disparities appear. However, when the model is an ideal homogeneous model, it will show uniform strain. Hence, while the gap of CG and UFG material characteristics is small, the result of harmonic structure is closed to random structure. Nevertheless, when the gap of CG and UFG material characteristics is large, harmonic structure and random structure show disparity in strain distribution which is described in Chapter 4. Random structure shows some strain localizations and the remaining parts can not be distinguished if the parts are UFG regions or CG regions.

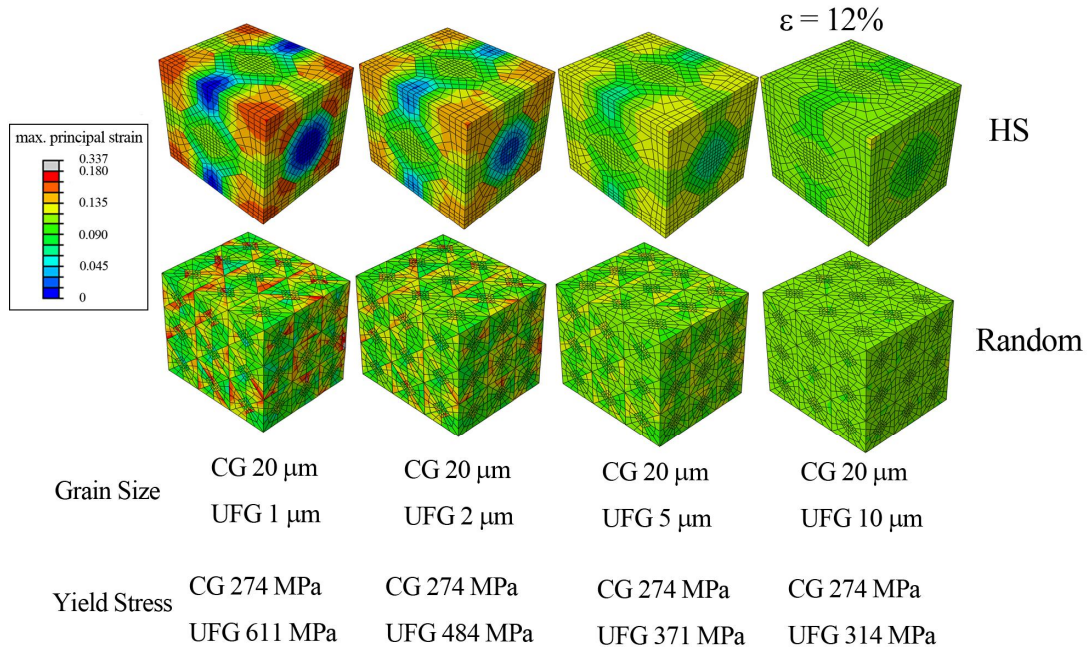


Figure 6.10: Max. principal plastic strain distribution with different CG/UFG material characteristics in same volume UFG fraction of 53%.

6.2.3 Comparison of max stress/strain values of these bi-modal harmonic and random structures

To find out the discipline of CG/UFG material characteristics' change, the comparison of max stress/strain values has been raised. Figure 6.11 (a) shows the max. Von Mises Stress values of these models. As the gap between the CG and UFG material characteristics enlarging, the value of max stress gets higher. It can be observed that the max value of random structure is always higher than HS which is in the same CG/UFG material characteristics with random structure. While the CG and UFG grain sizes are same--the material is equal to homogeneous material, the values of the two models' max stress are same. However, as CG and UFG grain sizes' distance enlarging, the gap of the HS and random structure max stress values gets larger. It can be noticed that without network structure of harmonic structure, the general random structure will show the plastic instability early. Moreover, Figure 6.11 (b) shows the max. principal plastic strain values of these models. In the plastic

deformation region, the stress-strain curve is flatter relative to elastic deformation region. Therefore, the stress value changes a little as the strain value changes a lot in the plastic deformation region. Hence, compared to the Von Mises Stress value, the principal plastic strain value represents the disparity of HS and general random structure more clearly. From the result of the max. principal plastic strain values of these models, it can be noticed that when grain size of CG material is 20 times of UFG grain size, the strain value difference between HS and general random structure is significantly huge---as the max value of HS is 0.174, while the max value of random structure is 0.337. The max strain value of random structure is almost 2 times as much as the max strain value of HS. Although the amount of strain localization regions is little, severe strain localization regions in the random structure will lead to crack easily. With deformation restraint by the regular uniform thickness network shell, the strain localization is evaded in harmonic structure. CG regions (cores) in harmonic structure keep uniform deformation as the homogeneous material.

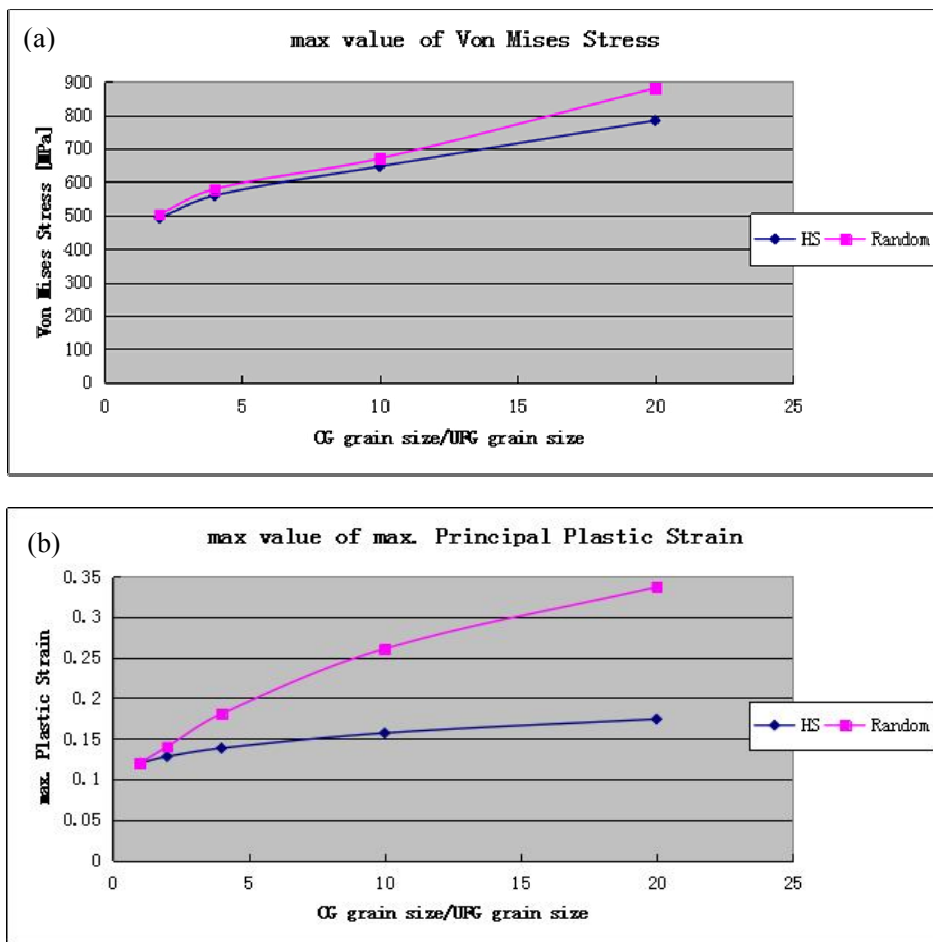


Figure 6.11: Max value for the Von Mises Stress and max. principal plastic strain for harmonic structure and random structure with different CG/UFG material characteristics in same volume UFG fraction of 53%.

6.3 Conclusions

In this chapter, effects of UFG volume fraction and CG/UFG material characteristics in harmonic structure material have been discussed.

1. For the effect of UFG volume fraction transition, 5 kinds of UFG volume fraction have been employed--20%/ 43%/ 50%/ 57%/ 70%. In the middle of the volume fraction as the UFG volume fraction and CG volume fraction are nearly equal to each other, the preponderance of harmonic structure is extremely obvious that the peak of strain of CG region of harmonic structure shows

higher while the max value of strain of harmonic structure is lower compared to random structure model. Moreover, in the edge of the volume fraction as the UFG volume fraction is just 20%, although the advantage of harmonic structure is not as clear as the 50% UFG volume fraction model shown, harmonic structure model still shows better mechanical performance than random structure. The better mechanical performance reveals in that in CG region, the random structure models always show strain localization while the harmonic structure models avoid the strain localization. Moreover, for 20% UFG volume fraction models, the peak of strain frequency in UFG region of harmonic structure show lower value than random structure, and for 70% UFG volume fraction models, the peak of strain frequency in CG region of harmonic structure show higher value than random structure. These results demonstrate that, in harmonic structure the CG region undertakes more strain than the CG region in random structure. Hence it reveals that the UFG region in harmonic structure is protected by CG region through bearing less strain, while the UFG region has to undertake same strain with CG region in random structure.

2. For the effect of CG/UFG material characteristics in harmonic and random structure material, harmonic and random structure models with grain size of CG material 2/4/10/20 times of UFG grain size have been employed to compare. From the max value comparisons of Von Mises Stress and max. principal plastic strain for harmonic structure and random structure with different CG/UFG material characteristics in same volume UFG fraction of 53%, it can be demonstrated that while the ratio of CG grain size and UFG grain size is low, harmonic and random structure models both approach to homogeneous CG material, the difference between harmonic and random structure is slight. However, with the increase of the ratio of CG grain size and UFG grain size, harmonic structure model reveals better mechanical performance than random structure, the superior of harmonic structure is more obvious.

Chapter 7: Application of deformation behavior of harmonic structure based on digital image correlation

7.1 Introduction of digital image correlation

In engineering practice, strain measuring can be performed in various ways and in general the techniques can be divided into contact measuring and non-contact measuring. Digital image correlation (DIC) is an effectual optical method which applies tracking and image registration techniques for accurate 2D measurements of changes in images due to its high accuracy and ease of use [1-16]. In a DIC analysis, the displacement and strain distribution of a test specimen can be obtained by correlation comparison between two high contrast digital images taken from before and after deformation states. The two high contrast digital images are compared by the data of luminance difference which can be quantified as similar degree. The images can be divided into many neat little regions. The two regions with the same coordinates and neighboring coordinates in the two images will be compared. As the similar degree is higher than a setting value by user, the two regions in the two images can be treated as same regions. The use of image correlation is at pixel level or even can be at the subpixel level [13].

The DIC analysis is often used to measure deformation (engineering), displacement, strain, and optical flow, and it is widely applied in many areas of science and engineering. DIC techniques have been increasing in popularity, especially in micro- and nano-scale mechanical testing applications due to its relative ease of implementation and use. Driven by the recent advances in materials and biological research, there is a growing requirement for measurable deformation analysis at the microscale.

7.2 Circumspect parts for use of tensile test specimen photos for DIC

In this research, a without post treatment DIC soft programmed by Kyoto university Tsuji lab is employed to measure harmonic structure deformation during tensile test. This DIC soft can export the observing point's coordinates of before and after deformation. SUS304L 100h MM harmonic structure and SUS304L initial powder have been employed to compare in this research. For the digital image correlation, marks are significant for location. In this research, the grain boundaries have been employed as marks.

Because the DIC soft should compare two photos before and after stretching by luminance difference in many little regions which are always set to 25×25 . While the real object deformation step length is too large, the result of DIC will be imprecision. It means that if the center of a grid deforms above 5 pixels, then the soft can not distinguish the grid after deformation. Then the soft will just pick a coordinate wide of the mark. Moreover, the error will extend to the whole line of grids. Hence, the result is that the calculation will stop after these error grids. In order to deal with this problem, the multiple steps can be employed. In order to get the clear photos for the DIC soft, two significant steps should be raised, first is mark on the surface; second is step length.

First, the marks should be set in surface of the tensile test specimen to help to recognize by soft. There is no need to observe the whole grain boundaries, because the whole acidizing specimen for OM (optical microscope) will bring the fragile surface for the tensile test specimen. However, in order to obtain the strain distinctions between CG and UFG, in this research, the light acidizing has been employed to observe the boundary of the UFG and CG regions. Afterwards, it will still bring a little influence to the tensile test.

Second, the length of step should be small, thus the soft can recognize the same grids. We chose to process the tensile test by 5% of length firstly. Because the acidizing, the specimen become fragile, after second time of stretching the specimen become

collapse. Then we choose to process the tensile test by each time 3% of length. As a result, there are obvious cracks happened the tensile test specimen after three times 3% stretching. It is inescapability, and the surfaces of the specimens have become concavo convex after stretching. The specimen can not be polished again, because after polishing, the distinguishing feature identified by the soft will disappear. The OM can not focus on the whole surface simultaneously. Hence, the 6% strain stretching is employed in this research.

For this DIC soft, the calculation principle is that calculation is from upper left first grid. Because the soft can just find the grid which move within 5 pixels but the totting-up deformation for the whole object will surpass 5 pixels as the grids in the right part, it will be error until the soft scans to right part. For the DIC soft, it can not modify error automatically. The error will continue to neighbor grid and then next grid, and after about five error grids finally it will lead to the stop of the calculation. In order to deal with this problem, each calculation for the grid is based on the left grid, except for the far left grid. For example, if the first grid (named: a) moved left 4 pixels after deformation, and the next grid (named: b) is based on the new coordinate and moved left 3 pixels after deformation. For the b grid, the real moved distance is 7 pixels. For this soft with the upper limit deformation of 5 pixels, the b grid can not be calculated precisely. Hence, instead of being calculated based on the origin grid before deformation, calculation based on the previous grid relatively has been employed. This method will help to disperse the deformation to each grid and reduce the amount of calculation. However, for the large scale object, there are still problems. After tensile test, a slight unevenness will happen in the surface, even if the unevenness is hard to be observed by eyes, it will affect the focus of the OM. In the high magnification of OM, the unevenness surface will not show clear because the focal lengths here and there are different. Hence, whole object will be separated to several parts to take photo. The before and after deformation photos will be taken by each part that between the neighbor parts there is overlapping region. After taking photos for each region, the results will be jogged together by “Adobe Photoshop” software. Because the boundary of CG and UFG is clear to observe, the extra marks

are not needed. The boundary of CG and UFG can be the mark to take the photos. I took 3 lines, 6 rows photos which conclude totally 18 pieces of photos to make one whole photo. Figure 7.1(1) shows manufacture of the photo in whole strain with $\varepsilon = 0\%$. It can be observed that there are overlapping regions between neighbor parts, and it will help to jog together the photos. The photos in whole strain with $\varepsilon = 3\%$ (Figure 7.1 (2)) and $\varepsilon = 6\%$ (Figure 7.1 (3)) will be set with same way. However, as the totally strain is 6% which the status is fixed in the tensile test machine, the totally strain contains elastic strain and plastic strain in it. Because the photos are taken by OM that the specimen has been pulled down from the tensile test machine, there will be only plastic strain displayed in the specimen. In this research, the specimen has been tested for two times with each time 3% totally strain. It reveals that, the elastic strain has been added for two times. Hence, the plastic strain for the whole specimen will be a little less than 6%.

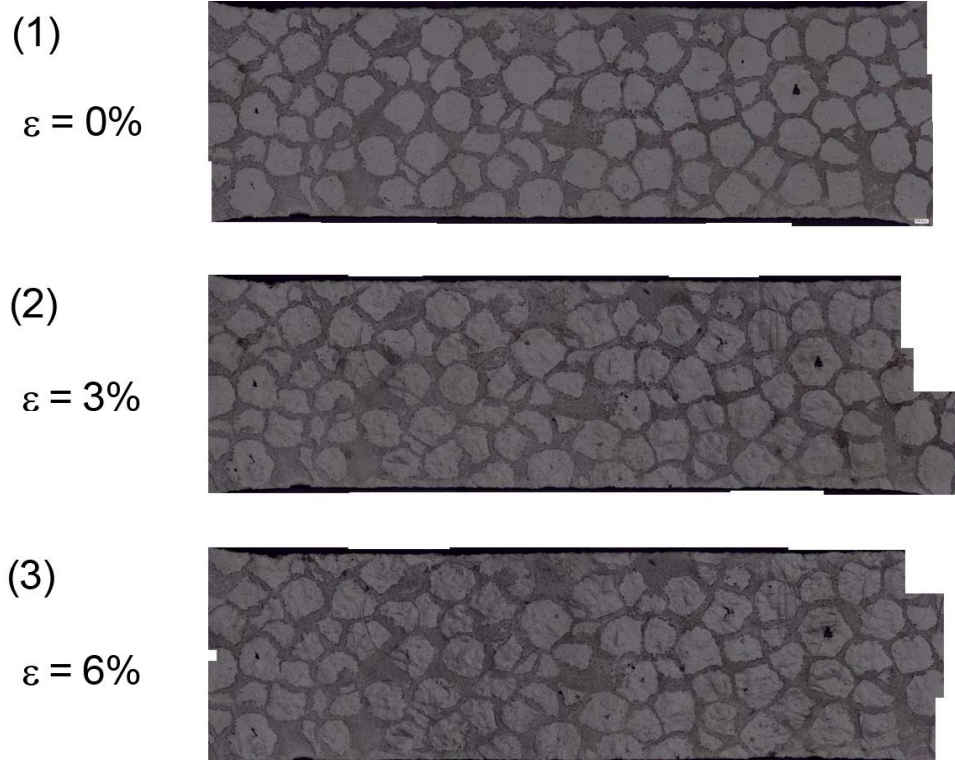


Figure 7.1: Pieced together tensile test photos of SUS304L 360h MM specimen by OM (optical microscope). (1) $\varepsilon = 0\%$; (2) $\varepsilon = 3\%$; (3) $\varepsilon = 6\%$.

However, if lapse happens in some grids, the previous calculation will be repealed at all. Moreover, after each tensile test, the specimen will be unloaded from the tensile test machine and cleaned again by ultrasonic cleaner. Sometimes, a small quantity of little cuts happens inevitably. The cuts happened after deformation will bring difficulty for the soft to notice the same region before and after deformation. Hence, the calculation should be separated to several regions.

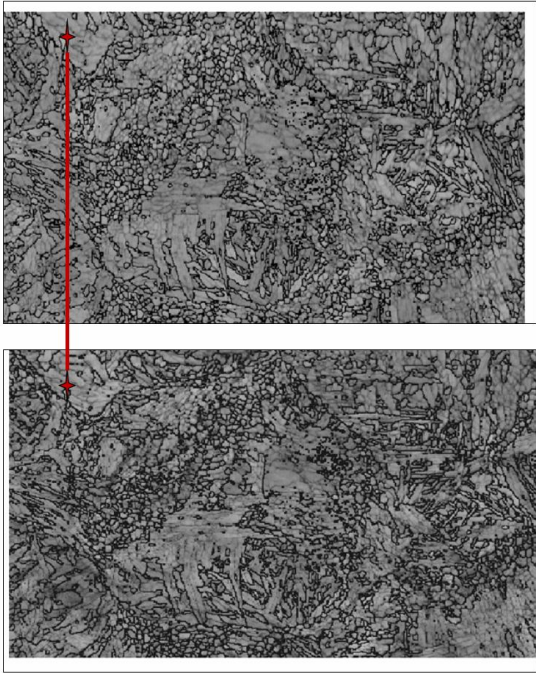


Figure 7.2: Make sure the initial point of calculation fixing the same positions.

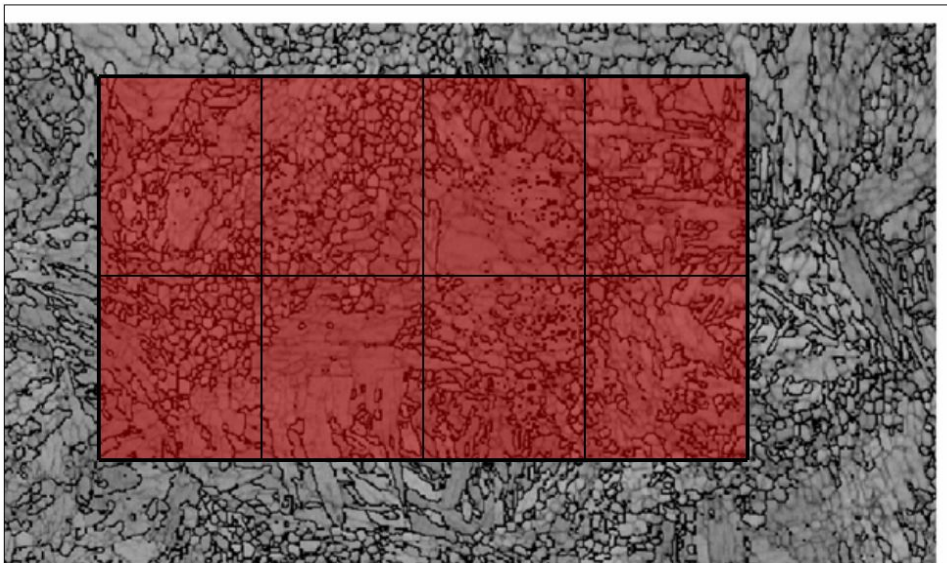


Figure 7.3: Divide the whole calculation region into small regions, due to decreasing the possibilities of mistakes.

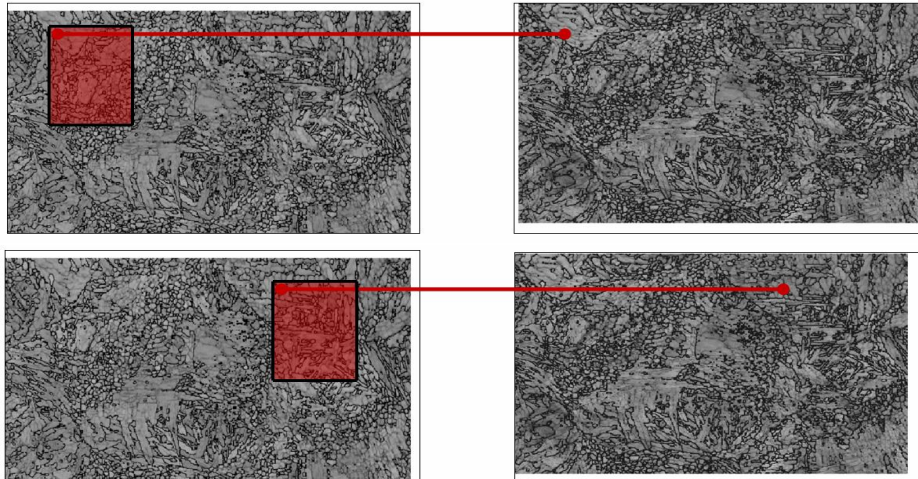


Figure 7.4: Adjust the position of the photo after deformation to make sure the the initial point of calculation fixing the same positions.

For this research, the 7 rows as 7 regions of photos for a whole harmonic structure tensile test specimen have been applied. For each region, in order to guarantee the position of upper left grid before and after deformation, the photo of after deformation should be moved to fix it. I used the ruler tool in the Photoshop to fix position. I used direction keys in keyboard to move the photo of after deformation. By this way, each step represents one pixel. The amount of movement should be recorded, and the data can be restored to the original state in the whole final calculation. The amount of movement should be added in the after deformation data.

7.3 Programming for post treatment

After simulated by the DIC soft, the coordinates' data of center of the grids before and after deformation have been written as excel file. I created a VB program in this research to make the results visualization. This post treatment soft has contained two functions: first, displaying the displacement; second, the strain distribution.

For the displaying of the displacement, the target is to draw the arrow shape. It is easy to draw a line to connect the center of grid before and after deformation with command of "line (x1,y1)-(x2,y2)". The arrowhead can be drawn by using the line

command to draw two little lines. For the DIC soft result, there is a parameter called similar degree to describe the similarity before and after deformation. Hence, while drawing the displacement result, the Schwellenwert should be set in the post treatment soft that the data below it will not be shown in the result. The Schwellenwert can be set as 0.7. However, the data of similarity are just for reference. We can confirm that the DIC soft will stop calculating after five or more low similar degree data happening.

For the strain distribution, the region between two center points of grids will be the effective region for the strain. Because the photo is taken landscape orientation as the direction of tensile test. The ratio of landscape distances of the neighbor center points of grids before and after deformation will be the strain. In order to reach transparent display. Command of “AlphaBlend” has been employed. The function “AlphaBlend” is written as `AlphaBlend (HDC hdcDest, int nXOriginDest, int nYOriginDest, int nWidthDest, int hHeightDest, HDC hdcSrc, int nXOriginSrc, int nYOriginSrc, int nWidthSrc, int nHeightSrc, BLENDFUNCTION blendFunction)`. We can use “AlphaBlend” to make some existed figures translucent. It is used to make the label and show the strain distribution and the original OM photo simultaneously. Hence, as shown in Figure 7.5, I prepared some pure color figures for label owing to the convenience. These pure color figures can be built by command before the “AlphaBlend” command also.

For the displaying of strain distribution, the foremost rows may have some problems while the grid in first row sometimes shows inaccuracy. It will influence the whole data. Hence, parameter should be added which describe from which row the results can be shown. Figure 7.7 shows the example for pure Ti. In order to analysis the strain distribution happened in the harmonic structure specimen, the transparency level should be adjusted.

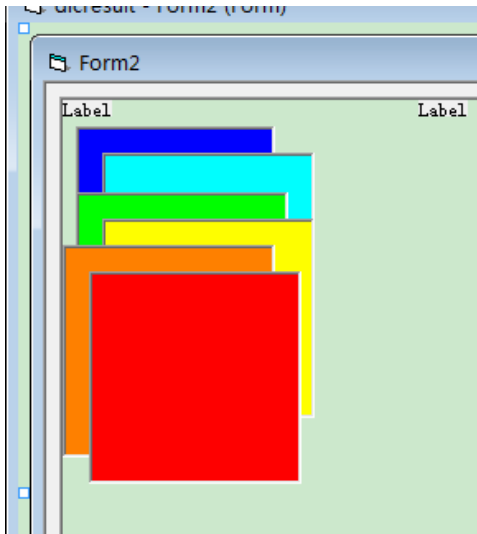


Figure 7.5: Due to command “AlphaBlend”, prepare color figures for label.

As shown in Figure 7.4, because the positions of the photos after deformation have been adjusted to make sure the initial points of calculation fixing the same positions, before integrating the csv files, we should modify the coordinates of after deformation photos in the csv files. We can modify the csv files in excel itself. After modifying the coordinates data in the csv files, the whole files should be integrated into one file. I applied VB to make a program to integrate the files. The program concludes three parameters which users should set: each line with how many files; how many lines; how many cycles the calculation has run.

Because the original csv file pretermits the parameter for the number of calculation of the before deformation data as 0, the parameter has been added one per cycle. It can be used to record the cycle.

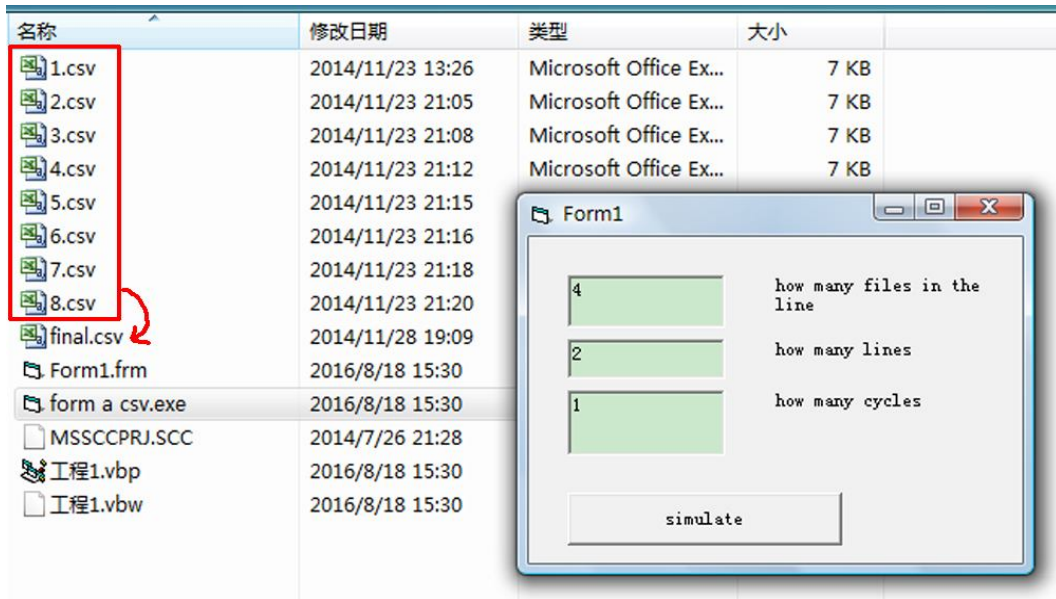


Figure 7.6: Integrate small regions files into the final file.

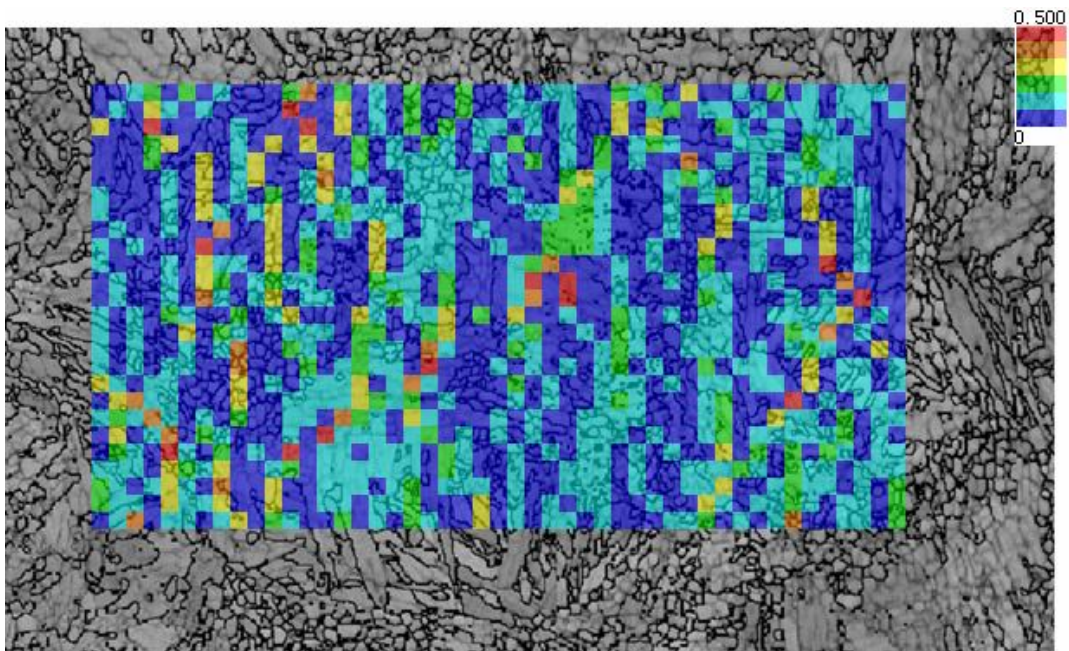


Figure 7.7: Strain distribution for the whole part.

7.4 Results

Figure 7.8 shows the displacement distribution of the uniaxial tensile test result of

SUS304L 100h MM specimen in $\varepsilon = 6\%$. The yellow arrows represent the displacement. Because the totally strain is just 6% which is too small to see, the distribution result is two times of real result. Owing to the calculation principle of DIC soft, the top left corners before and after deformation should be matched together. Hence, the lengths of the arrows become from short to long with the horizontal axis. If we don't want the arrows to show disequilibrium that the left side shows too short while right side shows too long, we can change the data in the csv file by adding a constant value in the whole data after deformation.

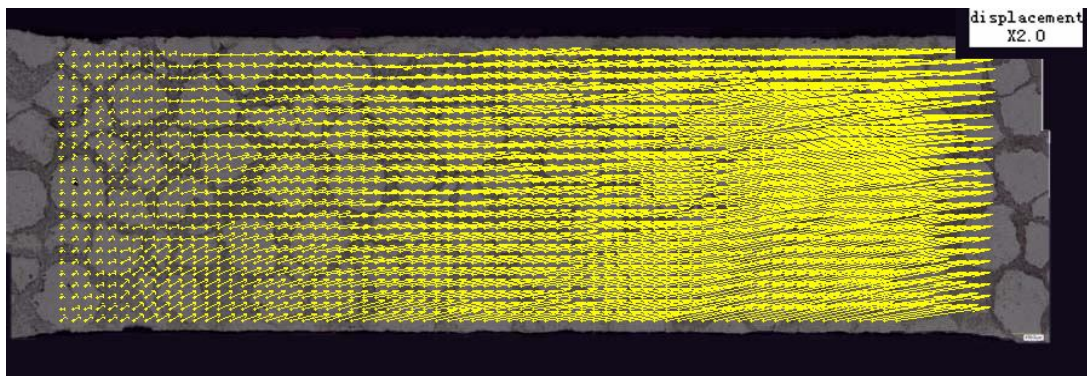


Figure 7.8: Displacement of the tensile test SUS304L 360h MM specimen. $\varepsilon = 6\%$.

Figure 7.9 represents the strain distribution of the uniaxial tensile test result of SUS304L 100h MM specimen in $\varepsilon = 6\%$. I applied 18 pieces of photos to constitute the whole stretching regions of the I-shape specimen. From the result shown in Figure 7.9, it can be clearly observed that although the strain value ranges from 0 to 30%, the whole distribution is relatively uniform. For the general homogeneous specimen tensile test result, the strain distribution will show radioactive from a center line. However, for harmonic structure, instead of a center line, the tendency of strain distribution is dispersal. It can be clearly observed that many relatively strain concentrations happened in the CG regions, while the UFG regions show lower strain. Meanwhile, many relatively high strain regions appear in the center parts of the CG regions. The DIC result is in keeping with the multi-scale FEM result discussed in Chapter 4. The high elongation but low strength CG regions suffer more strain to ease the burden of the high strength but low elongation UFG regions.

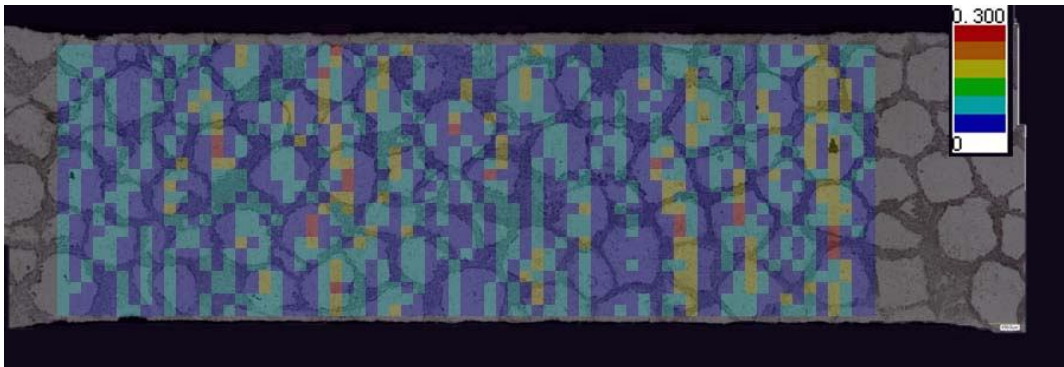


Figure 7.9: Strain distribution of the uniaxial tensile test SUS304L 360h MM specimen.

$$\varepsilon = 6\%.$$

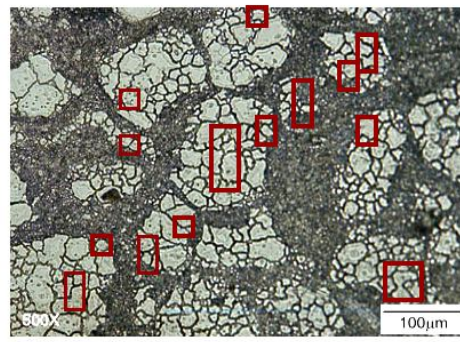
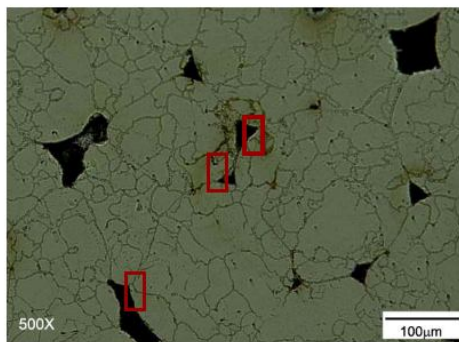
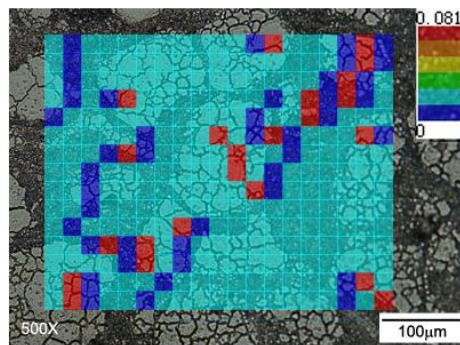
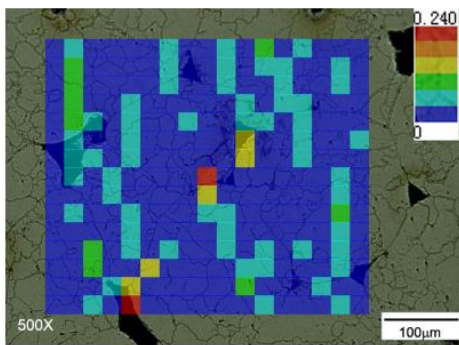
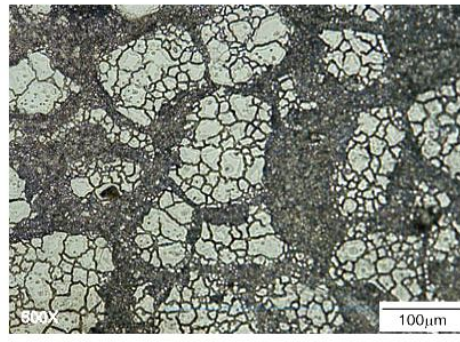
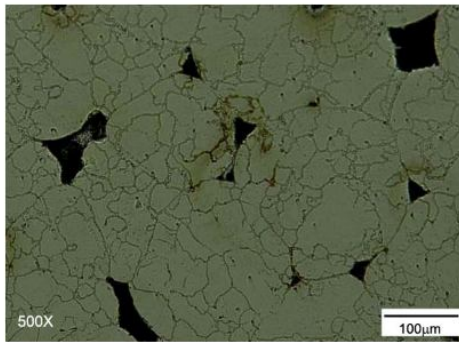
Figure 7.10 demonstrates the strain distribution comparison between SUS304L initial powder (IP) and harmonic structure specimens of uni-axial tensile test with total strain of 5%. These two specimens are just be stretched for one time which is different from the two times test discussed above. These two specimens use just one piece of photo, hence, the calculation region is smaller than the test discussed above.

The figures on the left side are photos for IP, while the figures on the right side show photos for harmonic structure. For the IP specimen, there are some holes in the sintered compact. After tensile test, the strain locations happened near the holes. For the IP specimen, the max strain value is as high as 0.24, and the max value appears in just two places in the calculation region. As a general homogeneous object, the strain distribution is radioactive from a center point. In contrast with IP, for the harmonic structure, the max strain value is just 0.081. Although the calculation region for harmonic structure is as small as the IP, it can still be observed that the max strain value of 0.081 appears in many districts for the harmonic structure. Meanwhile, the most relatively high strain regions are in the centers of the CG regions. With the network structure of the UFG region, the original CG regions are separated into many small regions. The extension of the strain locations appeared in general IP specimen has been interdicted by the network structure of UFG phase. While the strain distribution happened in one CG core has been restricted by the ambient UFG phase, because of the fixed total deformation of the specimen, relatively high strain will

appear in other CG cores. The majority strain has been shared by many CG cores which will lead to the relatively lower strain in each CG core compared to the strain localization happened in general homogeneous specimen. Hence, the strain localization which has happened in IP will not appear in harmonic structure. The harmonic structure specimen demonstrates the relatively uniform deformation as the periodic boundary condition multi-scale FEM results shown. The multi-scale FEA model for harmonic structure can be validated.

Figure 7.11 shows the morphology of Ni initial powder and harmonic structure tensile elongated specimens. From the data of reduction of area, it can be clearly revealed that for the harmonic structure specimen (square shape), the cross-sectional area shrinkage curve is a patelliform. This result indicates that the harmonic structure demonstrates uniform deformation without any remarkable necking formation. In contrast, for the initial powder specimen, there is no “plate-like” region in the cross-sectional area shrinkage curve, and strain localization is observed near the end point. It can be predicted the strain localization happens in the pore regions. These results demonstrate that the harmonic structure design promotes uniformity of deformation compared with structure of IP, thus leading to suppressed strain localization and relatively higher tensile ductility. Thereby, these experimental results have a good agreement with the FEM results.

$\epsilon = 5\%$



SUS304L IP

SUS304L harmonic structure

Figure 7.10: Strain distribution comparison between SUS304L IP and HS specimens.

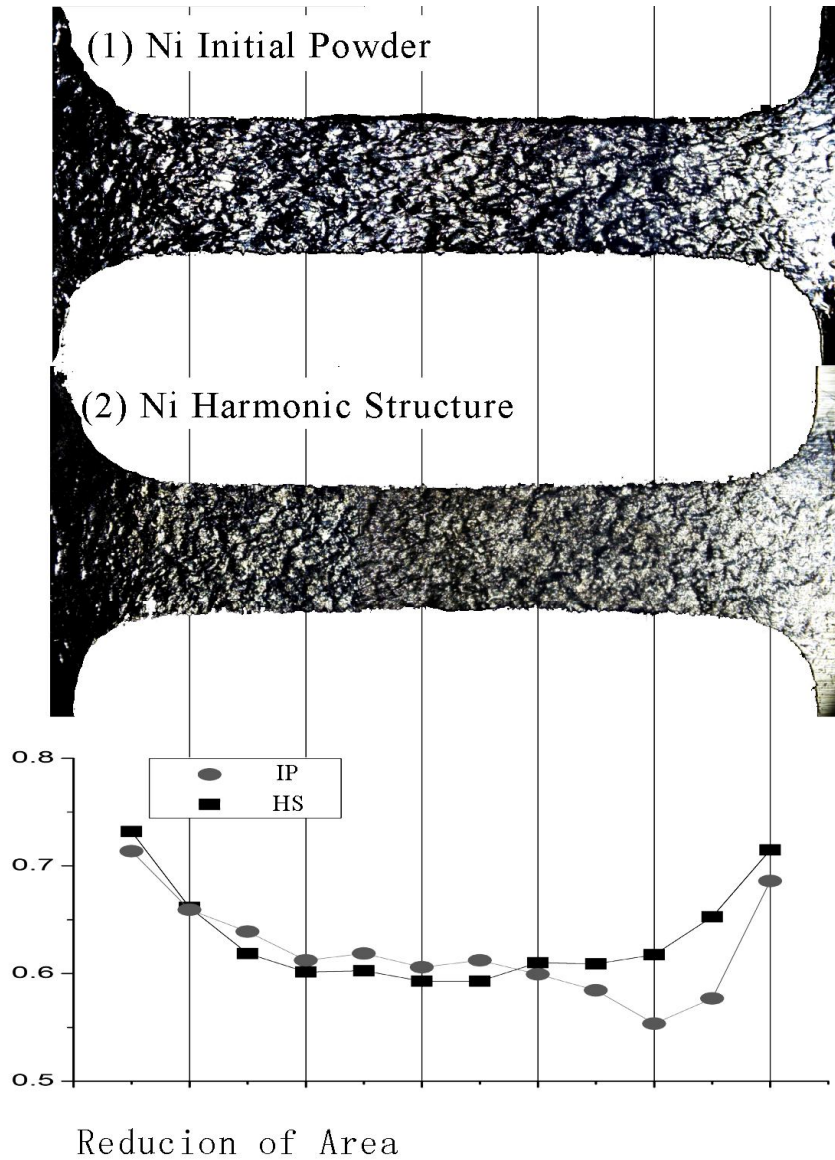


Figure 7.11: Morphology of tensile elongated specimens: (1) Ni Initial Powder and (2) Ni Harmonic Structure.

References

- [1] Peters, W. H., and Ranson, W. F., 1982. Digital Imaging Techniques in Experimental Stress-Analysis. *Opt. Eng.* 21(3), 427 - 431.
- [2] Chu, T., Ranson, W., and Sutton, M., 1985. Applications of Digital-Image-Correlation Techniques to Experimental Mechanics. *Exp. Mech.*

- 25(3), 232 - 244.
- [3] Sutton, M. A., Cheng, M. Q., Peters, W. H., Chao, Y. J., and McNeill, S. R., 1986. Application of an Optimized Digital Correlation Method to Planar Deformation Analysis. *Image. Vision. Comput.* 4(3), 143 - 150.
- [4] Lagattu, F., Bridier, F., Villechaise, P., and Brillaud, J., 2006. In-Plane Strain Measurements on a Microscopic Scale by Coupling Digital Image Correlation and an In Situ SEM Technique. *Mater. Charact.* 56(1), 10 - 18.
- [5] Sutton, M. A., Li, N., Garcia, D., Cornille, N., Orteu, J. J., McNeill, S. R., Schreier, H. W., and Li, X., 2006. Metrology in a Scanning Electron Microscope: Theoretical Developments and Experimental Validation. *Meas. Sci. Technol.* 17(10), 2613 - 2622.
- [6] Jin, H., Lu, W., and Korellis, J., 2008. Micro-Scale Deformation Measurement Using the Digital Image Correlation Technique and Scanning Electron Microscope Imaging. *J. Strain Anal. Eng. Des.* 43(8), 719 - 728.
- [7] Pan, B., Qian, K., Xie, H., and Asundi, A., 2009. Two-Dimensional Digital Image Correlation for In-Plane Displacement and Strain Measurement: A Review. *Meas. Sci. Technol.* 20(6), 062001.
- [8] Krehbiel, J. D., Lambros, J., Viator, J., and Sottos, N., 2010. Digital Image Correlation for Improved Detection of Basal Cell Carcinoma. *Exp. Mech.* 50(6), 813 - 824.
- [9] Tong, W., 2013. Formulation of Lucas - Kanade Digital Image Correlation Algorithms for Non - contact Deformation Measurements: A Review. *Strain.* 49(4), 313 - 334.
- [10] Kammers, A. D., Daly, S., 2013. Digital Image Correlation Under Scanning Electron Microscopy: Methodology and Validation. *Exp. Mech.* 53(9), 1743 - 1761.
- [11] Kammers, A. D., Daly, S., 2013. Self-Assembled Nanoparticle Surface Patterning for Improved Digital Image Correlation in a Scanning Electron Microscope. *Exp. Mech.* 53(8), 1333 - 1341.
- [12] Karlsson, J., Sjogren, T., Snis, A., Engqvist, H., & Lausmaa, J. (2014). Digital

- image correlation analysis of local strain fields on Ti6Al4V manufactured by electron beam melting. *Mater. Sci. Eng.: A.* 618, 456-461.
- [13] Wang, X. J., Pan, Z. P., Fan, F. F., Wang, J. W., Liu, Y., Mao, S. X., Zhu, T., Xia, S. M., 2015. Nanoscale deformation analysis with high-resolution transmission electron microscopy and digital image correlation. *J. Appl. Mech.* 82(12), 121001.
- [14] Yang, G., Cai, Z., Zhang, X., Fu, D., 2015. An experimental investigation on the damage of granite under uniaxial tension by using a digital image correlation method. *Opt. Laser. Eng.* 73, 46 - 52.
- [15] Salvini, P., Lux, V., Marotta, E., 2015. Modal Pursuit to Detect Large Displacements and Strain Fields by Digital Image Correlation. *Strain.* 51(1), 30 - 42.
- [16] Milosevic, M., Milosevic, N., Sedmak, S., Tatic, U., Mitrovic, N., Hloch, S., Jovicic, R., 2016. Digital Image Correlation in analysis of stiffness in local zones of welded joints. *Teh Vjesn.* 23(1), 19 - 24.

Chapter 8: The feasibility of harmonic structure multi-scale model with multi-layer shell region

8.1 The solid foundation of harmonic structure material with multi-layer shell region

As the definition harmonic structure, the harmonic structure is a unique heterogeneous bi-modal structure consisting of coarse-grained areas (cores) enclosed in a three-dimensional continuously connected network of UFG structures (shell). While in some situations, there will be an intermediate layer between shell regions and core regions, which has the midterm grain size and midterm characteristics between UFG area and CG area. Ota et al. (2014) shows a harmonic structure with multi layer shell region. It has been observed a grain size gradient of the shell region in harmonic S329J1 which has been recognized as mid-shell and outer-shell [1]. However, this outer-shell is not with the intermediate grain size between UFG and CG phases but is consisted of both UFG and CG mix phases. Nevertheless, the characteristic of this region can be recognized between homogeneous UFG and CG materials.

In this chapter, the realizability of multi-scale FEA with multi layer shell region has been investigated.

8.2 Body fitted anisotropic layers in ICEM

Body fitted anisotropic meshes have been employed in this research as the intermediate layer meshes instead of dividing new blocks for intermediate layer. Body fitted anisotropic meshes have always been applied in computational fluid dynamics (CFD) problems [2-15]. In fluid problems, hydraulic resistance happened in the region near the wall is a major factor affecting of the calculation accuracy. Hence, there is demand to refine the meshes near the wall. The number of body fitted

anisotropic layers is often more than four generally. However, considering the mesh size balance, there is no need to divide so many layers.

In ICEM software, there are two methods to divide body fitted anisotropic meshes: controlling the number and arrangement of nodes in the blocks' edges for hexahedron mesh; using prism meshing parameters. For the first method, there is no way to distinguish the meshes' serial number for every layer. It means that the shell region can not be divided into multi layers. In contrast, with the second method, the new prism meshes will show large serial numbers relative to origin meshes although the new meshes share same material properties and same unit sets with origin meshes. Because the truncated octahedron based model has complicated shape, there are many blocks in the origin models. Hence, the new prism meshes will distribute on the basis of blocks, dispersedly. However, the large serial numbers are conspicuous. The large serial numbers meshes can be picked as a new group. Then we should set the new group with a new material. Importing the inp file into ABAQUS, the different colors based on materials will indicate if the shell region is divided into layers. Because picking the large serial numbers meshes is feasible but trivial and taking time, in this research, only 1/8 unit has been employed. After clearance for the 1/8 unit, the mirror step which has been shown in chapter 4 can be applied to build the whole unit.

In order to divide the body fitted anisotropic meshes, we can apply the function called prism mesh. Because the body fitted anisotropic meshes are divided from original meshes, before generating prism meshes, there should be the basement meshes already. For pure CFD simulation, the boundary of fluid is usually wall. Hence, the fluid can be one block group overall. However, for dividing the intermediate layer, there are two types of materials already, hence there are two block groups. Before applying the prism mesh, the interior surfaces shared by two block groups should be chosen as individual parts which are prepared for prism meshes setting.

Figure 8.1 shows an example of setting the prism mesh parameters. To generate one layer intermediate mesh, the block which will conclude the body fitted anisotropic meshes should be chosen first. Then the prepared surfaces should be

selected with the height 1, height ratio 1, num layers 2. Comparing the mesh in the left and the right, it can be clearly observed that in the blue meshes, a new layer of meshes appear.

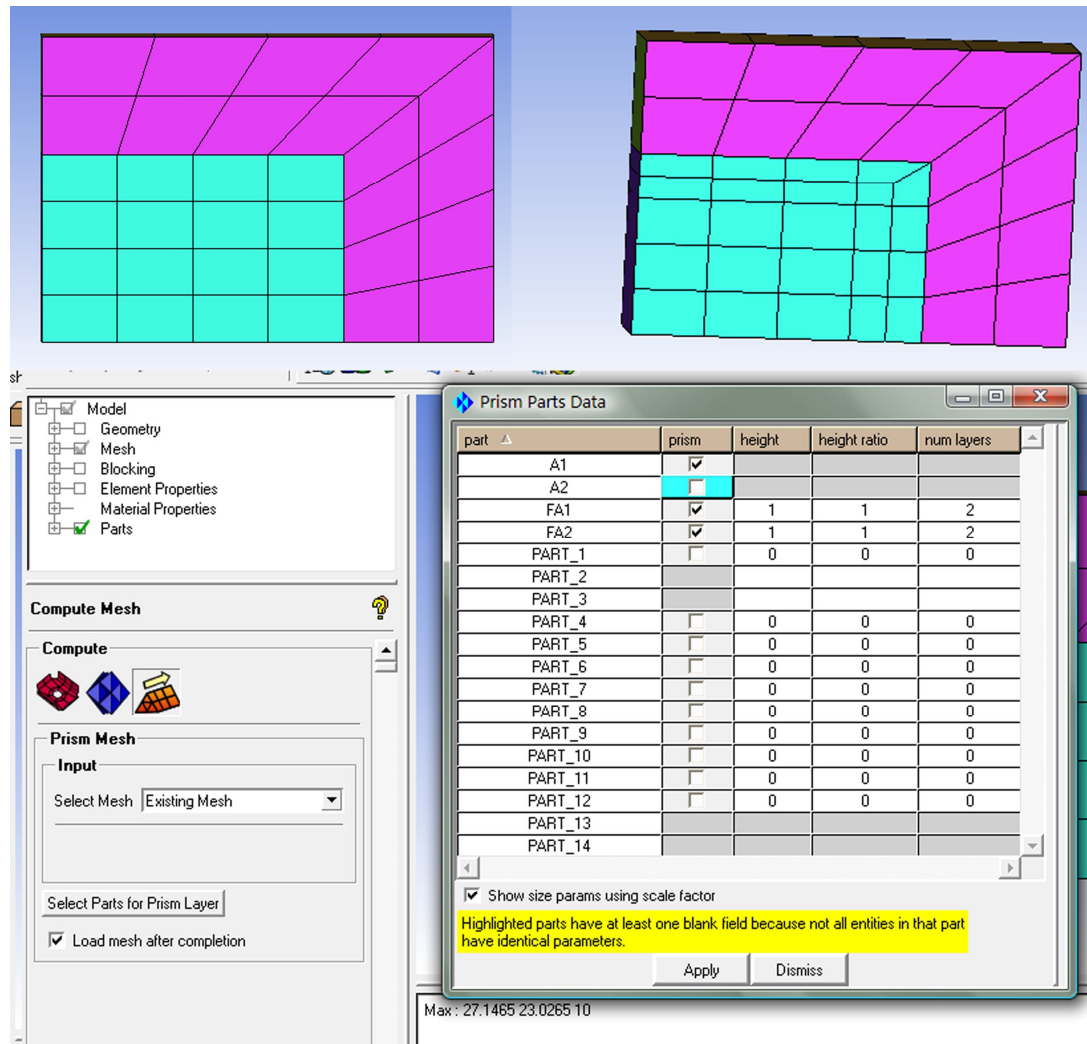


Figure 8.1: Body fitted anisotropic layer meshes generation in ICEM.

As shown in Figure 8.2, in the inp file, the large serial numbers mesh elements with the number above 200 can be clearly distinguished from the normal serial numbers mesh elements with the double figures numbers. The large serial numbers mesh elements are the new generation body fitted anisotropic layer meshes. We can modify the inp file by creating a new command “*ELEMENT”, which makes a new group for the elements. Then we should cut and paste the large serial numbers mesh

elements messages into the new element group. Endue the new element group with a new material characteristic. Afterwards, in ABAQUS, the result can be shown as the Figure 8.2. The red mesh elements are the intermediate layer meshes modified from new generation body fitted anisotropic layer meshes. Hence, the intermediate layer meshes can be generated by this way.

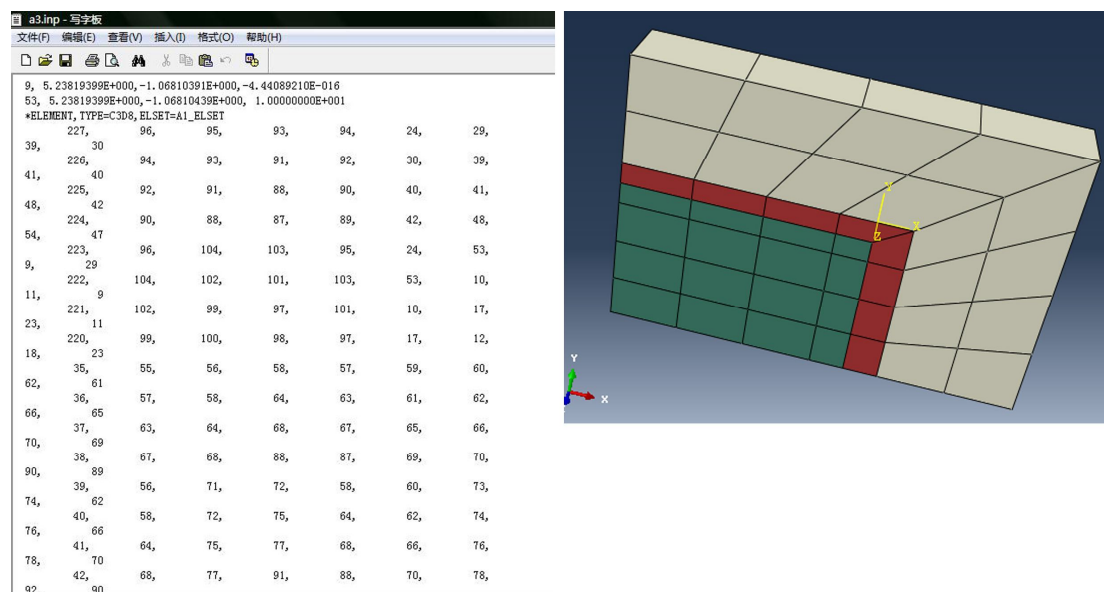


Figure 8.2: Distinguish the new generation body fitted anisotropic layer meshes by serial numbers of nodes.

As shown in Figure 8.3, when the body fitted anisotropic layer function is used twice, the mesh elements with large serial numbers have a discipline. The numbers of the two times body fitted anisotropic layer meshes are not continuous. It can be observed that the number from 245 directly to 255. It is an obvious watershed to distinguish the two times body fitted anisotropic layer meshes. By setting the two times body fitted anisotropic layer meshes with different materials. In ABAQUS, it can be shown with materials' color (Figure 8.3), one layer is red, while one layer is blue. However, Figure 8.3 shows a very simple model. While the origin model without body fitted anisotropic layer meshes is complicated, the original mesh numbers are not continuous. Meanwhile, the amount of the meshes is very large. It is difficult to distinguish two times body fitted anisotropic layer meshes. Even just for

one time body fitted anisotropic layer meshes in 1/8 harmonic structure model, because the original model is complicated, the new generated body fitted anisotropic layer meshes are distributed by many parts into the original meshes in the inp file. Fortunately, the new generated body fitted anisotropic layer meshes are still with the large serial numbers compared to the original meshes. By picking all the large serial numbers meshes into a new element group. The rudiment step of generating harmonic structure material model with multi layer shell regions can be achieved. In order to make sure all the new generated body fitted anisotropic layer meshes are concluded to the new group, it can be observed by ABAQUS using different colors to describe the different materials.

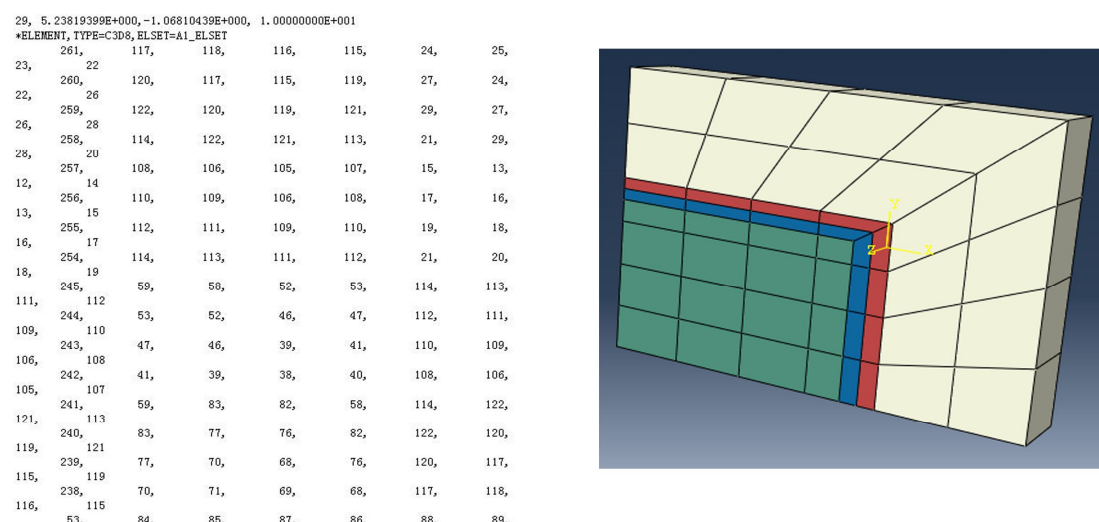


Figure 8.3: Generate body fitted anisotropic layer twice.

8.3 Dealing with the wrong sequence node serial number meshes

However, as the model is complicated itself, there are some errors happening in the 1/8 unit without predicting. As shown in Figure 8.4, in ABAQUS, some meshes seem to be missed which should be displayed. However, the similar error happened in making mirror program in Chapter 4 which aims to use mirror to build random structure model. The reason is the wrong order of the node serial number. The disappeared meshes are with minus volume. In ABAQUS, just inverse hour direction

can be acknowledged. While one mesh has 8 nodes, the number 2 should be exchanged with number 4, the number 6 should be exchanged with number 8. For simple shape blocks, the new prism meshes can be generated smoothly and with no error. But the model for harmonic structure is truncated octahedron which has complicated shape, it will make the block dividing difficult and finally bring up a complicated combination of blocks. As the new prism meshes generated automatically, the reaction in complexity is opposite direction of some meshes. The opposite direction meshes should be found one by one, and the nodes' order should be modified. After modifying the nodes' order with wrong directions, the 1/8 unit can be mirrored by x-, y-, z-axis, respectively. Then, the model for the harmonic structure multi-scale model with multi-layer shell regions can be built as Figure 8.5 shown. The color of mesh shown in Figure 8.5 is displayed by material, respectively. The green, red, white parts represent three types of materials. The interface layer has one layer of meshes which are red in this research.

By applying two times body fitted anisotropic layer function, the interface layer can have two layers of meshes. However, there will be more disappeared meshes with minus volume. Even in the 1/8 model, there are two parts of the intermediate mesh. For the one time body fitted anisotropic layer function in Figure 8.4, there are 135 meshes for one side intermediate mesh in 1/8 model. Hence, there are 270 meshes for the new generating intermediate mesh in 1/8 model even it is just one layer of mesh.

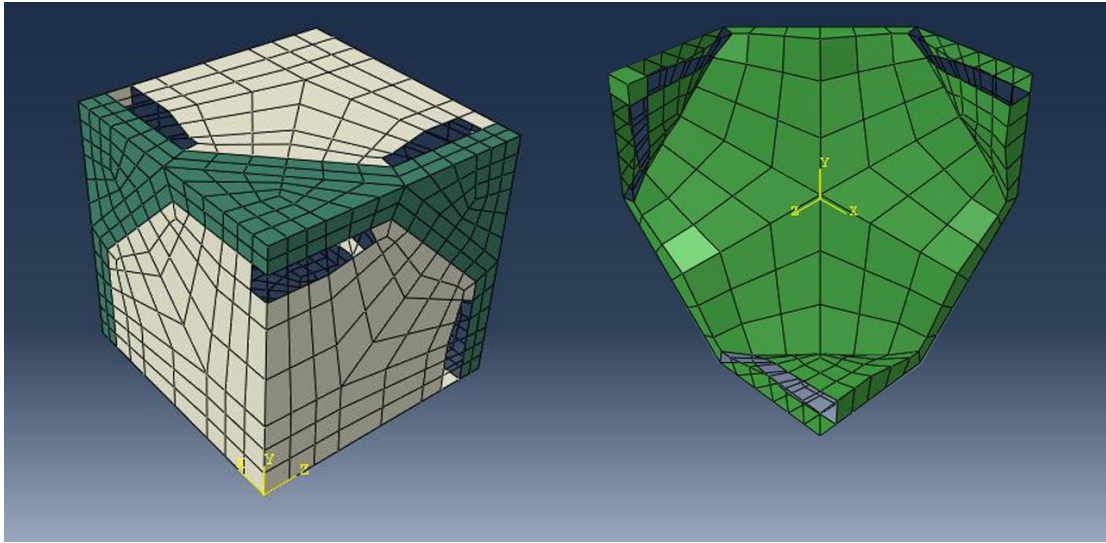


Figure 8.4: Some body fitted anisotropic layer meshes disappeared in ABAQUS.

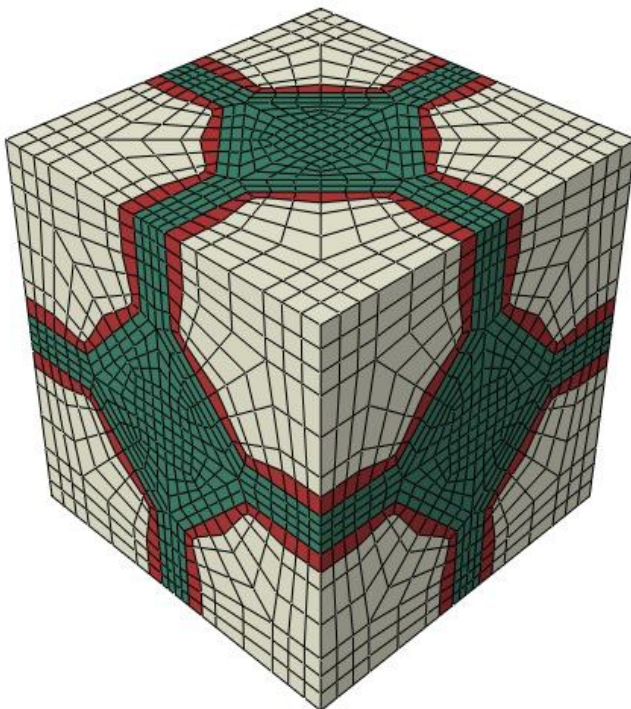


Figure 8.5: Harmonic structure multi-scale model with multi layer shell region.

8.4 Simulation results

Figure 8.6 demonstrates the Von Mises Stress and max. principal plastic strain distribution of the harmonic structure with mono-layer shell and with multi-layer shell. For the Von Mises Stress, it can be observed that except of the original low stress CG region and high stress UFG region, there is one intermediate value stress region between CG region and UFG region. For the max. principal plastic strain distribution, there is no obvious boundary between UFG region and intermediate layer. It demonstrates that the intermediate layer and UFG region both show low strain, while the CG region shows relatively higher strain.

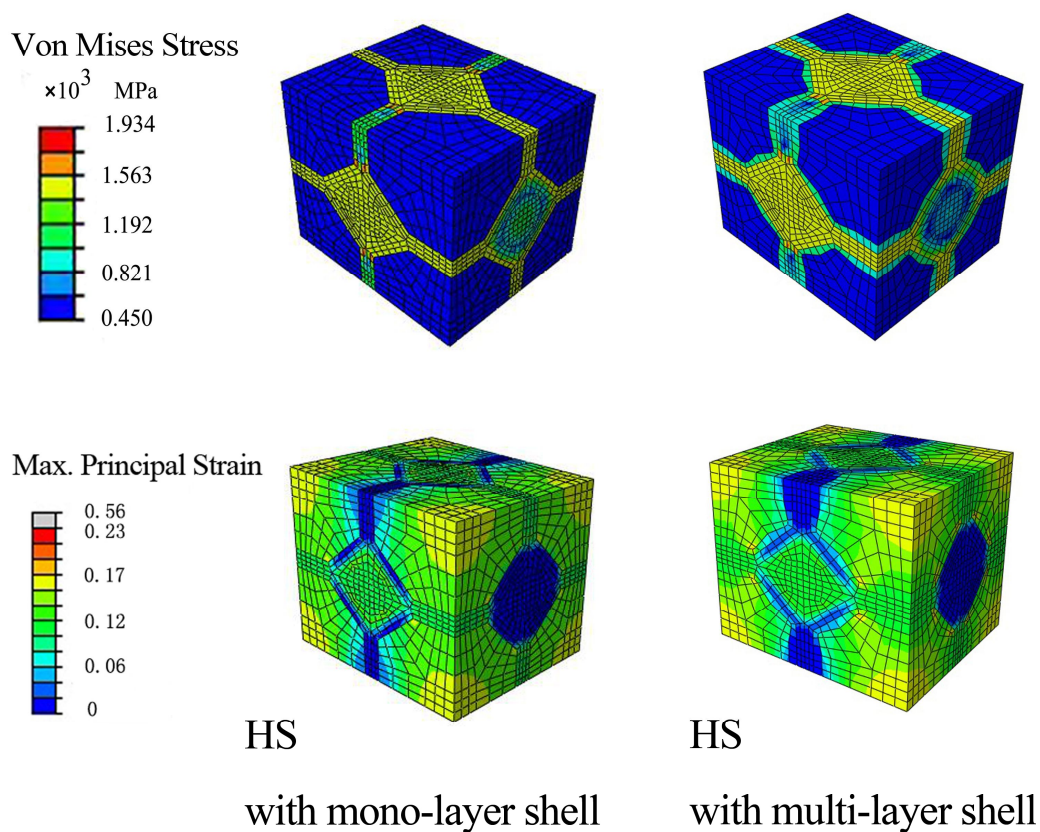


Figure 8.6: Von Mises Stress and max. principal strain distribution for harmonic structure with mono-layer shell and multi-layer shell.

8.5 Conclusions

In this chapter, the feasibility of building harmonic structure multi-scale model with multi-layer shell region has been discussed. Thanks to Body fitted anisotropic layers function in ICEM, which is widely used in computational fluid dynamics problems, the intermediate region can be obtained. However, the complexity of the original harmonic structure material model led to a problem in which some minus volume meshes appear. By amending the order of minus volume meshes' nodes, the problem can be solved. Hence, the model for the harmonic structure with intermediate shell region was completed. For the comparison of the harmonic structure models with mono-layer shell and multi-layer shell, it can be clearly observed that, the value for Von Mises Stress of the outer shell regions is between the values of core and inter shell regions. At the same time, intermediate layer and UFG region both show low strain, while the CG region shows relatively higher strain.

References

- [1] Ota, M., Sawai, K., Kawakubo, M., Vajpai, S. K., Ameyama, K., 2014. Harmonic structure formation and deformation behavior in a $(\alpha + \gamma)$ two phase stainless steel. *Mater. Sci. Eng.* 63, 012027.
- [2] Schlichting, H., 1960. *Boundary layer theory*. McGraw-Hill Book Company Inc, New York
- [3] Barbosa, H. J. C., Thomas, J. R. H., 1991. The finite element method with Lagrange multipliers on the boundary: circumventing the Babuska-Brezzi condition. *Comput. Meth. Appl. Mech. Eng.* 85(1), 109 - 128
- [4] Beran, P., 1991. Steady and unsteady solutions of the Navier-Stokes equations for flows about airfoils at low speeds. *AIAA Paper*. 91 - 1733
- [5] Baker, T. J., 1997. Mesh adaptation strategies for problems in fluid dynamics. *Finite Elem Anal Des.* 25(3), 243 - 273.

- [6] Borouchaki, H., Georges, P. L., Hecht, F., Laug, P., Saltel, P., 1997. Delaunay mesh generation governed by metric specifications. part I. algorithms. *Finite. Elem. Anal. Des.* 25(61 - 83), 85 - 109
- [7] Borouchaki, H., Hecht, F., Frey, P. J., 1998. Mesh gradation control. *Int. J. Numer. Meth. Eng.* 43(6), 1143 - 1165.
- [8] Jansen, K. E., Shephard, M. S., Beall, M. W., 2001. On anisotropic mesh generation and quality control in complex flow problems. In *Tenth International Meshing Roundtable*. pp. 111 - 134.
- [9] Li, X., Remacle, J. F., Chevaugeron, N., Shephard, M. S., 2004. Anisotropic Mesh Gradation Control. In *IMR*. pp. 401 - 412.
- [10] Frey, P., Alauzet, F., 2005. Anisotropic mesh adaptation for CFD computations. *Comput. Meth. Appl. Mech. Eng.* 194(48 - 49), 5068 - 5082.
- [11] Choi, J. I., Oberoi, R. C., Eewards, J. R., Rosati, J. A., 2007. An immersed boundary method for complex incompressible flows. *J. Comput. Phys.* 224, 757 - 784.
- [12] Claisse, A., Ducrot, V., Frey, P., 2009. Levelsets and anisotropic mesh adaptation. *Discret. Contin. Dyn. Syst.* 23(1 - 2), 165 - 183.
- [13] Dolbow, J. E., Harari, I., 2009. An efficient finite element method for embedded interface problems. *Int. J. Numer. Meth. Eng.* 78(2), 229 - 252.
- [14] Alauzet, F., 2010. Size gradation control of anisotropic meshes. *Finite. Elem. Anal. Des.* 46(1 - 2), 181 - 202.
- [15] Quan, D. L., Toulorge, T., Bricteux, G., Remacle, J. F., Marchandise, E., 2014. Anisotropic adaptive nearly body-fitted meshes for CFD. *Eng. Comput.* 30(4), 517 - 533.

Acknowledgement

First of all, I would like to express my most sincere gratitude to Prof. Kei AMEYAMA, who gave me such a wonderful opportunity to be part of Ameyama lab members. All the invaluable advice and generous encouragements from him through the joyous times during four years in Ritsumeikan University are mostly appreciated. His wide sight and professional knowledge in this field has helped me a lot in improving and building basic and fundamentals in materials science field. Moreover, I would express deeply appreciation of his assistance in Japanese language and culture, which makes me to be involved in the life of study in Japan. I would like to express my appreciation deeply on the guidance and encouragement from him, which enabled me to benefit a great deal both in academic matters and personal growth.

I also wish to express my deepest appreciation to Dr. Ikumu WATANABE, a senior researcher in NIMS for his considerable guidance on my scientific work of FEM simulation. Under his kind guidance, I come to understand the FEM mechanism foundation deeper and better, which becomes the indispensable basis of this thesis. Besides, I must thank to his constant supports and fruitful suggestions in the paper writing.

I own my most sincere gratitude to Dr. Mie OTA, an assistant professor in AMEYAMA laboratory, for her useful advice, assistant both on my research and usual life in Japan. She gave me a lot of selfless support in undertaking experiments and research. Besides, thanks to much warm company from her, my study and life in Japan has become more enjoyable.

My heartfelt thanks to all of the past and present members in AMEYAMA laboratory, their very kind assistance and company has helped me significantly during my study and life in Ritsumeikan University. Special thanks to Dr. Zhe ZHANG, Dr. Yanbo SUN, Dr. Nur Zalikha Binti Khalil, Mrs. Nurul Nadiah binti Mahmud and Mr. Bo TONG for their wonderful assistance.

I am also heartily thankful to all of my friends. I should express many thanks to all the people who have given me kind assistance during my study and life.

Finally, I should finally like to express my best gratitude to my beloved parents who have been assisting, supporting and caring for me all of my life no matter in economy or spirit. I am indebted to them.

Han YU

Kusatsu, Japan

2016